

AD-A156 394

ANALYSIS OF TWO-PARAMETER CONSTANT BACKGROUND BORN
INVERSION FOR ACOUSTIC. (U) COLORADO SCHOOL OF MINES
GOLDEN CENTER FOR WAVE PHENOMENA P B VIOLETTE

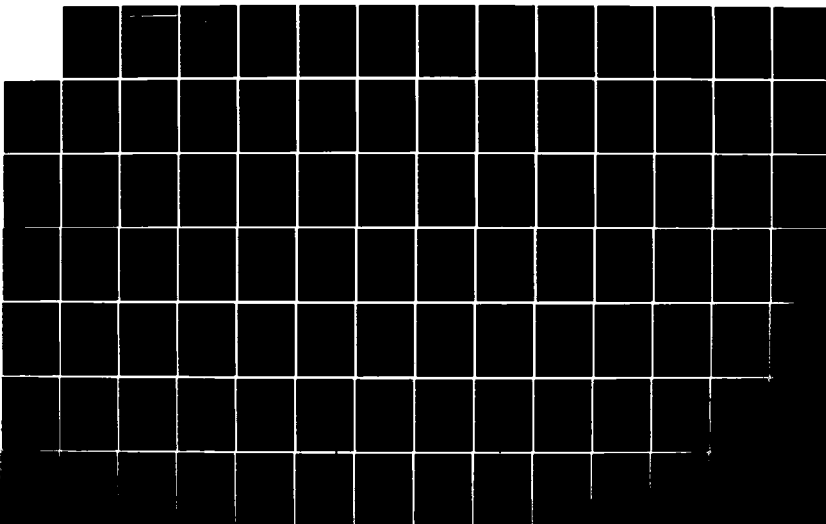
1/2

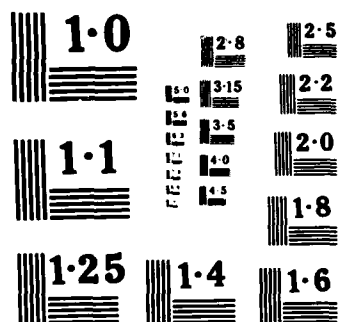
UNCLASSIFIED

15 MAY 85 CMP-029 N00014-84-K-0049

F/G 17/10

NL





NATIONAL BUREAU OF STANDARDS
MICROCOPY RESOLUTION TEST CHART

AD-A156 394

CSM



ANALYSIS OF TWO-PARAMETER CONSTANT BACKGROUND
BORN INVERSION FOR ACOUSTIC SYNTHETIC DATA

by

Paul B. Violette

Partially supported by Sohio Petroleum Company,
the Consortium Project of the Center for Wave Phenomena,
and the Selected Research Opportunities Program of
the Office of Naval Research

Colorado School of Mines

Golden, Colorado 80401

Center for Wave Phenomena
Department of Mathematics
303/273-3559

DTIC FILE COPY

This document has been approved
for public release and unlimited
distribution is unlimited.

DTIC
JUL 10 1985
A



85 06 25 223

2
CWP-029



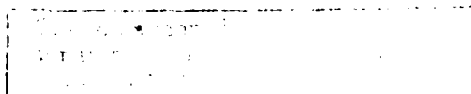
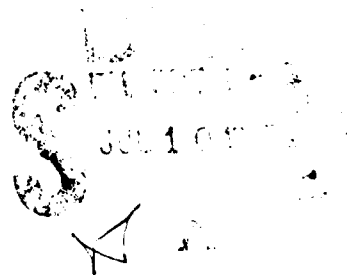
**ANALYSIS OF TWO-PARAMETER CONSTANT BACKGROUND
BORN INVERSION FOR ACOUSTIC SYNTHETIC DATA**

by

Paul B. Violette

**Partially supported by Sohio Petroleum Company,
the Consortium Project of the Center for Wave Phenomena,
and the Selected Research Opportunities Program of
the Office of Naval Research**

**Center for Wave Phenomena
Department of Mathematics
Colorado School of Mines
Golden, Colorado 80401
(303) 273-3557**



CONTENTS

ABSTRACT.....	i
GLOSSARY.....	ii
LIST OF FIGURES.....	iv
LIST OF TABLES.....	vi
PREFACE.....	vii
INTRODUCTION.....	1
DERIVATION OF THE FORWARD AND INVERSE EQUATIONS.....	4
Introduction.....	4
Derivation of the Integral Equation.....	4
Inversion of the Integral Equation for the Medium Parameters.....	8
DERIVATION OF THE SYNTHETIC DATA.....	13
Introduction.....	13
Derivation of the Single Interface Data.....	13
Derivation of the Double Interface Data.....	15
ARTIFACTS IN LINEAR INVERSION.....	19
Introduction.....	19
Examining the Differential Equation.....	19
Analysis of Single Interface Inversion Artifacts.....	21
Identification of Single Interface Inversion Artifacts.....	24
FIXED FREQUENCY SINGLE INTERFACE RECONSTRUCTIONS.....	26
Introduction.....	26
Interpretation of the Reconstructions.....	26
Increasing Velocity Reconstructions.....	28
Decreasing Velocity Reconstructions.....	31
Constant Velocity Reconstructions.....	32
Least-Squares Reconstructions.....	33
FIXED FREQUENCY DOUBLE INTERFACE RECONSTRUCTIONS.....	34
Introduction.....	34
Examples of Double Interface Reconstructions.....	35

CONTENTS (continued)

FIXED ANGLE INVERSION.....	39
Introduction.....	39
Reformulation of the Inversion.....	40
Examples of Fixed Angle Reconstructions.....	42
INVERSION ARTIFACTS REVISITED.....	46
Introduction.....	46
Analysis of Double Interface Artifacts.....	46
Inversion Artifacts and the Reference Velocity.....	53
CONCLUSIONS.....	58
ACKNOWLEDGMENTS.....	61
REFERENCES.....	62
APPENDIX A: TRANSFORMED GREEN'S FUNCTIONS.....	63
APPENDIX B: ONE-DIMENSIONAL FORWARD EQUATION.....	66
APPENDIX C: LEAST-SQUARES SOLUTION OVER TEMPORAL FREQUENCY.....	69
APPENDIX D: SINGLE INTERFACE, LINE SOURCE ACOUSTIC DATA.....	70
APPENDIX E: DERIVATION OF THE DOUBLE INTERFACE FORWARD MODEL.....	73
FIGURES.....	77

ABSTRACT

In this thesis, we examine the usefulness of the two-parameter Born inversion method of Clayton and Stolt (1981) under idealized conditions. We implement a constant background procedure to reconstruct line source synthetic data which simulate a stratified acoustic medium. Specifically, this investigation is an extension of the single interface work of Weglein, Violette and Eoho (1985) for double interface models. Since we use offset data to recover one-dimensional bulk modulus and density variations, this procedure is termed a 1.5 dimensional inversion. Implicit in these reconstructed acoustic profiles are errors related to the approximate inversion. Phase shifts inherent in the modeled wave field cause these inversion errors not only to propagate, but also to increase with depth. Since the model data are exact, we are able to examine the analytic expressions of these inversion artifacts. From this analysis, we develop an implementation which minimizes inversion errors. This is achieved by both preconditioning the offset data, and judiciously choosing a reference velocity in accordance with inversion goals. Both of these procedures however provide limited improvement, and we conclude that this constant background, frequency domain, method should be enhanced by more sophisticated algorithms. Specifically, we suggest the implementation of either a variable background procedure, or the refinement algorithm of Hagin and Cohen (1984).

Accession For	
NTIS GRA&I	<input checked="checked" type="checkbox"/>
DTIC TAB	<input type="checkbox"/>
Unannounced	<input type="checkbox"/>
Justification	
By	
Distribution /	
Availability Codes	
Dist	
A1	

GLOSSARY

a_1	bulk modulus variation
\tilde{a}_1	Fourier transformed bulk modulus variation
a_2	density variation
\tilde{a}_2	Fourier transformed density variation
A_1	coefficient in the forward equation
A_2	coefficient in the forward equation
c_r	reference velocity
c_n	medium velocities ($n = 1, 3$)
D_s	synthetic data
$G_r^+(x_g, 0 x', z', \omega)$	Green's function from scatterer to receiver
$G_r^+(x', z' x_g, 0, \omega)$	Green's function from source to scatterer
h, h_1	depth to the first interface
h_2	depth of the second interface below the first
k	wave number
k_{xg}	Fourier transformed horizontal receiver coordinate
k_{xs}	Fourier transformed horizontal source coordinate
k_{zg}	Fourier transformed vertical receiver coordinate
k_{zs}	Fourier transformed vertical source coordinate
k_r	wave number in the reference medium
k_x, k_y	horizontal components of wave number
k_z	vertical component of wave number
K	bulk modulus
K_r	bulk modulus in the reference medium
Q_n	arbitrary function related to the refl. coeff.
Q_n^*	arbitrary function related to the trans. coeff.

GLOSSARY (continued)

R_1	Rayleigh reflection coeff. at the first interface
R_2	Rayleigh reflection coeff. at the second interface
$S(\omega)$	Fourier transform of the source-time function
T	transmission loss through the layer
U	pressure wave field
U_r	reference wave field
V	scattering potential
x, y	horizontal coordinates
x'	horizontal coordinate of the scatterer
x_g	receiver (geophone) location at $z = 0$
x_h	half-offset coordinate at $z = 0$
x_m	midpoint coordinate at $z = 0$
x_s	source location at $z = 0$
z	vertical coordinate
z'	vertical coordinate of the scatterer
δ_n	ratio of adjacent densities
Δ_n	contrast between medium and reference velocities
ρ	density
ρ_r	density in the reference medium
ρ_n	medium densities ($n = 1, 3$)
ϕ_n	displacement potential
θ	angle of the wave vector with respect to the z -axis
ω	angular temporal frequency

LIST OF FIGURES

Figure		Page
1	Diagram of the single interface experiment.....	77
2	Shot record of a typical single interface forward model....	78
3	Diagram of the double interface experiment.....	79
4	Shot record of a typical double interface forward model....	80
5	Fixed frequency, increasing velocity, constant density, single interface reconstruction for all pre-critical data.	81
6	Fixed frequency, increasing velocity, constant density, single interface reconstruction for filtered data.....	82
7	Fixed frequency, increasing velocity, constant bulk modulus single interface reconstruction for all pre-critical data.	83
8	Fixed frequency, increasing velocity, constant bulk modulus single interface reconstruction for filtered data.....	84
9	Fixed frequency, increasing velocity, constant impedance, single interface reconstruction for all pre-critical data.	85
10	Fixed frequency, increasing velocity, constant impedance, single interface reconstruction for filtered data.....	86
11	Fixed frequency, decreasing velocity, constant density, single interface reconstruction for broadband data.....	87
12	Fixed frequency, decreasing velocity, constant density, single interface reconstruction for filtered data.....	88
13	Fixed frequency, constant velocity, single interface reconstruction for broadband data.....	89
14	Least-squares, constant density, single interface reconstruction for the input model of Figure 6.....	90
15	Fixed frequency, constant density, double interface reconstruction for 10% velocity changes.....	91
16	More highly filtered reconstruction of Figure 15.....	92
17	Fixed frequency, constant density, double interface reconstruction for 1% velocity changes.....	93
18	Fixed frequency, constant density, double interface reconstruction for 0.1% velocity changes.....	94

LIST OF FIGURES (continued)

Figure		Page
19	Fixed frequency, constant bulk modulus, double interface reconstruction for 10% velocity changes.....	95
20	Fixed frequency, constant bulk modulus, double interface reconstruction for 1% velocity changes.....	96
21	Fixed frequency, constant bulk modulus, double interface reconstruction for 0.1% velocity changes.....	97
22	Reconstruction of the model of Figure 18 but for a shallower second reflector.....	98
23	Reconstruction of the model of Figure 18 but for a deeper second reflector.....	99
24	Fixed angle reconstruction of the model of Figure 6.....	100
25	Fixed angle reconstruction of the model of Figure 15.....	101
26	Fixed angle reconstruction of the model of Figure 17.....	102
27	Fixed angle reconstruction of the model of Figure 18.....	103
28	Reconstruction of the model of Figure 26 but for a shallower second reflector.....	104
29	Reconstruction of the model of Figure 26 but for a deeper second reflector.....	105
30	Fixed angle, constant density, double interface, reconstruction for 0.1% and 10% velocity changes.....	106
31	Reconstruction of the model of Figure 30 but with the order of the velocity changes reversed.....	107
32	Fixed angle, constant density, double interface reconstruction with 1% velocity changes.....	108
33	Reconstruction of Figure 32 with the reference velocity equal to the layer velocity.....	109
34	Reconstruction of Figure 33 but for a deeper second reflector.....	110
35	Reconstruction of Figure 32 with the reference velocity equal to 3025 ft/sec.....	111
36	Reconstruction of Figure 35 but for a deeper second reflector.....	112

LIST OF TABLES

Table	Page
1 List of the maximum parameter amplitudes for Figures 32, 33, and 34.....	55

PREFACE

In seismic exploration, an energy source located at the Earth's surface initiates seismic waves which propagate through the subsurface. A portion of this seismic energy is reflected by inhomogeneities within the probed medium, and this reflected response is systematically measured along the Earth's surface. In general, the object of seismic exploration is to determine the nature of the subsurface from these geophysical data. That is, given knowledge about both the source and receivers, we hope to extract subsurface information. This information depends upon both the mathematical model used to describe the medium, and the method of inversion. In this investigation, we implement a method, founded in inverse scattering, for recovering both acoustic parameters.

In our method, we assume that subsurface parameter changes can be modeled as deviations about a known reference medium. Thus, as the incident wave field propagates through the medium, any variation of the wave field from the reference wave field is attributed to scattering. Expressing reflected energy as these scattering interactions establishes the mathematical framework for recovering subsurface information. Basic to any mathematical expression for wave propagation is a physical model describing the assumed nature of the medium. Typically, these expressions are partial differential equations which include spatially variant coefficients. Determining these coefficients determines the model parameters. As mentioned above, we assume an acoustic model and recover the corresponding bulk modulus and density variations.

Scattering theory is characterized by both the forward and inverse problems. In the forward problem, we specify the model parameters and

calculate the corresponding wave response. This procedure has been used in an iterative scheme to recover subsurface information, given a data set, we would: (1) calculate a forward response, (2) compare this synthetic response with the observed response, and (3) minimize the resulting model parameter differences through an iterative procedure. Inverse scattering however seeks to directly determine the model parameters from the observed data. These methods are constrained by the specific assumptions which characterize the model. In this thesis, we consider an approximate inversion scheme for directly recovering one-dimensional acoustic parameter variations.

Since this inversion scheme is approximate, subsurface phenomena are either incorrectly modeled, or not modeled at all. Specifically, our method is a linear procedure which ignores both multiple reflections and transmission losses. Furthermore, all reconstructed parameter changes are contaminated by linearization errors. We therefore focus our attention on the reliability of this direct inversion method.

INTRODUCTION

The goal of seismic inversion is to recover subsurface properties from surface reflection data. For a particular method, these recovered properties depend on the assumed nature of the probed medium. In this thesis, we examine the usefulness of a well known linear inversion procedure which extracts acoustic parameters from a stratified earth. Before discussing this method however, we outline the development of other related techniques.

Prior to the development of direct inversion procedures, structural inversion was accomplished by wave equation migration methods. These methods have been refined and are widely used today. Although wave equation migration methods can accurately locate subsurface reflectors, they can only qualitatively predict the sizes of corresponding impedance contrasts--hence the term structural inversion. Briefly, all wave equation migration methods rely on specific imaging assumptions to map subsurface reflectivity by backpropagating the recorded wave field. Recent survey books discuss both the theoretical background (Morgan, (1983)), and the available techniques (Berkhout, (1982) and Robinson, (1983)) of wave equation migration.

In a 1979 paper, Cohen and Bleistein present and implement a procedure for the direct inversion of the acoustic wave equation for a two-dimensional velocity profile. Expressing the forward equation as Green's theorem, they linearize the resulting integral equation and adopt a perturbative approach before inverting. This linearization admits two assumptions inherent in wave equation migration: (1) all reflection events are treated as primary reflections, and (2) a constant velocity medium lies above each reflector. As demonstrated by Cohen and Bleistein, the linearization does not seriously

impair their method. In fact, this direct inversion offers an improvement over the imaging techniques of wave equation migration. In direct inversion, not only are the reflectors imaged, but also the sizes of impedance changes are recovered within the linearization assumption. In effect, this inversion is a direct mapping procedure which assigns a value of acoustic velocity to a specific subsurface location. In subsequent work, Bleistein and Cohen (1982) present a three-dimensional inversion algorithm as well as implement their method for field data. Also, Hagin and Cohen (1984) refine the previous method to compensate for the effects of the linearization.

Both wave equation migration and the approximate inversion of Bleistein and Cohen utilize the conventional common-midpoint stacked section to simulate a coincident source-receiver configuration. The processing of this data however eliminates all information concerning the variation of the reflection coefficient with incident angle. Thus, these techniques cannot separate density variations from velocity or bulk modulus variations. As shown by Clayton and Stolt (1981) and Raz (1981), the above method of linear inversion provides the mathematical basis for recovering both velocity and density variations. Both papers present alternate approximate inversion algorithms for separating the components of impedance. Since both algorithms are formulated from Born theory, their underlying assumptions are identical to those of Cohen and Bleistein. In fact, both methods reduce to Cohen and Bleistein's result for zero offset and constant density. Hanson (1984) has demonstrated this in his discussion of the three methods.

Although the Born inverse methods of Clayton and Stolt, and Raz both rely on the angular dependence of the reflection coefficient to separate velocity and density variations, their approaches are different. The method

of Clayton and Stolt is similar to that of Cohen and Bleistein in that the data must be Fourier transformed over both time and the spatial coordinates. In contrast, Raz's procedure operates in the time domain. In implementing Raz's method, Hanson (1984) demonstrates that this time domain algorithm has greater stability than the frequency domain methods. According to Hanson, this improved stability derives from the operator's ability to accurately record amplitude variations with offset. (Frequency domain methods manipulate the entire wave field at once, and thus an accurate reference velocity is necessary for stability.) Hanson admits however that the careful picking of events, critical to Raz's method, is a tedious chore. Thus, although Raz's method leads to more accurate results, there is of yet no automated method of implementation.

In this investigation, we reformulate and implement the frequency domain method of Clayton and Stolt for synthetic data representing a stratified acoustic medium. Since we are reconstructing one-dimensional parameter variations, we require only a single common shot gather. To further simplify both the analysis and the computation of the inversion, we consider a constant background reference medium. By examining such a rudimentary problem, we are able to focus on the reliability of two-parameter, constant background, Born inversion under idealized conditions. We remark also that this thesis is organized as a research progression which represents the evolution of our understanding.

DERIVATION OF THE FORWARD AND INVERSE EQUATIONS

Introduction

In this chapter, we derive an approximate technique for the direct inversion of the density and bulk modulus variations of a stratified acoustic earth. As mentioned above, we reformulate the method of Clayton and Stolt (1981) to accommodate a one-dimensional medium. We therefore present their general result first. In their paper, Clayton and Stolt express the observed wave field as a Lippmann-Schwinger equation which represents the sum of all scattering interactions in a two-dimensional acoustic medium. The resulting integral equation is equivalent to the Green's theorem expression presented by Cohen and Bleistein (1979). To invert this forward equation, Clayton and Stolt assume that all subsurface parameter variations are small and apply the first Born approximation. This procedure establishes an approximate linear relationship between the medium variations and the observed data, and it is identical to the linearization inherent in the method of Cohen and Bleistein. Therefore, although the notation of this derivation is similar to that of Clayton and Stolt, the derivation of the forward equation adheres largely to the work of Cohen and Bleistein. The inversion of the resulting integral equation however relies on the insights of Clayton and Stolt.

Derivation of the Integral Equation

Wave propagation in a variable density, two-dimensional acoustic medium is governed by the equation:

$$LU = \left[\nabla \cdot \frac{1}{\rho} \nabla + \frac{\omega^2}{K} \right] U = -\delta(\mathbf{x}_g - \mathbf{x}_s) \delta(z_s) S(\omega) \quad (1)$$

where L is the linear wave operator defined by the middle expression of this dual equality, U is the pressure wave field, ρ is the density, K is the bulk modulus, and $S(\omega)$ is the Fourier transform of the source-time function. In this and other equations, the subscripts g and s denote the receiver and the source locations, respectively. The inversion of this equation for the acoustic medium parameters is in general a nonlinear problem. To overcome this inherent nonlinearity, we express solutions as perturbations about a reference medium where analytic solutions are known. The equation representing the response of the unperturbed medium is given by

$$L_r U_r = \left[\nabla \cdot \frac{1}{\rho_r} \nabla + \frac{\omega^2}{K_r} \right] U_r = -\delta(\mathbf{x}_g - \mathbf{x}_s) \delta(z_s) S(\omega) \quad (2)$$

where L_r is the linear operator in the reference medium, U_r is the field in the reference medium, and ρ_r and K_r are the reference medium parameters.

We now rewrite equation (1) so as to introduce the scattering potential $V(\mathbf{x}, z)$ and its corresponding perturbations a_1 and a_2 . Recognizing that the scattering potential which initiates the scattered wave field is merely the difference of the linear operators, L and L_r , we add and subtract L_r to L in equation (1). After collecting terms, we find

$$\left[\nabla \cdot \frac{1}{\rho_r} \nabla + \frac{\omega^2}{K_r} + V(x, z) \right] U = -\delta(x_g - x_s) \delta(z_s) S(\omega) \quad (3)$$

where

$$a_1 = \frac{K_r}{K} - 1, \quad a_2 = \frac{\rho_r}{\rho} - 1 \quad (4)$$

and

$$V(x, z) = \frac{\omega^2 a_1}{K_r} + \nabla \cdot \frac{a_2}{\rho_r} \nabla \quad (5)$$

Although a_1 and a_2 are dimensionless parameters, we consider them as the medium variations and seek their values in the inversion process. To recover the actual parameter variations, we need only substitute the inverted values of a_1 and a_2 into equations (4) and solve for ρ and K .

The wave field represented by U (recorded at the geophone location x_g due to the source at location x_s) is the simple integration of all scatterers over the entire subsurface area. This total wave field is the sum of the direct wave field traveling from source to receiver and the wave field reflected from within the subsurface. The seismic experiment we are considering consists only of the measurement of the scattered or reflected wave field. We therefore express the observed field or the data as the difference of the total field and the field in the reference medium

$$D(x_g, x_s, \omega) = (U - U_r) S(\omega) \quad (6)$$

where U_r is now thought of as the direct wave. The presense of $S(\omega)$ acknowledges that the data necessary for any subsequent inversion are implicitly band-limited.

To establish a relationship between the data and the parameter

variations, we subtract equation (2) from equation (3)

$$\left[\nabla \cdot \frac{1}{\rho_r} \nabla + \frac{\omega^2}{K_r} \right] D = -V(U_r + D)S(\omega) \quad (7)$$

In order to provide an approximate linear relationship between the surface observations and the perturbations, we apply the first Born approximation and replace the total field by the field in the reference medium. As always, the Born approximation requires that the perturbations and hence the scattering potential remain small. We are justified in ignoring the product VD appearing on the right hand side of equation (7) as it is of lower order than the product VU_r (Bleistein, 1984). Therefore, the linearized equation is

$$\left[\nabla \cdot \frac{1}{\rho_r} \nabla + \frac{\omega^2}{K_r} \right] D = -VU_r S(\omega) \quad (8)$$

In the language of theoretical physics, the above procedure is equivalent to truncating the Born series representation of equation (7) after the second term. By applying this linearization, we are forcing the inversion to model all observed data as primary reflections. The result of this is that the inversion cannot properly interpret both transmission losses and multiple reflections. The addition of other nonlinear terms of the Born series would include such phenomena in the forward equation, but the inherent nonlinearity would preclude a direct inversion.

It is convenient to express equation (8) as an integral equation which

incorporates the Green's function representations of the incident and the scattered fields

$$D(\mathbf{x}_g, \mathbf{x}_s, \omega) = \int_{-\infty}^{\infty} d\mathbf{x}' \int_{-\infty}^{\infty} dz' G_r^+(\mathbf{x}_g, 0 | \mathbf{x}', z', \omega) \cdot V(\mathbf{x}', z', \omega) G_r^+(\mathbf{x}', z' | \mathbf{x}_s, 0, \omega) S(\omega) \quad (9)$$

In order to successfully recover the components of reflectivity, we have considered wave motion in a two-dimensional medium. In keeping with the method of Clayton and Stolt (1981), we consider two-dimensional Green's functions in the above integral equation. The first Green's function in this expression represents the wave propagating from the scatterer location to the receiver location. Similarly, the second Green's operator corresponds to propagation from the source location to the scatterer location. Both Green's operators represent the outgoing solutions in the reference medium as indicated by the "+" sign and are derived in Appendix A.

According to equation (9), the surface wave field can be determined if the parameter variations a_1 and a_2 are known. Equation (9) is therefore often referred to as a forward equation. Our goal is to invert this equation so that the parameter variations are expressed in terms of the known data.

Inversion of the Integral Equation for the Medium Parameters

For our specific inversion scheme, we are considering only constant background reference parameters, ρ_r and K_r . This approach allows a direct inversion of equation (9) since the Green's functions have an exact analytic

form.

Substituting equation (5) into equation (9), we find

$$D(\mathbf{x}_g, \mathbf{x}_s, \omega) = 1/\rho_r \int_{-\infty}^{\infty} d\mathbf{x}' \int_{-\infty}^{\infty} dz' G_r^+(\mathbf{x}_g, 0 | \mathbf{x}', z', \omega) \\ \cdot \left[k_r^2 a_1(\mathbf{x}', z') + \nabla \cdot \mathbf{a}_2(\mathbf{x}', z') \nabla \right] G_r^+(\mathbf{x}', z' | \mathbf{x}_s, 0, \omega) S(\omega) \quad (10)$$

where $k_r = \omega/c_r$. Following the derivation of Clayton and Stolt, we integrate the density term by parts to obtain

$$D(\mathbf{x}_g, \mathbf{x}_s, \omega) = \\ 1/\rho_r \int_{-\infty}^{\infty} d\mathbf{x}' \int_{-\infty}^{\infty} dz' \{ k_r^2 a_1(\mathbf{x}', z') G_r^+(\mathbf{x}_g, 0 | \mathbf{x}', z', \omega) G_r^+(\mathbf{x}', z' | \mathbf{x}_s, 0, \omega) \\ - \mathbf{a}_2(\mathbf{x}', z') \nabla G_r^+(\mathbf{x}_g, 0 | \mathbf{x}', z', \omega) \cdot \nabla G_r^+(\mathbf{x}', z' | \mathbf{x}_s, 0, \omega) \} S(\omega) \quad (11)$$

where we eliminate the boundary terms by assuming that the scattering potential is of bounded support. Fourier transforming over both source and receiver locations gives

$$\tilde{D}(\mathbf{k}_{xg}, \mathbf{k}_{xs}, \omega) = \\ 1/\rho_r \int_{-\infty}^{\infty} d\mathbf{x}' \int_{-\infty}^{\infty} dz' \{ k_r^2 a_1(\mathbf{x}', z') \tilde{G}_r^+(\mathbf{k}_{xg}, 0 | \mathbf{x}', z', \omega) \tilde{G}_r^+(\mathbf{x}', z' | \mathbf{k}_{xs}, 0, \omega) \\ - \mathbf{a}_2(\mathbf{x}', z') \nabla \tilde{G}_r^+(\mathbf{k}_{xg}, 0 | \mathbf{x}', z', \omega) \cdot \nabla \tilde{G}_r^+(\mathbf{x}', z' | \mathbf{k}_{xs}, 0, \omega) \} S(\omega) \quad (12)$$

where the tilde denotes the spatial Fourier transform.

In Appendix A, we derive the analytic expressions for the Green's

functions represented in equation (12). Inserting these results into equation (12) and applying the differential operators yields

$$\begin{aligned} \tilde{D}(k_{xg}, k_{xs}, \omega) = \frac{\rho_r}{4k_{zg}k_{zs}} \left[k_r^2 W_1(k_{xg} - k_{xs}, -k_{zg} - k_{zs}) \right. \\ \left. + (k_{zg}k_{zs} - k_{xg}k_{xs}) W_2(k_{xg} - k_{xs}, -k_{zg} - k_{zs}) \right] S(\omega) . \quad (13) \end{aligned}$$

This expression establishes an approximate linear relationship between the Fourier transform of the scattered wave field and the Fourier transform of the medium variations. As pointed out by Clayton and Stolt, there is more than enough information inherent in the data to allow an inversion for the medium parameters.

In this investigation, we reduce the dimensionality of the problem by one. That is, we confine our attention to the situation where the medium parameters depend only on the depth variable. As a result, the offset surface reflection data must be collected on a line-source, line-receiver configuration, and only one shot record is required. Since the data varies in two directions while the medium varies in only one, we term this a 1.5 dimensional inversion. In Appendix B, equation (13) is recast in terms of the one-dimensional medium parameters to give

$$\tilde{D}(k_z, \omega) = \frac{-\rho_r}{4k_z^2} \left[k_r^2 W_1(-2k_z) + (2k_z^2 - k_r^2) W_2(-2k_z) \right] S(\omega) . \quad (14)$$

Before inverting the above equation, we must precondition the observed data. If the data were a recorded time section, then we would have to

Fourier transform the data with respect to x , and express the result as a function of k_z . This second processing step would be achieved by applying the dispersion relation and resampling the resulting function for appropriate values of Δk_z . Additionally, we would also have to deconvolve the source function $S(\omega)$ within the temporal bandwidth before inverting. This procedure would require detailed knowledge of the source function which also might be used in a weighted least squares solution. Furthermore, for a fixed angle implementation of this method on field data, the deconvolution of the source function would be critical for accurate inversion results. For the purposes of this investigation, the above processing steps are unnecessary since we are considering only synthetic data, we therefore express our synthetic data directly as a function of k_z and allow all temporal frequencies to be of equal amplitude. Thus, the forward equation becomes

$$\tilde{D}_s(k_z, \omega) = A_1(k_z, \omega) \mathcal{H}_1(-2k_z) + A_2(k_z, \omega) \mathcal{H}_2(-2k_z) \quad (15)$$

where $\tilde{D}_s(k_z, \omega)$ represents the synthetic data, and

$$A_1(k_z, \omega) = \frac{-\rho_r \omega^3}{4k_z^3 c_r^3} \quad (16)$$

$$A_2(k_z, \omega) = \frac{-\rho_r}{2} - A_1(k_z, \omega) .$$

Since the medium variations, a_1 and a_2 , are independent of ω , we may compute A_1 , A_2 , and \tilde{D}_s for two distinct values of ω and solve for a_1 and a_2 directly. With temporal frequency as the free parameter, the inversion relations are simplified to become:

$$\tilde{u}'_1(-2k_z) = \tilde{u}'_2(-2k_z) - \frac{4c_r^2 k_z^2}{\rho_r} \left[\frac{\tilde{D}_s(k_z, \omega_1) - \tilde{D}_s(k_z, \omega_2)}{\omega_1^2 - \omega_2^2} \right] \quad (17a)$$

$$\tilde{u}'_2(-2k_z) = \frac{2}{\rho_r} \left[\frac{\omega_1^2 \tilde{D}_s(k_z, \omega_1) - \omega_2^2 \tilde{D}_s(k_z, \omega_2)}{\omega_1^2 - \omega_2^2} \right] \quad (17b)$$

By expressing the inversion relations in this manner, we observe the near singular behavior of these functions as ω_1 becomes close to ω_2 . To express \tilde{u}'_1 and \tilde{u}'_2 as functions of depth, we inverse Fourier transform equations (17).

Since the choice of input frequencies is somewhat arbitrary, we could attempt a least-squares or an average least-squares solution over frequency values. This approach would only provide improved results if noisy synthetic or real data sets were being inverted. In any case, the least-squares result is given by the solution to the equations:

$$\begin{bmatrix} \sum A_1^2 & \sum A_1 A_2 \\ \sum A_1 A_2 & \sum A_2^2 \end{bmatrix} \begin{bmatrix} \tilde{u}_1 \\ \tilde{u}_2 \end{bmatrix} = \begin{bmatrix} \sum A_1 \tilde{D}_s \\ \sum A_2 \tilde{D}_s \end{bmatrix} \quad (18)$$

where the summations are taken over values of ω . The derivation of the preceding result is given in Appendix C.

DERIVATION OF THE SYNTHETIC DATA

Introduction

In this chapter, we examine the synthetic data which we implement to test the inversion. We choose an exact analytic form for the data so as to create a controlled experiment. This control not only provides a more confident interpretation of subsequent reconstructions, but also it simplifies the mathematical analysis. To conform to the requirements of the inversion, this synthetic data is computed directly in the Fourier domain.

Since we are considering a one-dimensional medium, the synthetic data is constrained by a line-source, line-receiver configuration. Even though the medium only varies with depth, the data varies with offset. This feature of the data provides the information necessary for the separation of the components of impedance. The specific form of this data is derived from the point-source results given by Ewing, Jardetzky, and Press (1957). In our derivation, we follow their approach and develop expressions for both single and double interface models. In summary, the resulting analytic expressions represent the two-dimensional Fourier transform of the wave field scattered from a stratified acoustic medium and collected at many offsets.

Derivation of the Single Interface Data

As an initial attempt, we consider an analytic expression which represents the response of a single interface. This single interface situation is modeled by joining two acoustic constant velocity half-spaces.

Since we are inverting for one-dimensional parameter variations, we require only one shot record, the experiment providing this data is illustrated in Figure 1. The point source response of this model is derived by Ewing, Jardetzky, and Press, and its corresponding line-source, line-receiver expression is derived in Appendix D:

$$\tilde{D}_s(k_x, \omega) = \left[\frac{\delta \nu_1 - \nu_2}{\delta \nu_1 + \nu_2} \right] \exp(-2\nu_1 h) \quad (19)$$

where h is the depth of the reflector below the source-receiver line, $\delta = \rho_2/\rho_1$, and

$$\nu_1 = i \sqrt{\frac{\omega^2}{c_1^2} - k_x^2}, \quad \nu_2 = i \sqrt{\frac{\omega^2}{c_2^2} - k_x^2}. \quad (20)$$

The right side of equation (19) is often referred to as the plane-wave reflection coefficient for the single interface model (Frisk, 1979), and this quantity is a function of both the incident angle and the input frequency.

For our purposes, equation (19) must be written as a function of k_z . This is achieved by observing the dispersion relation, and the resulting expression is

$$\tilde{D}_s(k_z, \omega) = \frac{\delta k_z - \sqrt{k_z^2 + \omega^2 \Delta_1}}{\delta k_z + \sqrt{k_z^2 + \omega^2 \Delta_1}} \exp(-2i k_z h) \quad (21)$$

$$\text{where } \Delta_1 = \frac{1}{c_s^2} - \frac{1}{c_r^2}, \quad \text{and} \quad \frac{\omega^2}{c_r^2} = k_x^2 + k_z^2.$$

To view the shot record associated with this analytic expression, we have only to apply a two-dimensional FFT to equation (19). The result of this procedure for a particular input model is shown in Figure 2.

Derivation of the Double Interface Data

As an extension of this single interface situation, we consider a double interface model. Although this model includes the same assumptions as the single interface case, there are additional features which may provide insight. Specifically, the two-interface data will include such nonlinear effects as multiple reflections and transmission losses. By inverting this forward model, we should be able to examine the accuracy with which our linear inversion reconstructs nonlinear data. Furthermore, as the depth and complexity of the probed medium increases, Born theory predicts that the associated error will increase. Therefore, by examining this two-interface model, we investigate the validity of our linear inversion where it is predicted to breakdown.

For the two-interface forward model, we consider two constant velocity acoustic half-spaces, separated by a constant velocity acoustic layer. As with the one-interface model, the source and receivers are located in the upper half-space. The geometry for this model is illustrated in Figure 3. To derive the analytic expression, we follow the method of Ewing, Jardetzky, and Press and determine the displacement potential of the upgoing waves at the receiver depth. This is accomplished by solving the system of equations which satisfy the boundary conditions at each interface. The details of

this derivation are given in Appendix E. Thus, the synthetic data for the two-interface model is given by the plane-wave reflection coefficient

$$\tilde{D}_s(k_x, \omega) = \left[\frac{R_1 + R_2 \exp(-2\nu_2 h_2)}{1 + R_1 R_2 \exp(-2\nu_2 h_2)} \right] \exp(-2\nu_1 h_1) , \quad (22)$$

where R_1 and R_2 are the Rayleigh reflection coefficients at the first and second interfaces, respectively:

$$R_1(k_x, \omega) = \frac{\delta\nu_1 - \nu_2}{\delta\nu_1 + \nu_2} , \quad R_2(k_x, \omega) = \frac{\delta\nu_2 - \nu_3}{\delta\nu_2 + \nu_3} . \quad (23)$$

As before, we define: $\delta_1 = \rho_2/\rho_1$, $\delta_2 = \rho_3/\rho_2$, and

$$\nu_1 = i \sqrt{\frac{\omega^2}{c_1^2} - k_x^2} , \quad \nu_2 = i \sqrt{\frac{\omega^2}{c_2^2} - k_x^2} , \quad \nu_3 = i \sqrt{\frac{\omega^2}{c_3^2} - k_x^2} . \quad (24)$$

If the model parameters are matched up across either interface, equation (22) reduces to equation (19). This feature allows us to implement equation (22) for either the single or the double interface models.

As in the single interface model, we can express equation (22) as a function of k_z , this is the analytic form required by the inversion relations and is accomplished by rewriting equations (24) as

$$\nu_1 = i \sqrt{k_z^2 + \omega^2 \Delta} \quad , \quad \nu_2 = i \sqrt{k_z^2 + \omega^2 \Delta_1} \quad , \quad \nu_3 = i \sqrt{k_z^2 + \omega^2 \Delta_2} \quad (25)$$

where

$$\Delta = \frac{1}{c_1^2} - \frac{1}{c_r^2} \quad , \quad \Delta_2 = \frac{1}{c_2^2} - \frac{1}{c_r^2} \quad . \quad (26)$$

To accommodate the Born approximation, we may choose to consider a form of equation (22) which excludes multiple reflections. This expression is derived in Appendix E and is given by

$$\tilde{D}_s(k_x, \omega) = R_1 \exp(-2\nu_1 h_1) + R_2 (1 - R_1^2) \exp[-2(\nu_1 h_1 + \nu_2 h_2)] \quad (27)$$

where $(1 - R_1^2)$ represents the transmission loss through the layer.

An example of a shot record for this two-interface model is shown in Figure 4. This result was computed by applying a two-dimensional FFT to equation (22).

Before inverting equation (15) for the data represented by equations (21) and (22), we note that the synthetic data and the inversion are based on two different Green's function conventions. Equating the conventions used by Clayton and Stolt (1981), and Ewing, Jardetzky, and Press (1957) gives a new form to the forward equation:

$$A_1(k_z, \omega) = \frac{-\pi \omega^2}{k_z^2 c^2}$$

(28)

$$A_2(k_z, \omega) = -2\pi - A_1(k_z, \omega) \quad .$$

Thus, to invert equation (15) for the synthetic data discussed in this chapter, we must replace equation (16) by equation (28).

ARTIFACTS IN LINEAR INVERSION

Introduction

Before considering examples of reconstructed acoustic profiles, we examine the source of artificial parameter variations which contribute to two-parameter reconstructions. As mentioned above, our inversion scheme is based on a linearization of the nonlinear relationship between the model parameters and the observed data. This linearization produces errors in all subsequent reconstructions. For instance, a variation in one acoustic parameter will generate a false variation in its reconstructed counterpart. We term these artificial parameter changes, inversion artifacts. In this chapter, we discuss the source of these artifacts in the context of linear inverse theory. Specifically, we outline the method developed by Weglein, Violette, and Keho (1985) for both identifying and reducing single interface artifacts. (In fact, this thesis represents the double interface extension of their work.) In this chapter, most of our conclusions are derived from the analytic form of the synthetic data. We begin however with a general analysis of the differential equations relevant to our method.

Examining the Differential Equation

Consider the differential equation governing wave motion in a stratified acoustic medium

$$\left[\frac{\partial^2}{\partial x^2} + \frac{\partial^2}{\partial z^2} + \frac{\omega^2}{c_r^2} + \frac{\omega^2}{c_r^2} a_1 + \frac{\partial}{\partial z} \left[a_2 \frac{\partial}{\partial z} \right] \right] U(x, z, \omega) = 0 \quad . \quad (29)$$

The spatially transformed wave field satisfies

$$\left[\frac{\partial^2}{\partial z^2} - k_x^2 + \frac{\omega^2}{c_r^2} + \frac{\omega^2}{c_r^2} a_1 + \frac{\partial}{\partial z} \left[a_2 \frac{\partial}{\partial z} \right] \right] \tilde{U}(k_x, z, \omega) = 0 \quad (30)$$

and can be rewritten as

$$\left[\frac{\partial^2}{\partial z^2} + k_z^2 + V(z, \omega) \right] \tilde{U}(k_x, z, \omega) = 0 \quad (31)$$

where $\omega^2/c_r^2 = k_x^2 + k_z^2$, and

$$V(z, \omega) = \frac{\omega^2}{c_r^2} a_1 + \frac{\partial}{\partial z} \left[a_2 \frac{\partial}{\partial z} \right] \quad (32)$$

By applying the Born approximation, we assume that the total field, U , can be replaced by the field in the reference medium, U_r . Since the field in the reference medium satisfies

$$\left[\frac{\partial^2}{\partial z^2} + k_z^2 \right] U_r(k_x, z, \omega) = 0 \quad (33)$$

it is clear that equation (31) will only be well approximated by equation (33) when

$$k_z^2 \tilde{U} \gg V(z, \omega) \tilde{U} \quad (34)$$

For the fixed frequency implementation outlined in the previous chapter, k_z values can range from zero to ω_1/c_r where ω_1 is the smaller of the two

chosen angular frequencies. Thus, for any scattering potential, V , there exists k_z values near zero for which equation (34) is not satisfied, and the Born approximation is inappropriate. Reconstructed profiles which utilize low k_z data values will be degraded by the inherent nonlinear processes. We should therefore eliminate low k_z data values prior to inversion. In effect, preconditioning the offset data in this manner allows the linear inversion to produce more exact results.

Analysis of Single Interface Inversion Artifacts

In the previous section, we examined the differential equation to determine which portion of the data in the wavenumber domain best satisfies the assumptions in our linear inversion. We found that even though no wavenumber component of the data is independent of nonlinear effects, certain portions are more strongly influenced than others. To better understand this observation, we now consider an analytic expression for the artifacts generated by exact synthetic model data. As a simple example, we substitute the single interface result given by equation (21) into the inversion relations given by equations (17).

Consider the situation where only the bulk modulus varies across the interface. In this case, the exact value of the density variation a_1 is zero. The reconstructed value of a_1 is determined by substituting $\tilde{D}_s(k_z, \omega)$ into equation (17b) with ρ_1 set equal to ρ_2 :

$$a_2'(-2k_z) =$$

$$\frac{2}{\rho_r} \left[\frac{\omega_2^3 \left[\frac{k_z - \sqrt{k_z^2 + \omega_1^2 \Delta}}{k_z + \sqrt{k_z^2 + \omega_1^2 \Delta}} \right] - \omega_1^3 \left[\frac{k_z - \sqrt{k_z^2 + \omega_2^2 \Delta}}{k_z + \sqrt{k_z^2 + \omega_2^2 \Delta}} \right]}{\omega_1^3 - \omega_2^3} \right] \exp(-2ik_z h). \quad (35)$$

This relation represents a density change at $z = h$ and is identified as the source of the density artifact. After examining this equation, we conclude that this density artifact will vanish only if Δ equals zero. Since Δ is zero only for both constant density and bulk modulus, it is obvious that our inversion scheme will always predict a density variation for the case of constant density. Alternatively, it can be shown that a similar substitution of the data for a constant bulk modulus model into equation (17a) leads to a false bulk modulus change. Therefore, even though the synthetic data has an exact form, the reconstructed acoustic profiles contain artificial variations which are traced to the linearization of the inversion.

To understand the nature of these artifacts, we examine equation (35) which represents the artificial density variation generated by a bulk modulus change. We notice that if we choose ω_1 close to ω_2 , and if

$$k_z^2 \gg \omega^2 \Delta, \quad (36)$$

then the density artifact diminishes, that is, $a_2' \rightarrow 0$. The criterion expressed by equation (36) is identical to equation (34) with density held constant. As before, we satisfy this requirement by eliminating low k_z

offset data prior to inversion. By performing a similar analysis on the bulk modulus artifact generated by a density change, we confirm that the requirement suggested by equation (36) will indeed reduce this artifact as well. We conclude that the condition initiated by our analysis of the differential equation is verified by our analysis with the synthetic data.

If we eliminate ω^2 from both sides of equation (36), we obtain

$$\cos^2 \theta \gg \left| \frac{\frac{c_1^2}{c_2^2} - 1}{\frac{c_1^2}{c_2^2}} \right| \quad (37)$$

where θ represents the angle of incidence with respect to the z-axis. The condition expressed by equation (37) suggests that the data corresponding to large θ are responsible for the inversion artifacts. Eliminating low k_z data is physically equivalent to excluding large θ data from the inversion. Note also, when $c_1 < c_2$, equation (37) becomes $\cos^2 \theta \gg \cos^2 \theta_c$ where θ_c represents the critical angle. To satisfy this condition, we must insure that $\theta < \theta_c$ which precludes the use of post-critical data. This observation is not surprising as the reflection coefficient becomes imaginary with modulus equal to one for $\theta > \theta_c$. Equation (37) however demands more than just the simple elimination of inhomogeneous waves from the inversion. To satisfy equation (37), we must eliminate the incident angles which correspond to a large scattering potential. By permitting these angles to contribute to the inversion, we are allowing the scattering potential to become large. This result violates the primary assumption which supports the applicability of the first Born approximation. Therefore, to diminish artificial parameter variations, we should eliminate the data which are characterized by large incident angles since these data correspond to a

significant scattered wave field.

In his two-parameter Born inversion scheme, Raz (1981) linearizes the acoustic reflection coefficient to obtain stable results. In implementing Raz's method, Hanson (1984) remarks that the reliability of this method rests largely on the accuracy of this approximation. In fact, Hanson's results are favorable only when the variation in the reflection coefficient is small. At large angles, the reflection coefficient deviates appreciably from the linearized expression, and the method fails. As mentioned by Clayton and Stolt, the amplitude information inherent in offset data allows the proper separation of the components of impedance. The above results however suggest that the large θ information can seriously degrade reconstructed acoustic profiles. We conclude that the accuracy of these methods relies not only on the inherent variation in the reflection coefficient, but also on the suitability of the Born approximation in representing this offset information. Later, we will consider synthetic examples which illustrate this apparent contradiction.

Identification of Single Interface Inversion Artifacts

In this chapter, we have presented the method of Weglein, Violette and Keho (1985) for enhancing the interpretability of reconstructed acoustic profiles. As mentioned above, this is accomplished by preconditioning the input data so as to minimize the effects of nonlinear processes. In their work, Weglein, Violette, and Keho also discuss a method for identifying these single interface artifacts; we outline this method below. Given a data set, we would run the inversion for two different k_z bandwidths. The data for the initial inversion would include all permissible k_z values while

the second inverted data set would be filtered to eliminate low k_z values. Since the low k_z data is highly dependent on nonlinear processes, the broadband reconstruction would be less reliable than the band-limited reconstruction. By comparing these reconstructions, we could identify the artifact as that variation whose relative amplitude decreased most rapidly between reconstructions. This artifact could then be ignored in a subsequent interpretation. In the following chapters, we will examine the usefulness of this procedure for identifying both single and double interface artifacts.

FIXED FREQUENCY SINGLE INTERFACE RECONSTRUCTIONS

Introduction

In this chapter, we examine the reconstructed acoustic profiles of the single interface synthetic data discussed in Chapter 2. Drawing on the analysis of the previous chapter, we implement a method for both reducing and identifying artificial parameter variations. In all these reconstructions, the reference velocity is chosen to be the velocity in the first medium. Consequently, the Born-predicted locations of the reconstructed parameter variations are always correct, and the Born-related artifacts only affect the amplitudes of the reconstructions. In the subsequent examples, we not only consider the deficiencies of our linear theory, but also we emphasize the role of the angularly dependent reflection coefficient in recovering both acoustic parameters.

Interpretation of the Reconstructions

Due to limitations implicit in conventional acquisition techniques, seismic data is band-limited at both ends of the spectrum. This loss of information impairs all subsurface reconstructions provided by direct inversion procedures. Specifically, the absence of high spatial frequencies limits the resolution of subsequent images--structural variation within the high frequency limit is not detected. An equally serious limitation is created by the loss of low frequency information. The missing low spatial frequencies contain information about the background or the absolute trend of the medium. As a result of this limitation, all reconstructed parameter

changes are signaled by band-limited step functions which deviate about a constant background medium. The amplitudes and the directions of actual parameter changes can be inferred from these step functions, but slowly varying information cannot be directly recovered. By examining the impulse response of a layered earth model for several bandwidths, Hanson (1984) has demonstrated the limitations implicit in band-limited data.

For interpretational purposes, Bleistein and Cohen (1982) choose to process the data for the derivative of the variation rather than the variation itself. This result arises from two observations: (1) both the amplitude and the direction of a parameter change are more easily extracted from a band-limited delta function than from a band-limited step function, and (2) the strength of a parameter change can be directly estimated from its corresponding band-limited delta function (Mager and Bleistein, (1979)). In this investigation, we follow the suggestion of Bleistein and Cohen and process for the normal derivative of the perturbations. Since all reconstructions are contaminated by artifacts of the linear inversion, we are not concerned with relating these reconstructed amplitudes to the actual input parameter changes. We note however that the peak amplitudes of these sinc-like functions are proportional to the spatial bandwidth (Mager and Bleistein, (1979)). In presenting the reconstructions, we normalize the reconstructed profiles to the largest peak value of a_1 or a_2 and list the corresponding maximum values. This feature aids in the comparison of different reconstructions. As a general rule, we may only compare the amplitudes of different reconstructed profiles if their spatial bandwidths are equivalent.

Increasing Velocity Reconstructions

In this section, we consider the inverted output of three different increasing velocity input models. These models simulate : (1) constant density, (2) constant bulk modulus, and (3) constant normal incidence impedance structures. Listed with each reconstruction are the input velocities in feet per second, the input densities in grams per cubic centimeter, the maximum incident angle in degrees, and the reflector depth in feet. Also included is a plot of the plane-wave reflection coefficient with offset. This plot not only demonstrates the nature of the specific reflection coefficient, but also it indicates the amount of offset data included in the inversion. Note that when k_x exceeds the smallest wavenumber in either medium, the reflection coefficient becomes imaginary. We therefore plot the reflection coefficient up to this limit.

In these examples temporal frequency is the free parameter, and the two input frequencies are listed (in Hz) with the model parameters. The smaller of these two frequencies determines the maximum k_z value: $k_{zmax} = \omega_1/c_r$. The lower limit of the k_z bandwidth is fixed by the maximum offset allowed in the inversion: $k_{zmin} = k_r \cos \theta_{max}$. This fact follows from our fixed frequency formulation. By fixing frequency, we must sweep through a range of incident angles to generate a suite of k_z values. This method for establishing a spatial bandwidth has its shortcomings. For instance, if we reduce offset by restricting θ , then we necessarily eliminate some low spatial frequencies from the inversion. In this implementation, the bandwidth is determined by both the choice of input frequencies and the maximum offset included in the inversion.

To conform to the seismic bandwidth, we generally do not invert for

frequencies much larger than 60 Hz. Also, we choose the input frequencies rather close together since: (1) Born-related artifacts are reduced, and (2) we only compute the inversion for k_z values corresponding to the smaller of the two input frequencies.

As a first model, we consider a 10% velocity increase with density held constant. To demonstrate the artificial density variation produced by a bulk modulus change, we invert this model with all pre-critical offsets included in the data. This reconstruction is shown in Figure 5. As expected, the reconstructed bulk modulus predicts the proper parameter change while the reconstructed density variation records a substantial artifact. This artifact is a plot of the Fourier transform of equation (35). As explained in the previous chapter, the origin of this artifact can be traced to the behavior of the reflection coefficient at far offsets. The plot of the reflection coefficient for the data inverted in Figure 5 details this nonlinear behavior. To reduce this artificial density variation, we have only to eliminate the far offset data which are inconsistent with the Born approximation. The reconstructed profiles for this case are presented in Figure 6. Notice that the plot of the reflection coefficient demonstrates the reduction of offset data by an angle of 10 degrees. Clearly, the density artifact has diminished relative to the actual bulk modulus variation. We note however that we have sacrificed some low spatial frequencies by discarding some offset information. As mentioned above, by reducing the spatial bandwidth, we necessarily reduce the amplitudes of the reconstructed parameter variations. Therefore, by adhering to the condition of equation (34), we have provided an interpretable acoustic profile for a 10% velocity change.

The preceding example also demonstrates the artifact identification

procedure of Weglein, Violette, and Keho (1985). By comparing the reconstructions of Figures 5 and 6, we observe that the relative amplitude of the density variation has diminished more rapidly than the bulk modulus variation. Thus, we identify the density change as an artifact of the linear inversion.

As a second example, we examine the inverted profiles of an input model corresponding to a 10% velocity increase for constant bulk modulus: $c_1^3 \rho_1 = c_2^3 \rho_2$. To view the associated bulk modulus artifact, we run the inversion for data which includes all pre-critical offsets (see Figure 7). As before, we reduce the Born-related artifact by excluding the far offset (low k_z) data from the inversion (see Figure 8). Once again, we acknowledge that this procedure serves to diminish the relative amplitude of the artifact and could be used as an artifact identification procedure. This reconstruction however has a different character from the previous example. By comparing Figures 5 and 7, we notice that the bulk modulus artifact does not dominate the reconstruction as in the case of the density artifact. This result suggests a feature of two-parameter Born inversion which should be recalled when interpreting subsequent reconstructions. Simply stated, the reconstructed density profiles are less reliable than the reconstructed bulk modulus profiles. Hanson (1984) has also documented this result in his implementation of Raz's inversion method. Thus, although we can reduce artifacts of the inversion, we recognize that both parameter reconstructions are influenced by differing levels of inaccuracy.

As pointed out by Hanson, the most accurately inverted profiles are obtained when the density and the bulk modulus vary in a manner which reduces impedance contrasts. This situation occurred in the previous example. As an additional example, we consider a model where although both

parameters vary across the interface, the normal incidence impedance remains constant. The filtered and unfiltered reconstructions of a constant impedance model with 10% parameter changes are shown in Figures 9 and 10, respectively. For this input model, the expected reconstruction should consist of the bulk modulus and density variations moving equal amounts in opposite directions. In Figure 9, we notice that, once again, the density variation dominates the reconstruction. As before, we are able to obtain an interpretable result by preconditioning the offset data prior to inversion (compare Figures 9 and 10). The primary reason for presenting this example is to demonstrate the usefulness of two-parameter inversion techniques. By taking advantage of impedance variations with offset, we are able to separate the components of reflectivity. Methods which utilize coincident source-receiver data can only recover normal incidence impedance changes and would not interpret a parameter change for the model of Figures 9 and 10.

Decreasing Velocity Reconstructions

When the velocity decreases across the interface, there are no post-critical data to exclude from the inversion. This allows us to test the inversion for broadband data. As an initial example, we consider the model of Figure 5 with the velocities interchanged. This situation is equivalent to probing the model of Figure 5 from below. A quick look at the plane-wave reflection coefficient for this model reveals that its magnitude is identical to that of Figure 5. In Figure 11, we present the broadband reconstruction of this model. Clearly, the density artifact is of the same order as the actual bulk modulus variation. Comparing this broadband artifact with its counterpart in Figure 5, we observe that both are of equal

size relative to their respective bulk modulus changes. Since the spatial bandwidths of these models are different, this equivalence might be traced to the equivalence of the reflection coefficients. To test this, we invert the model of Figure 12 for data which correspond to the reflection coefficient of Figure 6. In comparing the relative sizes of the resulting density artifacts, we conclude that they indeed are of equal amplitude. Therefore, the amplitudes of inversion artifacts are determined by the nonlinear nature of the reflection coefficient. By adhering to the criterion suggested by equation (37), we can reduce these deleterious effects.

Constant Velocity Reconstructions

As a final example which illustrates the usefulness of two-parameter inversion techniques, we consider a constant velocity model. For this situation, the reflection coefficient is a constant which does not vary with offset. We therefore gain nothing by filtering the offset data prior to inversion. This example provides the only situation where our approximate inversion agrees with the exact result. That is, since there is no velocity contrast, the Born approximation is exactly satisfied ($\Delta_1 = 0$). As a result, both the Born and exact theories predict that both parameter variations have equal amplitude and polarity. An example of a broadband constant velocity reconstruction is illustrated in Figure 13. Clearly, this two-parameter inversion scheme can accurately predict these subsurface parameter changes.

Least-Squares Reconstructions

As mentioned above, inversion results improve if the input frequencies are chosen close together. There is however no criterion which governs the specific choice of these frequencies. In the previous examples, we chose 60 and 62 Hz, because these values both conform to the seismic bandwidth, and provide reasonable inversion results. To demonstrate that the specific choice of frequencies is arbitrary, we consider a least-squares solution over a range of frequency values. In Figure 14, we present a least-squares reconstruction of the model shown in Figure 6. These results are obtained by inverting equation (18) with the summation extending from 55 to 65 Hz. In comparing Figures 6 and 14, we acknowledge that the reconstructions are similar in character and would lead to equivalent interpretations. Their only difference lies in the frequency content of the reconstructed profiles. The similarity of these results is not alarming. We do not expect the least-squares procedure to improve the inversion of synthetic data since this method is only useful when considering noisy synthetic or field data sets. The above example merely demonstrates that inversion results are not strictly dependent on the choice of input frequencies. As mentioned above, the two frequencies should be chosen close together, and should be large enough to provide a sufficient bandwidth for stable computation.

FIXED FREQUENCY DOUBLE INTERFACE RECONSTRUCTIONS

Introduction

In all wave equation methods which transform surface reflection data into a map of subsurface reflectors, the selection of a background velocity profile determines the accuracy of the results. For Born inverse methods, this reference velocity affects not only the migration of the image, but also the recovery of the amplitude information. These results are demonstrated in a simple example by Weglein and Gray (1983). In this example, they consider the single parameter Born reconstruction of a one-dimensional medium for various constant background velocities. They conclude that constant background Born techniques cannot simultaneously determine both the location and the size of a single parameter change.

As mentioned above, our inversion scheme assumes that the velocity in the first medium is the constant background velocity. Consequently, the locations of both parameter variations are correct for the first reflector while the amplitudes are necessarily incorrect. In addition, these amplitudes are further complicated by the apparent link between the parameter variations. The deficiencies of Born methods do not improve with depth. In fact, both the locations and the amplitudes of the parameter variations for the second reflector will be incorrect. In this chapter, we examine the reconstructions of the double interface synthetic data derived in Chapter 2. When examining these reconstructions, we use the first reconstructed reflector as a measure for the accuracy of the second reconstructed reflector. For interpretational purposes, it is safe to assume that the amplitude of the first change is correct if the data have

been filtered. The following examples will expose the deficiencies inherent in the formulation of our approximate inversion. As before, we will attempt to rectify inversion artifacts by filtering the input data prior to inversion.

Examples of Double Interface Reconstructions

To conform to realistic earth models, we considered 10% parameter changes for the single interface model. By filtering the input data, we were able to obtain interpretable reconstructions. For the double interface model, we begin by considering two consecutive 10% parameter changes. In Figure 15, we present the reconstruction of a constant density model with the layer separating two half-spaces of equal but lower velocity. Clearly, the inversion is unstable for this input model, the density artifact associated with the second interface dominates the reconstruction. To improve this reconstruction, we adhere to the previous strategy and eliminate far offset data prior to inversion (see Figure 16). In comparing Figures 15 and 16, we observe that this procedure does not improve the interpretability of the reconstruction--eliminating low k_z data merely reduces the spatial bandwidth. Furthermore, the artifact identification procedure outlined in Chapter 3 is not effective in delineating the double interface density artifact. We conclude that this procedure is limited to situations where the inverted wave field is accurately modeled above the reflector of interest. We note also that the density artifact incorrectly establishes the location of the second interface. Born theory however would predict a location shallower than 3000 feet rather than deeper. Thus, it appears that this inversion scheme produces unstable results for this model,

and these results are not improved by further filtering the input data.

Since this method is based on a weak scatterer approximation, we expect stable reconstructions for smaller parameter changes. In Figures 17 and 18, we present the reconstructed profiles of the model of Figure 15 with the 10% velocity changes replaced by 1% and 0.1% changes, respectively. In all three models, the maximum offset, the input frequencies, and the reflector depths are equivalent. Turning first to Figure 17, we observe that although the density artifact continues to dominate the reconstruction, the overall results are more stable. Note that the reflection coefficient is trivial for all offsets in this inversion, yet the reconstruction is inaccurate. This result further demonstrates that the low k_z filter has a limited application for the two-interface situation. When the parameter changes are reduced by another order of magnitude (see Figure 18), the reconstruction is interpretable, however, the density artifact located at the second interface still exists. For this model, the reflection coefficient is too small to be distinguished from the k_x -axis. From the preceding examples, we conclude that this inversion method cannot properly interpret two successive real earth parameter changes. As shown, the inversion results are only accurate for a cumulative change of 0.2%.

In the previous chapter, we examined a constant bulk modulus model to illustrate that inversion results improve for parameter changes which minimize impedance contrasts. In Figures 19 through 21, we present the reconstructed profiles of double interface, constant bulk modulus, models. These models are consecutively equivalent to the models of Figures 15, 17, and 18 with only the densities adjusted to simulate constant bulk modulus. For example, the spatial bandwidth, the velocity contrasts, and the reflector locations are equal for the models of Figures 15 and 19, however,

the input density profile of Figure 19 produces a constant bulk modulus. By equating all but the input densities, we insure that the limitations imposed by the Born approximation are identical. This allows a simple comparison between the two models. Similarly, the constant density models of Figures 17 and 18 can be compared with the constant bulk modulus models of Figures 20 and 21, respectively. Thus, in considering these six reconstructions, we can compare results within each constant parameter set or against its counterpart in the other set.

Considering Figure 19 first, we notice that the density change located at the second interface dominates the reconstruction. This change should be of equal amplitude and opposite polarity as the change which delineates the first interface. We therefore consider this reconstruction to be unstable. In fact the character of this reconstruction resembles the unstable constant density reconstruction of Figure 15. The differing density profile only affects the response at the first interface. We conclude that for velocity contrasts of this magnitude, the inversion results are unstable, regardless of the input density profile. It is also important to note that the reconstructed density is responsible for the instability. This result reinforces the previous statement that the reconstructed density is less reliable than the reconstructed bulk modulus.

Next, we examine the constant bulk modulus reconstruction of Figure 20. Although the velocity structure in this model corresponds to the constant density model of Figure 17, this reconstruction is superior. In Figure 17, the density artifact at the second interface dominates the reconstruction. In Figure 20, the density change at the second interface is only slightly incorrect in amplitude and location. Also, the bulk modulus artifact is quite small. Thus, for 1% velocity changes, the input density profile of

Figure 20 reduces the impedance contrasts and improves the inversion. In fact, the accuracy of this reconstruction is comparable to that of Figure 18, even though the velocity contrasts are ten times greater. This further suggests that artificial bulk modulus variations are less damaging than artificial density variations.

Finally, we consider the reconstruction of Figure 21. As expected, this result is almost exact; the bulk modulus artifact is trivial. In comparing all three constant bulk modulus reconstructions with all three constant density reconstructions, we conclude that the former set are more accurate than the latter. This result is attributed both to the reduction of impedance across the interfaces, and the controlling influence of the density variation in all reconstructions. We must admit however that the inversion is unstable for the realistic earth models of Figures 15 and 19.

Returning to the constant density model of Figure 15, we consider two equivalent models but for the depth of the second interface. In Figure 22, we present the reconstruction of this model with a shallower second reflector. The model of Figure 23 is characterized by a deeper second reflector. In comparing these three reconstructions, we conclude the error associated with the approximate reconstruction of the first interface increases with depth. Therefore, not only is this fixed frequency procedure unstable for two realistic parameter changes, but also the accuracy of all reconstructions depends on the depth of the second reflector. Instead of speculating as to the origin of these deficiencies, we take advantage of the exact form of the model data to analyze inversion artifacts. Before we do this, we reformulate the inversion to both improve stability and simplify analysis.

FIXED ANGLE INVERSION

Introduction

In the previous inversion scheme, temporal frequency is chosen as the free variable when solving for the parameter variations. In that formulation, the necessary suite of k_z values is generated by sweeping through a range of incident angles for each fixed wave vector. A prohibitive consequence of this procedure is that the elimination of the detrimental far offsets severely reduces the spatial bandwidth. As a result, the inversion becomes unstable. To overcome this instability, we reformulate the inversion in terms of fixed incident angles. Instead of choosing two fixed frequencies, we now choose two fixed incident angles when solving for the parameter variations. The k_z values are computed by establishing a temporal frequency bandwidth for the fixed angle wave vector. As we will see, this formulation achieves greater stability as the offset information and the spatial bandwidth are no longer linked. In this new formulation, we can choose incident angles which correspond to Born-compatible reflection coefficients with no restriction on spatial bandwidth. This procedure is not unique. In his time domain formulation, Raz (1981) utilizes two distinct offsets when recovering both velocity and density. Therefore, in this chapter, we reformulate the inversion to improve the stability of the output. To demonstrate this improvement, we re-invert the models, previously considered in the fixed frequency formulation. As an additional feature, this reformulation simplifies the computation of the inverted profiles.

Reformulation of the Inversion

In this section, we rewrite the forward equation in terms of the incident angle θ . This is achieved by substituting the definition

$$k_z = \frac{\omega}{c_r} \cos \theta \quad (38)$$

in equations (28):

$$\begin{aligned} A_1(\theta) &= \frac{-\pi}{\cos^2 \theta} \\ A_2(\theta) &= -2\pi - A_1(\theta) \end{aligned} \quad (39)$$

where

$$\tilde{D}_s(k_z, \theta) = A_1(\theta) \mathfrak{H}_1(-2k_z) + A_2(\theta) \mathfrak{H}_2(-2k_z) \quad (40)$$

To invert equation (40) for the transformed medium variations, we compute A_1 , A_2 , and \tilde{D}_s for two values of θ and solve for \tilde{a}_1 and \tilde{a}_2 :

$$\tilde{a}_1'(-2k_z) = \mathfrak{H}_2'(-2k_z) + \frac{1}{\pi} \left[\frac{\tilde{D}_s(k_z, \theta_1) - \tilde{D}_s(k_z, \theta_2)}{\sec^2 \theta_1 - \sec^2 \theta_2} \right] \quad (41a)$$

$$\mathfrak{H}_1'(-2k_z) = \frac{1}{2\pi} \left[\frac{\sec^2 \theta_1 \tilde{D}_s(k_z, \theta_1) - \sec^2 \theta_2 \tilde{D}_s(k_z, \theta_2)}{\sec^2 \theta_1 - \sec^2 \theta_2} \right] \quad (41b)$$

Clearly, this inversion procedure is computationally simpler than the previous method since equations (39) are independent of k_z . For a specific θ , A_1 and A_2 are numbers which weight each spatial component of the data equally. This result not only simplifies the computation, but also it reduces the complexity of future mathematical analysis. Once again, we note the near singular behavior of the denominator of equations (41) for θ_1 close to θ_2 . As before, we have only to inverse Fourier transform equations (41) to express the parameter variations as a function of depth.

To compute the synthetic data for this method, we generate the k_z values by fixing the incident angle and sweeping through a specified range of temporal frequencies. For this fixed angle formulation, we re-express the single interface data of equation (21) as

$$\tilde{D}_s(k_z, \theta) = \left[\frac{\frac{\rho_2}{\rho_1} - \sqrt{1 + \frac{c_r^2 \Delta_1}{\cos^2 \theta}}}{\frac{\rho_2}{\rho_1} + \sqrt{1 + \frac{c_r^2 \Delta_1}{\cos^2 \theta}}} \right] \exp(-2ik_z h) \quad (42)$$

and the double interface data of equation (22) as

$$\tilde{D}_s(k_z, \theta) = \left[\frac{R_1(\theta) + R_2(\theta) \exp(-2\nu_2 h_2)}{1 + R_1(\theta) R_2(\theta) \exp(-2\nu_2 h_2)} \right] \exp(-2\nu_1 h_1) \quad (43)$$

where R_1 and R_2 are the Rayleigh reflection coefficients at the first and second interfaces respectively, and

$$\nu_1 = ik_z \sqrt{1 + \frac{c_r^2 \Delta}{\cos^2 \theta}}, \quad \nu_2 = ik_z \sqrt{1 + \frac{c_r^2 \Delta_1}{\cos^2 \theta}}, \quad \nu_3 = ik_z \sqrt{1 + \frac{c_r^2 \Delta_2}{\cos^2 \theta}}. \quad (44)$$

From these expressions, we observe that the Rayleigh reflection coefficients are also independent of k_z .

Examples of Fixed Angle Reconstructions

In this section, we examine fixed angle reconstructions of single and double interface models presented in Chapters 4 and 5. To compare the two inversion procedures, we equate both the input model parameters and the spatial bandwidths before inverting. In all of these examples, we examine the reconstruction of a constant density profile, this allows us to test the inversion for unfavorable conditions. As an initial example, we consider the fixed angle reconstruction of the single interface model shown in Figure 6 (see Figure 24). Note that we now list the input angles (in degrees) and the temporal bandwidth, instead of the input frequencies and the maximum offset. In comparing Figures 6 and 24, we observe that the bulk modulus variations are strikingly similar while the density artifact is smaller in the fixed angle reconstruction. This improvement results from our ability to confine the wave vector to a region which corresponds to a small reflected wave field. In other words, in the fixed angle implementation, we are able to satisfy equation (37) by choosing incident angles close to zero. Consequently, the reflection coefficient satisfies the Born approximation. This idea can be seen by comparing the plots of the reflection coefficients in Figures 6 and 24. In the fixed angle implementation, the reflection

coefficient maintains the low values determined by the incident angle of 10 degrees, whereas its counterpart in Figure 6 traces out values corresponding to 55 degrees. Clearly, the plot of the reflection coefficient for the fixed angle implementation appears linear (constant). The selection of incident angles in the fixed angle method is arbitrary. We note however that as in the fixed frequency formulation, inversion artifacts diminish if the input parameters (the incident angles in this case) are chosen close to each other. In all subsequent reconstructions, we select the angles of 5 and 10 degrees to comply with the Born approximation. Therefore, the flexibility of the fixed angle procedure provides more accurate results as the spatial bandwidth is no longer linked to the offset information.

As demonstrated in the previous example, the fixed angle implementation improves single interface reconstructions by further discriminating against nonlinear portions of the offset data. We now apply this method to invert double interface models and compare these results with their corresponding fixed frequency reconstructions. As a first example, we invert the constant density model of Figure 15 by the fixed angle method, this result is shown in Figure 25. As before, we are able to compare these reconstructions since both inversion methods are computed for equivalent spatial bandwidths. In comparing Figures 15 and 25, we notice that the density artifact at the second interface dominates both reconstructions. However, the instability inherent in the fixed frequency reconstruction is not present in the fixed angle reconstruction. In the fixed angle reconstruction, the Born-predicted location of the density artifact is correct. Thus, although the fixed angle technique enhances the character of this reconstruction, the results indicate that Born methods cannot successfully reconstruct both acoustic parameters for 10% velocity changes.

To continue this comparison, we consider two other constant density models with 1% and 0.1% velocity changes, respectively. In Figure 26, we present the fixed angle reconstruction of the 1% velocity contrast model of Figure 17. In comparing these two reconstructed profiles, we observe that the fixed angle profile is more accurate than the fixed frequency profile. In the fixed angle reconstruction, the density artifact located at the second reflector is one third the size of its fixed frequency counterpart. Nevertheless, this artifact is still appreciable. To complete this series of comparisons, we consider the fixed angle reconstruction of the 0.1% velocity contrast model shown in Figure 18 (see Figure 27). Although both reconstructed profiles are interpretable in terms of the input model, the results of Figure 27 are superior. As before, the density artifact is smaller for the fixed angle reconstruction. Therefore, even though the aforementioned advantages of the fixed angle method improve the reconstructions, the inversion method is still unreliable for real earth parameter changes.

In the fixed frequency double interface examples of the previous chapter, we presented evidence which suggested that errors associated with the incomplete (Born) reconstruction of the first interface propagate with depth. To verify this statement, we consider fixed angle reconstructions of a constant density input model for various depths of the second reflector. We choose the input model of Figure 26. Note that in the fixed frequency demonstration of this phenomenon, we considered 0.1% velocity contrasts. For the fixed angle example, we consider 1% velocity contrasts across the interfaces. In Figures 28 and 29, we present the reconstructed profiles of the model of Figure 26 with the second reflector located at 2000 and 4000 feet, respectively. In comparing these three figures, we conclude that the

error does in fact increase with depth. This feature of Born inversion is equally damaging for both inversion procedures.

In comparing the fixed angle reconstructions of Figures 26, 28, and 29, we observe that the error affects not only the amplitude but also the location of the parameter changes associated with the second interface. This result follows from the assumption of a constant background velocity. By assuming a constant background velocity, we force the inversion to model all waves as if they are propagating at the reference velocity. In this example, the reference velocity is the velocity in the first medium. Since this velocity is slower than the velocity in the second medium, the reconstructed parameter changes are located above their expected locations. This feature of the inversion is more obvious in the fixed angle example than in the corresponding fixed frequency example because the velocity contrasts are larger. In the next chapter, we consider the origin of inversion artifacts in the context of the preceeding discussion.

In the above examples, we equate spatial bandwidths between inversion procedures to allow a direct comparison of the amplitudes of the reconstructed profiles. This apparent limitation is in opposition to the flexibility of the fixed angle approach. In the fixed angle approach, we may choose any spatial bandwidth for any incident angle. As a result, we are free to select input data in accordance with the assumptions implicit in the linear inversion. Unlike the fixed frequency method, the stability of the results are not compromised by the bandwidth restrictions effected by the Born approximation.

INVERSION ARTIFACTS REVISITED

Introduction

In Chapter 3, we examined the analytic form of the artificial parameter variations associated with the Born reconstruction of the first interface. We showed that these artifacts could be reduced by emphasizing certain portions of the offset data in the inversion process. In fact, these single interface artifacts can practically be eliminated through the flexibility of the fixed angle implementation. In addition to these false parameter variations, Born theory inaccurately predicts the size of the actual parameter change at the first interface, even if the velocity in the first medium is selected as the reference velocity. Fortunately, this amplitude error is trivial. When considering the double interface reconstructions, we demonstrated that the errors associated with the incomplete reconstruction of the first interface increase with depth. Thus, even though these errors are not severe at the first interface, they are significant at the second interface. In this chapter, we examine the analytic expressions of the artifacts which characterize the reconstructed changes at the second interface. This analysis both verifies previous conclusions and provides insight into a possible correction of errors implicit in two-parameter, constant background, Born inversion.

Analysis of Double Interface Artifacts

As in the single interface analysis, we substitute constant parameter model data into the corresponding inversion relation to obtain an expression

for the artifact. Specifically, we will again consider the density artifact produced by a bulk modulus change. For this double interface analysis, we exploit the simplicity offered by the fixed angle implementation. Since the multiple reflections do not interfere with the primary reflections, we utilize the fixed angle expression of the model data given by equation (27)

$$\tilde{D}_s(k_z, \theta) = R_1(\theta) \exp(-2\nu_1 h_1) + R_2(\theta) T(\theta) \exp[-2(\nu_1 h_1 + \nu_2 h_2)] \quad (45)$$

where ν_1 and ν_2 are computed according to equations (44) and T represents the transmission loss through the layer. In this expression, each term represents the primary reflection event for each interface. Substituting equation (45) with a constant density profile and an arbitrary reference velocity into equation (41b), we obtain an expression for the density artifact:

$$\begin{aligned} \tilde{D}'_s(-2k_z) = & \frac{1}{2\pi(\sec^2 \theta_1 - \sec^2 \theta_2)} \\ & \cdot \left[\sec^2 \theta_2 B_1(\theta_1) \exp[-2ik_z (1 + c_r^2 \Delta / \cos^2 \theta_1)^{1/2} h_1] \right. \\ & - \sec^2 \theta_1 B_1(\theta_2) \exp[-2ik_z (1 + c_r^2 \Delta / \cos^2 \theta_2)^{1/2} h_1] \\ & + \sec^2 \theta_2 B_2(\theta_1) T(\theta_1) \exp\{-2ik_z [h_1 + (1 + c_r^2 \Delta / \cos^2 \theta_1)^{1/2} h_2]\} \\ & \left. - \sec^2 \theta_1 B_2(\theta_2) T(\theta_2) \exp\{-2ik_z [h_1 + (1 + c_r^2 \Delta / \cos^2 \theta_2)^{1/2} h_2]\} \right] \quad (46) \end{aligned}$$

where $B_1(\theta)$ and $B_2(\theta)$ are defined as the constant density Rayleigh reflection coefficients at the first and second interfaces, respectively. If the reference velocity is the velocity in the first medium, then $\Delta = 0$, and the density artifact is given by

$$\begin{aligned}
\mathbb{K}'_2(-2k_z) = & \frac{1}{2\pi(\sec^2\theta_1 - \sec^2\theta_2)} \\
& \cdot \left[[\sec^2\theta_1 B_1(\theta_1) - \sec^2\theta_2 B_1(\theta_2)] \exp(-2ik_z h_1) \right. \\
& + \sec^2\theta_2 B_2(\theta_1) T(\theta_1) \exp\{-2ik_z [h_1 + (1 + c_1^2 \Delta_1 / \cos^2\theta_1)^{1/2} h_2]\} \\
& \left. - \sec^2\theta_1 B_2(\theta_2) T(\theta_2) \exp\{-2ik_z [h_1 + (1 + c_1^2 \Delta_1 / \cos^2\theta_2)^{1/2} h_2]\} \right] . \quad (47)
\end{aligned}$$

The expression given by equation (47) corresponds to the spatial Fourier transform of the density artifacts plotted in Figures 25 through 32. To understand the nature of these artifacts, we will analyze this expression in the context of Born theory. Considering the first term in this equation, we observe that this expression is the fixed angle analog of equation (35). This term represents the artificial density variation produced by the incomplete reconstruction of the bulk modulus at the first interface. Reviewing the density artifacts plotted in the aforementioned figures, we see that this term is insignificant. The density artifact located at the first interface does not compromise the overall accuracy of the reconstruction since the input angles comply with the Born approximation. In contrast, the second and third terms of equation (47) combine to form the deleterious density artifact associated with the second interface.

Before examining the analytic expression for the second interface density artifact, we recall some assumptions implicit in the linear inversion. The primary assumption of Born inversion is that individual scattering interactions do not significantly affect the incident wave field. Thus, the total wave field is approximated by the reference wave field, and

the inversion models all wave motion as the wave field propagating in the reference medium. Consequently, for our problem, the wave field propagating in the second medium is phase shifted with respect to the wave field propagating in the first or reference medium. This phase shift is not accounted for by the inversion and contributes to inversion errors. In our analysis of single interface artifacts, we demonstrated that the weak scatterer assumption is satisfied if we select offset data which minimize the energy of the reflected wave field. As shown above, this requirement is not sufficient for the accurate reconstruction of the second reflector. To better understand inversion errors, we must consider the effect of the phase shift encountered by the incident field at the first interface.

Returning to equation (47), we observe that the sum of the second and third terms of this expression form the density artifact which delineates the second interface. In general, these two terms represent two delta functions whose amplitudes are similar in magnitude, yet opposite in sign. Furthermore, these delta functions are characterized by different phase shifts which affect their respective locations in the spatial domain. In fact, these two phase shifts are the manifestation of the phase shifting of the incident field in the second medium. That is, if Δ_1 were zero, then the wave field in the second medium would be in phase with the reference wave field, and the phase shifts which characterize these two delta functions would vanish. As a result, the second interface artifact would be represented by a single delta function whose amplitude would be of the same order as that of the single interface artifact. Therefore, as the velocity contrast at the first interface decreases in accordance with the Born approximation, the phase shifts inherent in equation (47) diminish, and the second interface artifact decreases. Upon further inspection, we conclude

that the relative amplitude and phase differences between these two delta functions are dependent on the input angles. For example, as θ_1 approaches θ_2 , both the phases and the moduli of these two terms become equal, and the two expressions cancel. Likewise, as the values of θ_1 and θ_2 diverge, the two delta functions become more dissimilar in amplitude and phase, and the artifact increases. Thus, as in the single interface situation, the artifact associated with the second interface diminishes as θ_1 approaches θ_2 . This second interface artifact however is affected in both amplitude and phase. Simply stated, it is the phase shifts implicit in these expressions which are responsible for the deleterious nature of the second interface artifacts.

In the previous discussion, we observed that since the incident field is phase shifted at the first interface, the reconstructed second interface is characterized by a sum of two phase shifted delta functions. These phase shifts are represented by

$$\left[1 + \frac{c_1^2 \Delta_1}{\cos^2 \theta_1} \right]^{1/2} \quad (48)$$

where c_1 is the velocity in the first medium, θ_1 is the incident angle, and Δ_1 is the velocity contrast at the first interface. As mentioned above, both the difference between these phase shifts as well as their magnitudes influence the quality of the reconstruction. For instance, if the second term of equation (48) vanishes, then the field in the second medium is in phase with the incident field, and inversion results are improved. Thus, to rectify inversion errors, we should minimize the size of this term in the phase shifts. This is accomplished by considering models which are

characterized by both a small velocity contrast at the first interface, and near normal wave vectors. Considering briefly the constant density models of Figures 25 through 27, we conclude that indeed both criteria are necessary--only the model of Figure 27 where 0.1% velocity contrasts are inverted leads to an insignificant density artifact at the second interface. Therefore, by adhering to the weak scatterer assumption, we minimize the phase shift of the incident wave field which enables an accurate reconstruction of the second reflector.

In examining equation (48), we note that only the strength of the first velocity contrast affects the magnitudes of the phase shifts implicit in the second interface density artifact. Consequently, a large velocity contrast at the first interface limits the accuracy of subsequently reconstructed parameter changes. To demonstrate this result, we consider two models which consist of both a 0.1% and a 10% velocity change. In these two models, the order of the velocity changes are reversed so as to reveal the influence of Δ_1 on the reconstructions (see Figures 30 and 31). Turning to Figure 30 first, we note that the 0.1% velocity change at the first interface does not seriously impair the reconstruction of the 10% velocity change at the second interface. This is the expected result as Δ_1 is trivial in this case. Comparing the reconstructions of the 10% velocity changes for both models, we observe that the corresponding density artifact is larger in Figure 30 than in Figure 31. We also note that the actual bulk modulus change in Figure 30 is slightly antisymmetric. (This asymmetry verifies that the actual parameter change is also a sum of two band-limited delta functions.) Based on the previous discussion, we conclude that these features are accumulative manifestations of the slight phase shift incurred at the first interface. When comparing the reconstructions of Figures 30 and 31

directly, we notice that they are not simple mirror images of each other. Since Δ_1 is appreciable for the model of Figure 31, the reconstructed parameter changes associated with the second interface are noticeably incorrect in both size and location. Thus, although the sizes of the reconstructed parameter changes at the second interface are weighted by the corresponding reflection coefficient, the overall character of these variations is determined by the phase shifts given in equation (48).

When considering the general features of double interface reconstructions, we observed that errors associated with the Born reconstruction of the first interface increase with depth. These errors affect both the sizes and the locations of the reconstructed parameter changes delineating the second interface. By examining the expression for the density artifact given by equation (47), we can understand the depth dependent nature of the error. In the second and third terms of equation (47), we notice that each corresponding phase shift is weighted by the depth of the second reflector. Thus as h_2 increases, the magnitudes of these phase shifts also increase. This result may also be understood in the context of Born theory. In Born inverse methods, the scattered wave field is estimated by the second term in the Born series. As a result, the suitability of this estimation depends upon the convergence of the higher order terms. If this series converges slowly, then the first Born approximation inadequately describes the scattered wave field. In any case, since the higher order terms in the Born series are integral expressions, the error associated with their convergence increases as the limits of integration increase. That is, errors implicit in the linear inversion accumulate as we integrate the wave field over greater and greater depths. In conclusion, we maintain that the predicted sizes and locations of the

second parameter changes are determined by both the phase shifting of the incident wave and the depth of the second interface.

Inversion Artifacts and the Reference Velocity

In the previous reconstructions, the reference velocity is chosen to be the velocity in the first medium. As a result, the wave field in the second medium is phase shifted with respect to the wave field in the reference medium, and this causes inversion errors to increase with depth. In Born inversion however, we need not choose the reference velocity to be the velocity in the first medium. The specific choice of a reference velocity depends on the goals of the inversion. In this section, we examine the influence of the reference velocity on inversion artifacts. To do this, we invert a constant density model for different reference velocities and interpret the results in terms of equation (46). As mentioned above, equation (46) represents the double interface density artifact for an arbitrary reference velocity. From this expression, we observe that the reconstruction of each interface is the summation of two phase shifted delta functions. Thus, if the reference velocity is neither c_1 nor c_2 , then each reconstructed interface is characterized by the accumulative errors produced by these phase shifts. As a result, not only are both the sizes and locations of the parameter changes incorrect for each interface, but also the extent of these errors are determined by the depths of the interfaces. As before, we note that the strengths of these phase shifts depend on the angle of incidence, the velocity contrast, and the reference velocity. We also recall that these phase shifts which spatially separate the delta functions only exist if the wave field above the reconstructed interface is

phase shifted with respect to the reference wave field.

In Figure 32, we present the reconstruction of a constant density model with the reference velocity equal to the velocity in the first medium. In this example, the reconstruction of the first interface is essentially correct while the reconstruction of the second interface suffers from accumulative phase errors. Considering the first reconstructed reflector, we observe that the locations of the parameter changes are correct, Born theory however predicts slight errors in the reconstruction of their corresponding amplitudes. For our purposes, we view this reconstruction as the prototype for both interfaces in all subsequent examples. To provide a proper comparison between this reconstruction and other relevant reconstructions, we list the amplitudes of these variations in Table 1 (see page 55).

In Figure 33, we reconstruct the model of Figure 32 with the reference velocity equal to the layer velocity. Consequently, the wave field in the layer is in phase with the reference wave field since $\Delta_1 = 0$. In this example however, the wave field in the first medium is phase shifted with respect to the reference wave field ($\Delta \neq 0$). We conclude that the artifact associated with the first interface is characterized by two phase shifted delta functions while that of the second interface consists of only one delta function. Thus, as the wave field propagates out of phase to the first reflector, the error inherent in the Born reconstruction of this reflector grows in size. From Figure 33, we observe that this accumulative error affects both the sizes and the locations of the parameter changes. Comparing the parameter amplitudes of this reconstruction with their counterparts in Figure 32 (see Table 1), we conclude that both parameter changes have

increased in size. In fact, there is now a noticeable density artifact located at the first interface. Considering the second reflector, we observe that the error in this reconstruction is similar to that of the first interface (see Table 1).

FIGURE	$K_1 \text{ max}$	$\rho_1 \text{ max}$	$K_2 \text{ max}$	$\rho_2 \text{ max}$
32	0.093	--	0.140	0.108
33	0.103	0.005	0.103	0.005
35	0.095	0.002	0.095	0.002

Table 1. List of the maximum parameter amplitudes for Figures 32, 33, and 35.

Since the wave field in the layer is in phase with the reference wave field, the errors established at the first interface propagate to the second reflector but do not grow in size. Thus, the location error at the second interface is identical to that at the first interface. There are however slight amplitude errors associated with the incomplete reconstruction of the second reflector. To further illustrate that these inversion errors do not increase within the layer, we consider this model for a deeper second reflector (see Figure 34). In comparing Figures 33 and 34, we conclude that the inversion errors associated with the second interface are identical to those of the first. Therefore, by establishing the reference velocity as the layer velocity, we have distributed the inversion error between both reflectors, and now these errors are sensitive to the depth of the first reflector.

As mentioned above, if the reference velocity is neither c_1 nor c_2 , then both reflectors are reconstructed by a sum of two phase shifted delta functions. As the depths of these reflectors increase, the corresponding

phase discrepancies also increase, and the inversion errors grow in size. These observations follow directly from equation (46). To demonstrate this result, we reconstruct the previous constant density model for a reference velocity midway between c_1 and c_2 ; in Figure 35, we present this example with $c_r = 5025$ ft/sec. Comparing this reconstruction with that of Figure 33, we observe that the inversion errors associated with the first interface have diminished. By reducing the reference velocity, we have reduced phase shifts in the first two terms of equation (46), thereby reducing the accumulative errors. Thus, both the density artifact and the location error decrease at the first interface. From Table 1, we also note that the amplitude of the bulk modulus variation is also reduced. In fact, it is close to its counterpart in Figure 32. Unlike the model of Figure 33, the wave field in the layer of Figure 35 is phase shifted with respect to the reference wave field. As a result, the inversion errors produced at the first interface not only propagate with depth, but also they increase with depth. To demonstrate this feature, we invert the model of Figure 35 for a deeper second reflector (see Figure 36). Clearly, the reconstruction of the second reflector in Figure 36 is characterized by greater inversion errors--the predicted parameter variations are both larger and shallower. In conclusion, we observe that this intermediate reference velocity effectively distributes the inversion error. In fact, this reconstruction is superior to that of Figure 33 as the locations and the amplitudes of both velocity changes are more accurate.

In the above examples, we demonstrate that by adjusting the reference velocity, we may distribute the inversion errors between the reconstruction of each interface. Depending on the goals of the inversion, this procedure

might be advantageous. For example, when comparing Figures 32 and 35, we might conclude that Figure 35 is a more accurate reconstruction of the input model. Even though all amplitudes and locations are incorrect, this reconstruction is not dominated by the error associated with the second reflector. We might however wish to reconstruct the first interface with precision. In that case, the reconstruction of Figure 32 would be superior to that of Figure 35. Therefore, since errors are an inevitable consequence of constant background inversion, we choose a reference velocity so as to minimize the errors, deemed most deleterious to our goals.

CONCLUSIONS

In this thesis, we implement the two-parameter, constant background, Born inversion method of Clayton and Stolt (1981) for acoustic synthetic data which represent single and double interface models. Since these data are exact, we are able to compare reconstructed acoustic profiles with their analytic expressions. We direct this analysis toward understanding the error implicit in the approximate inversion. As a result, we devise an implementation which provides more reliable interpretations of Born reconstructions.

From our analysis, we observe that inversion errors are minimized if the offset data is preconditioned in accordance with the Born approximation. Specifically, we reduce the energy of the reflected wave field by eliminating the offset data which are characterized by large angles of incidence. These deleterious data however provide the greatest variation in the reflection coefficient. As pointed out by Clayton and Stolt (1981), it is the angular dependence of the reflection coefficient which allows the separation of the components of reflectivity. Therefore, inherent in our method is a contradiction of objectives: the linear inversion requires the elimination of data which enhance the recovery of both acoustic parameters.

By selecting a fixed angle implementation, we are able to separate bandwidth considerations from data preconditioning requirements. Consequently, the flexibility afforded by this implementation leads to stable results. In fact, for single interface models, the reconstructed profiles are almost exact. For double interface models however, the reconstructions suffer from sizeable Born-related artifacts. To understand the nature of these artifacts, we examine their analytic expressions. Since

the reconstructed density variation is less reliable than its corresponding bulk modulus variation, we focus our analysis on double interface density artifacts. As a result, we test the inversion for the input models which provide the least favorable results.

In our analysis of double interface density artifacts, we observe that the reference velocity influences the interpretability of the reconstructions. In general, the reference velocity affects the phase shifts inherent in the modeled wave field. As evidenced by our examples, this phase shifting causes inversion artifacts to increase with depth--these accumulative phase errors seriously can compromise the usefulness of this inversion technique. We therefore select a reference velocity which reduces the errors, considered most harmful to our inversion objective.

This investigation establishes that this two-parameter, constant background, linear inversion cannot accurately reconstruct two consecutive, real earth, parameter changes, even under idealized conditions. The data requirements preclude the applicability of the Born approximation for recovering the acoustic parameter changes, typical of geophysical problems. Thus, this inversion accurately reconstructs only weak scattering interactions. To improve the usefulness of this technique, we could implement the inversion for a variable reference velocity. If accurate migration velocities are obtained, this approach will reduce the relative sizes of parameter changes, and hence validate the weak scatterer assumption. As a result, accumulative phase errors will be reduced.

Applying the refinement algorithm developed by Hagin and Cohen (1984) to this two-parameter procedure would reduce the accumulative errors, implicit in the linear inversion. According to this refinement algorithm, Born-related errors are recursively eliminated from constant background

reconstructions. Consequently, this procedure provides an improved estimate of subsurface parameter variations. This method however requires an accurate estimate of real earth parameter changes from measurements of their reconstructed counterparts. To insure accurate estimates, a method for separating artifacts from true parameter variations would have to be developed. Perhaps however, the single interface artifact identification procedure presented by Weglein, Violette, and Keho (1985) could be used to test each successive reflector for inversion artifacts. Since the aforementioned refinement scheme would eliminate accumulative errors, this identification procedure could be applied with confidence at each interface. We note that this method would be most useful for noisy synthetic or field data sets. Implementing the refinement procedure in conjunction with this artifact identification method would be computationally more efficient than implementing a variable background inversion. Furthermore, these methods require only an accurate estimate of the velocity in the first medium, whereas variable background inversion requires an accurate estimate of all migration velocities. Therefore, this postprocessing refinement algorithm might improve two-parameter reconstructions by efficiently reducing the effects of accumulative errors.

ACKNOWLEDGMENTS

Initially, I thank Sohio Petroleum Company for both supporting and releasing a portion of this research effort. Special thanks go to Art Weglein of Sohio and colleague Tim Keho of the Earth Resources Laboratory at the Massachusetts Institute of Technology. Much of this work derives from their research experience. I also thank Golden Geophysical Corporation for providing me with the computing facilities necessary for this work.

I also gratefully acknowledge the support of The Office of Naval Research, Mathematics Division, through its Selected Research Opportunity Program, and the Consortium Project on Seismic Inverse Methods For Complex Structures at the Center for Wave Phenomena, Colorado School of Mines. Consortium members are Amoco Production Company, Conoco, Inc., Digicon, Inc., Geophysical Exploration Company of Norway A/S, Golden Geophysical Corp., Marathon Oil Company, Mobil Research and Development Corp., Phillips Petroleum Company, Sun Exploration and Research, Texaco USA, Union Oil Company of California, and Western Geophysical.

Finally, I thank my advisor, Norm Bleistein, of the Center for Wave Phenomena for offering both his time and his timely insights. Norm's criticisms enhanced my knowledge of both inversion theory and word processing.

REFERENCES

- Berkhout, A. J., 1982, **Seismic Migration-Imaging of Acoustical Energy by Wave Field Extrapolation. Theoretical Aspects**: Elsevier Scientific Publishing Company, New York.
- Bleistein, N., 1984, **Mathematical Methods for Wave Phenomena**: Academic Press, New York.
- Bleistein, N., and Cohen, J. K., 1982, Velocity inversion--Present status, new directions: **Geophysics**, v. 47, p. 1497-1511.
- Clayton, R. W., and Stolt, R. H., 1981, A Born-WKB inversion method for acoustic reflection data: **Geophysics**, v. 46, p. 1559-1567.
- Cohen, J. K., and Bleistein, N., 1979, Velocity inversion procedure for for acoustic waves: **Geophysics**, v. 44, p. 1077-1087.
- Ewing, W. M., Jardetzky, W. S., and Press, F., 1957, **Elastic Waves in Layered Media**: McGraw Hill Book Co., New York.
- Frisk, G. V., 1979, Inhomogeneous waves and the plane-wave reflection coefficient: **J. Acoust. Soc. Am.**, 66, p. 219-234.
- Hagin, F. G., and Cohen, J.K., 1984, Refinements to the linear velocity inversion theory: **Geophysics**, v. 49, p. 112-118.
- Hanson, D. W., 1984, **Multi-parameter seismic inversion using the Born approximation**: PhD Thesis, Department of Physics and Astronomy, University of Wyoming.
- Mager, R. D., and Bleistein, N., 1978, An examination of the limited aperture problem of physical optics inverse scattering: **IEEE Trans. Ant. Prop.**, v. AP-25, p. 695-699.
- Morgan, T.R., 1983, **Foundations of Wave Theory for Seismic Exploration**: IHRDC, Boston.
- Raz, S., 1981, Direct reconstruction of velocity and density profiles from scattered field data: **Geophysics**, v. 46, p. 832-836.
- Robinson, E. A., 1983, **Migration of geophysical data**: IHRDC, Boston.
- Weglein, A. B., and Gray, S. H., The sensitivity of Born inversion to the choice of reference velocity: A simple example: **Geophysics**, v. 48, p. 36-38.
- Weglein, A. B., Violette, P. B., Keho, T. H., 1985, Using a constant background multi-parameter Born theory to obtain exact inversion goals: to appear in **Geophysics**.

APPENDIX A: TRANSFORMED GREEN'S FUNCTIONS

In this Appendix, we present the Fourier transforms of the analytic expressions for the Green's functions in equation (10). These Green's functions are the resolvent for the constant background, two-dimensional wave operator. If ρ_r and K_r are assumed constant, L_r becomes

$$L_r = \frac{1}{\rho_r} \left[\nabla^2 + \frac{\omega^2}{c_r^2} \right] . \quad (A-1)$$

The Green's function representing wave propagation from the scatterer location to the geophone location solves

$$\left[\nabla^2 + \frac{\omega^2}{c_r^2} \right] G_r = -\rho_r \delta(x_g - x') \delta(z') . \quad (A-2)$$

Introducing the spatial Fourier transform over the receiver coordinates as

$$\tilde{G}_r(k_{xg}, 0 | x', z', \omega) = \frac{1}{\sqrt{2\pi}} \int_{-\infty}^{\infty} dx_g G_r(x_g, 0 | x', z', \omega) \exp(-ik_{xg} x_g) , \quad (A-3)$$

we apply this transform to equation (A-2) to obtain the following ordinary differential equation for the function \tilde{G}_r :

$$\left[\frac{d^2}{dz^2} + k_{zg}^2 \right] \tilde{G}_r(k_{xg}, 0 | x', z', \omega) = \frac{-\rho_r}{\sqrt{2\pi}} \exp(-ik_{xg} x') \delta(z') \quad (A-4)$$

$$\text{where } k_{zg} = \sqrt{\frac{\omega^2}{c_r^2} - k_{xg}^2}.$$

Two linearly independent solutions to the homogeneous form of (A-4) are given by

$$\tilde{G}_r^\pm = \frac{A^\pm \rho_r}{\sqrt{2\pi}} \exp(\pm ik_{zg} |z - z'|) \exp(-ik_{xg} x_g) \quad (A-5)$$

where \tilde{G}_r^+ represents the outgoing solution and \tilde{G}_r^- represents the incoming solution. For our purposes, we are interested only in the outgoing solution and have only to determine the quantity A^+ .

We determine A^+ by imposing two conditions at the scatterer depth which characterize the nature of the scatterer. These conditions are: (1) that the function be continuous, and (2) that its first derivative have a jump equal to the source term over an interval containing z' . These conditions yield:

$$A^+ = \frac{i}{2k_{zg}}, \quad (A-6)$$

and, at the receiver location, the Green's function is given by

$$\tilde{G}_r^+(k_{xg}, 0 | x', z', \omega) = \frac{i\rho_r}{\sqrt{2\pi}} \exp[-i(k_{xg}x' - k_{zg}|z'|)]/2k_{zg} \quad (A-7)$$

We now perform a similar analysis to determine the transformed Green's function which characterizes propagation from the source location to the scatterer location. The only difference between this derivation and the previous one is that the Fourier transform over the source coordinates has the opposite sense as equation (A-3). This difference results in a sign change on the argument of the exponential:

$$\tilde{G}_r^+(x', z' | k_{xs}, 0, \omega) = \frac{i\rho_r}{\sqrt{2\pi}} \exp[-i(k_{xs}x' + k_{zs}|z'|)]/2k_{zs} \quad (A-8)$$

$$\text{where } k_{zs} = \sqrt{\frac{\omega^2}{c_r^2} - k_{xs}^2} \quad .$$

We now make the observation that the parameter variations are zero for z less than zero. This result allows us to drop the absolute value signs in equations (A-7) and (A-8) before substitution into equation (10)

APPENDIX B: ONE-DIMENSIONAL FORWARD EQUATION

In this Appendix, we derive the one-dimensional forward equation from the two-dimensional forward equation. This is accomplished by assuming that the probed medium is independent of both transverse directions. As a result, the observed offset data is only a function of $x_g - x_s$. Explicitly writing the spatial Fourier transform of the left hand side of equation (13)

$$\tilde{D}(k_{xg}, k_{xs}, \omega) = \frac{1}{2\pi} \int_{-\infty}^{\infty} dx_g \int_{-\infty}^{\infty} dx_s D(x_g - x_s, \omega) \exp[-i(k_{xg} x_g - k_{xs} x_s)], \quad (B-1)$$

we express this result in terms of midpoint, half-offset coordinates:

$$x_h = (x_g - x_s)/2, \quad x_m = (x_g + x_s)/2 \quad (B-2)$$

to obtain

$$\begin{aligned} D(k_{xg}, k_{xs}, \omega) &= \frac{1}{2\pi} \int_{-\infty}^{\infty} dx_m \int_{-\infty}^{\infty} 2dx_h D(2x_h, \omega) \\ &\quad \cdot \exp[-ik_{xg}(x_h + x_m)] \exp[ik_{xs}(x_m - x_h)] \end{aligned} \quad (B-3)$$

where $dx_g dx_s = 2dx_h dx_m$.

Rewriting equation (B-3)

$$\begin{aligned} \tilde{D}(k_{xg}, k_{xs}, \omega) = \frac{1}{2\pi} \int_{-\infty}^{\infty} 2dx_h D(2x_h, \omega) \exp[-i(k_{xg} + k_{xs})x_h] \\ \cdot \int_{-\infty}^{\infty} dx_m \exp[-i(k_{xg} - k_{xs})x_m] \quad , \end{aligned} \quad (B-4)$$

we recognize both integrals as Fourier transforms:

$$\tilde{D}(k_{xg}, k_{xs}, \omega) = \delta(k_{xg} - k_{xs}) \tilde{D}[(k_{xg} - k_{xs})/2, \omega] \quad . \quad (B-5)$$

Turning to the right hand side of equation (13), we write the transformed model variations as Fourier transforms

$$\begin{aligned} \tilde{a}_i(k_{xg} - k_{xs}, -k_{zg} - k_{zs}) = \frac{1}{2\pi} \int_{-\infty}^{\infty} dx \int_{-\infty}^{\infty} dz a_i(x, z) \\ \cdot \exp[-i(k_{xg} - k_{xs})x] \exp[i(k_{zs} + k_{zg})z] \quad (B-6) \end{aligned}$$

where a_i represents both parameter variations. For a_i independent of x , this result becomes

$$\tilde{u}_i(k_{xg} - k_{xs}, -k_{zg} - k_{zs}) = \delta(k_{xg} - k_{xs}) \tilde{u}_i(-k_{zg} - k_{zs}) \quad . \quad (B-7)$$

Thus, for a one-dimensional medium, the linear equations are:

$$\begin{aligned} \delta(k_{xg} - k_{xs}) \tilde{D}[(k_{xg} + k_{xs})/2, \omega] = \\ \frac{-\rho_r}{4k_{zs}k_{zg}} \left[k_r^2 \delta(k_{xg} - k_{xs}) \tilde{u}_1(-k_{zg} - k_{zs}) \right. \\ \left. + (k_{zg}k_{zs} - k_{xg}k_{xs}) \delta(k_{xg} - k_{xs}) \tilde{u}_2(-k_{zg} - k_{zs}) \right] S(\omega). \quad (B-8) \end{aligned}$$

Integrating both sides of equation (B-8) with respect to k_{xs} , and observing that $k_{xg} = k_{xs}$ and $k_{zg} = k_{zs}$, we find

$$\tilde{D}(k_x, \omega) = \frac{-\rho_r}{4k_z^2} \left[k_r^2 \tilde{u}_1(-2k_z) + (k_z^2 - k_x^2) \tilde{u}_2(-2k_z) \right] S(\omega) \quad . \quad (B-9)$$

By the dispersion relation, the right hand side of (B-9) is expressed only as a function of k_z , yielding equation (14).

APPENDIX C: LEAST-SQUARES SOLUTION OVER TEMPORAL FREQUENCY

The forward equation expressed by equation (15) can be solved for the medium parameters by applying least-squares principles. In general, the least squares criterion maintains that we minimize the square of the difference between the desired and the actual expressions. In our case, the desired earth response is the data itself. The actual response however is the right hand side of equation (15). Thus, the least squares error is:

$$E = \sum_j \left[D_j - A_{1j} \tilde{u}_1 - A_{2j} \tilde{u}_2 \right]^2 \quad (C-1)$$

where the summation is taken over a specified range of frequency values. This error is minimized by setting its partial derivatives with respect to each parameter equal to zero:

$$\begin{aligned} \frac{\partial E}{\partial \tilde{u}_1} &= 2 \sum_j \left[D_j - A_{1j} \tilde{u}_1 - A_{2j} \tilde{u}_2 \right] A_{1j} = 0 \\ \frac{\partial E}{\partial \tilde{u}_2} &= 2 \sum_j \left[D_j - A_{1j} \tilde{u}_1 - A_{2j} \tilde{u}_2 \right] A_{2j} = 0 \end{aligned} \quad (C-2)$$

The resulting system of equation is known as the normal equations given by equations (18). The solution of the normal equations yields the least-squares determination of the medium parameters.

APPENDIX D: SINGLE INTERFACE LINE SOURCE ACOUSTIC DATA

In this Appendix, we reduce the point source expression for wave propagation in two semi-infinite media to the line source result. On page 96 of Ewing, Jardetzky, and Press (1957), the scattered wave field in the first medium is given by

$$D_s(r, \omega) = \int_0^{\infty} dk \frac{\delta \nu_1 - \nu_2}{\delta \nu_1 + \nu_2} (\exp[-\nu_1(z+h)] J_0(kr) k) / \nu_1 \quad (D-1)$$

where $\delta = \rho_1/\rho_2$, and h is the distance of the source above the interface. In this expression, r and z represent cylindrical coordinates and thus:

$$\nu_1 = i \sqrt{\frac{\omega^2}{c_1^2} - k^2}, \quad \nu_2 = i \sqrt{\frac{\omega^2}{c_2^2} - k^2} \quad (D-2)$$

where $k = \sqrt{k_x^2 + k_y^2}$.

For layered media, the above point source result has circular symmetry, and we recognize equation (D-1) as the Fourier-Bessel transform. Rewriting equation (D-1) as a Fourier transform in

rectangular coordinates, the field at $z = h$ becomes

$$D_s(x, y, \omega) = \int_{-\infty}^{\infty} dk_x \int_{-\infty}^{\infty} dk_y \frac{\delta \nu_1 - \nu_2}{\delta \nu_1 + \nu_2} \cdot [\exp(-2\nu_1 h)] / \nu_1 \cdot \exp[-i(k_x x + k_y y)] \quad (D-3)$$

Since the probed medium is assumed independent of the y -direction, we may integrate over this direction to obtain the line source result

$$D_s(x, \omega) = 2\pi \int_{-\infty}^{\infty} dk_x \frac{\delta \nu_1 - \nu_2}{\delta \nu_1 + \nu_2} [\exp(-2\nu_1 h) / \nu_1] \exp(-ik_x x) \quad (D-4)$$

where now

$$\nu_1 = i \sqrt{\frac{\omega^2}{c_1^2} - k_x^2}, \quad \nu_2 = i \sqrt{\frac{\omega^2}{c_2^2} - k_x^2} \quad (D-5)$$

Fourier transforming equation (D-4), we find

$$\tilde{D}_s(k_x, \omega) = \frac{\delta \nu_1 - \nu_2}{\delta \nu_1 + \nu_2} [\exp(-2\nu_1 h) / \nu_1] \quad (D-6)$$

For interpretational purposes, Cohen and Bleistein (1982) suggest that it is more desirable to process data for the normal derivative of the variation rather than the variation itself. For our purposes, this derivative is achieved by multiplying equation (D-6) by μ_1 which leaves equation (19).

APPENDIX E: DERIVATION OF THE DOUBLE INTERFACE FORWARD MODEL

The purpose of this Appendix is to derive the expression for the scattered wavefield generated by the two-interface acoustic model. The specifics of this model are illustrated in Figure 3. The method of determination is to solve the system of equations which satisfy the boundary conditions at each interface for the displacement potential representing the upgoing wave field in the first medium. The details of the procedure are similar to examples presented by Ewing, Jardetzky, and Press (1957).

Omitting the time factor, we can express the potential in the first medium as

$$\phi_1 = \int_0^{\infty} dk \frac{k}{\nu_1} J_0(kr) \exp(-\nu_1 z) + \int_0^{\infty} dk \frac{Q_1}{\nu_1} J_0(kr) \exp(-\nu_1 z) \quad (E-1)$$

where Q_1 is the quantity to be determined. All other quantities are defined in Chapter 2 as well as in Ewing, Jardetzky, and Press. The first term in equation (E-1) represents the direct wave while the second term corresponds to the upgoing or scattered wave field. The potential in the second medium is

$$\phi_2 = \int_0^{\infty} dk \frac{Q_2}{\nu_2} J_0(kr) \exp(-\nu_2 z) + \int_0^{\infty} dk \frac{Q_2^*}{\nu_2} J_0(kr) \exp(\nu_2 z) . \quad (E-2)$$

These two terms correspond to the summation of the upward and the downward traveling waves which reflect many times within the layer. Finally, the potential in the third medium is given by

$$\phi_1 = \int_0^{\infty} dk \frac{Q_1}{\nu_1} J_0(kr) \exp(\nu_1 z) \quad (E-3)$$

which represents the downgoing wave field in the lower half-space.

The potentials ϕ_1 and ϕ_2 must satisfy the boundary conditions:

$$\rho_1 \phi_1 = \rho_2 \phi_2 \quad , \quad \frac{\partial \phi_1}{\partial z} = \frac{\partial \phi_2}{\partial z} \quad (E-4)$$

at the first interface. These conditions express the notion that both the pressure and the normal displacement are continuous across the interface. Similarly, the potentials in the second and third media must satisfy the boundary conditions:

$$\rho_2 \phi_2 = \rho_3 \phi_3 \quad , \quad \frac{\partial \phi_2}{\partial z} = \frac{\partial \phi_3}{\partial z} \quad (E-5)$$

at the second interface. These conditions lead to a system of four linear equations expressed by

$$AB = C \quad , \quad (F-6)$$

where

$$A = \begin{bmatrix} \exp(\nu_1 h_1)/\nu_1 & -\delta_1 \exp(\nu_2 h_1)/\nu_2 & -\delta_1 \exp(\nu_2 h_1)/\nu_2 & 0 \\ \exp(\nu_1 h_1) & \exp(-\nu_2 h_1) & -\exp(\nu_2 h_1) & 0 \\ 0 & \exp(-\nu_2 H_1)/\nu_2 & \exp(\nu_2 H_1)/\nu_2 & -\delta_2 \exp(\nu_2 H_1)/\nu_2 \\ 0 & -\exp(-\nu_2 h_1) & \exp(\nu_2 h_1) & \exp(-\nu_2 h_1) \end{bmatrix}$$

$h_1 = h_1 + h_2$, and

$$C = \begin{bmatrix} -k/\nu_1 \exp(\nu_1 h_1) \\ k \exp(-\nu_1 h_1) \\ 0 \\ 0 \end{bmatrix}.$$

As before, we are interested in the plane-wave reflection coefficient, and this quantity corresponds directly to Q_1 . Solving for Q_1 , we obtain equation (21). An expression similar to equation (21) is presented by Frisk (1979), in his paper, Frisk discusses many characteristics of the plane-wave reflection coefficient for single and double interface models.

By representing the denominator of equation (21) as an infinite sum, we are able to decompose the forward model into its component reflected events. Thus, equation (21) becomes

$$Q_1^n = \exp(-2\nu_1 h_1) \left[R_1 + R_2 \exp(-2\nu_2 h_2) \right] \sum_{n=0}^{\infty} (-1)^n (R_1 R_2)^n \exp(-2n\nu_2 h_2). \quad (E-7)$$

Carrying out a portion of the summation, and collecting terms, we obtain

$$Q_1 = R_1 \exp(-2\mu_1 h_1) + R_2(1 - R_1^2) \exp[-2(\mu_1 h_1 + \mu_2 h_2)] \\ + R_1 R_2^2(1 - R_1^2) \exp[-2(\mu_1 h_1 + 2\mu_2 h_2)] + \dots \quad (E-8)$$

where: the first term corresponds to the reflection from the first interface, the second term corresponds to the reflection from the second interface, and the third term corresponds to the first multiple reflection from within the layer. By writing the data in this form, we are able to establish a forward model which excludes multiple reflections. Not only does such an expression provide more favorable data for the linear inversion, but also it yields a less complicated analytic expression. This result is given by equation (25).

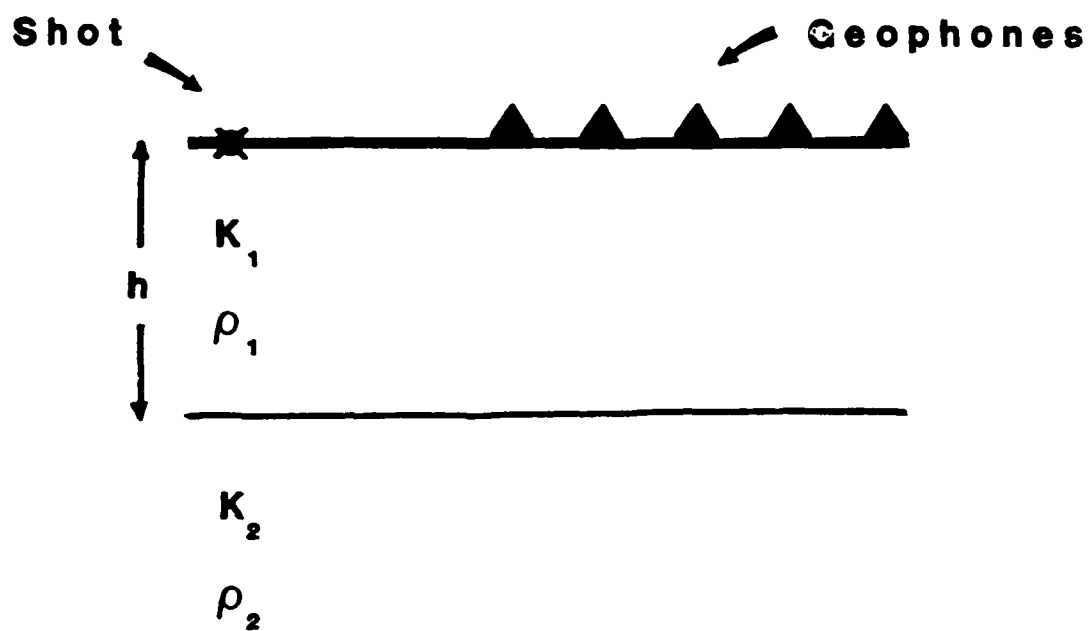


Figure 1. Diagram of the single interface experiment.

INPUT MODEL

0	C1 = 5000.0 D1 = 1.0000
1000	C2 = 5500.0 D2 = 1.0000

$$30.0 < F < 70.0$$

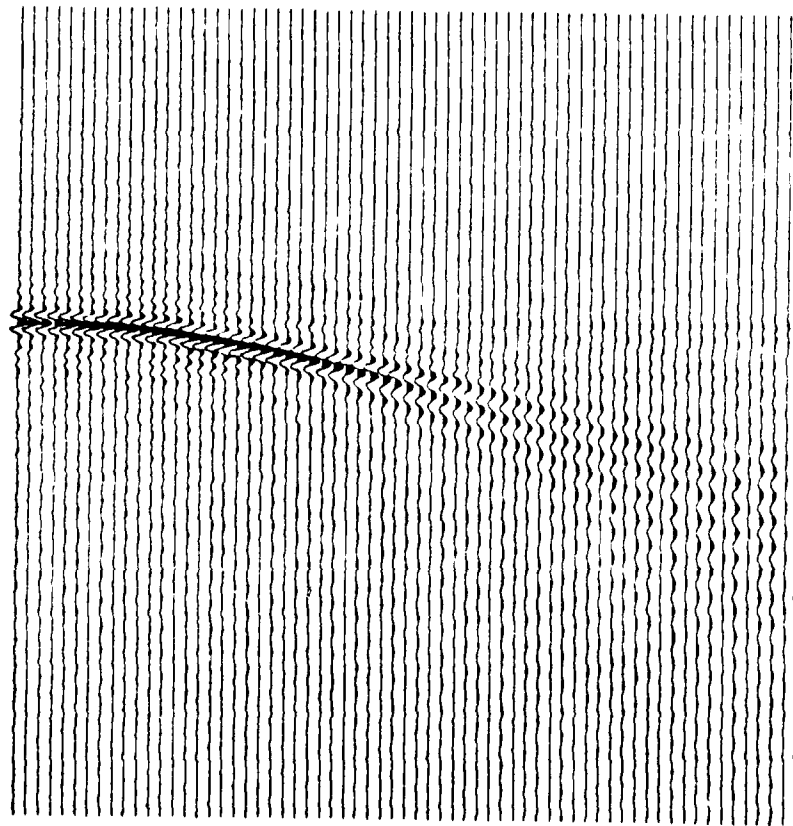


Figure 2. Shot record of a typical single interface forward model.

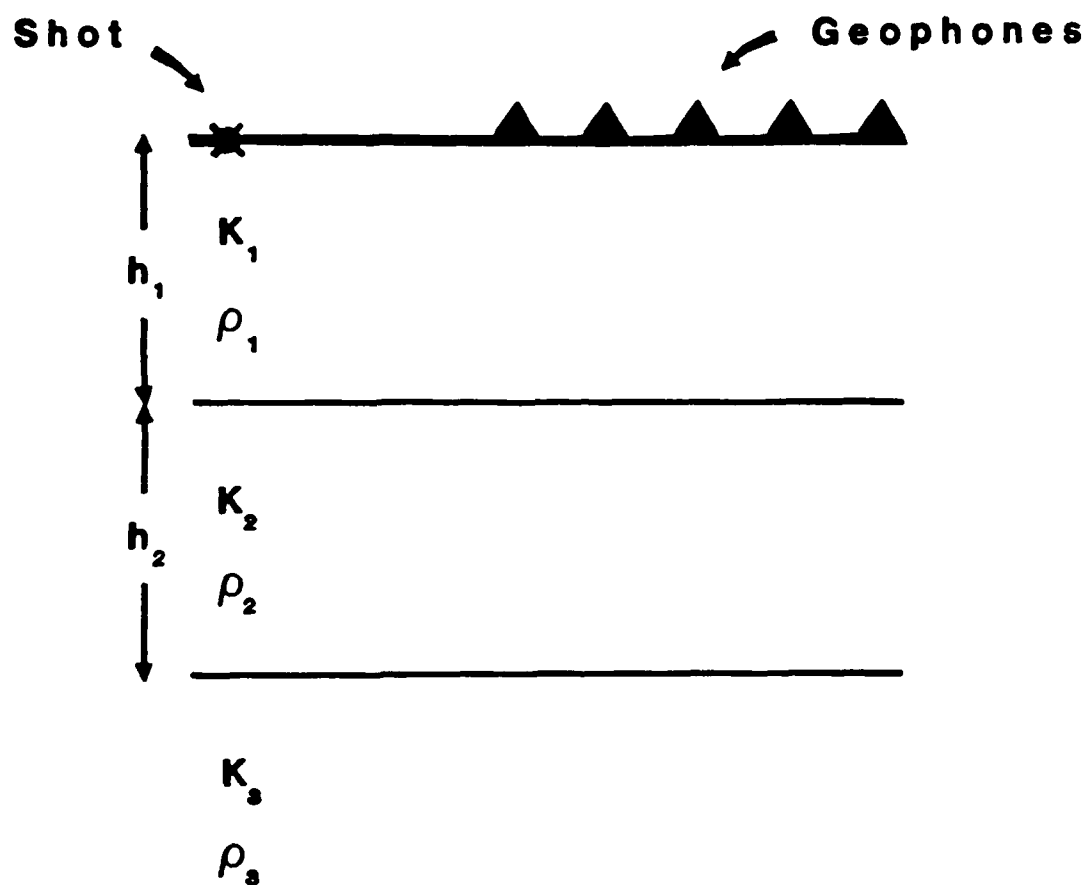


Figure 3. Diagram of the double interface experiment.

INPUT MODEL

0	C1 = 5000.0 D1 = 1.2100
500	C2 = 5500.0 D2 = 1.0000
1000	C3 = 5000.0 D3 = 1.2100

$$30.0 < F < 70.0$$

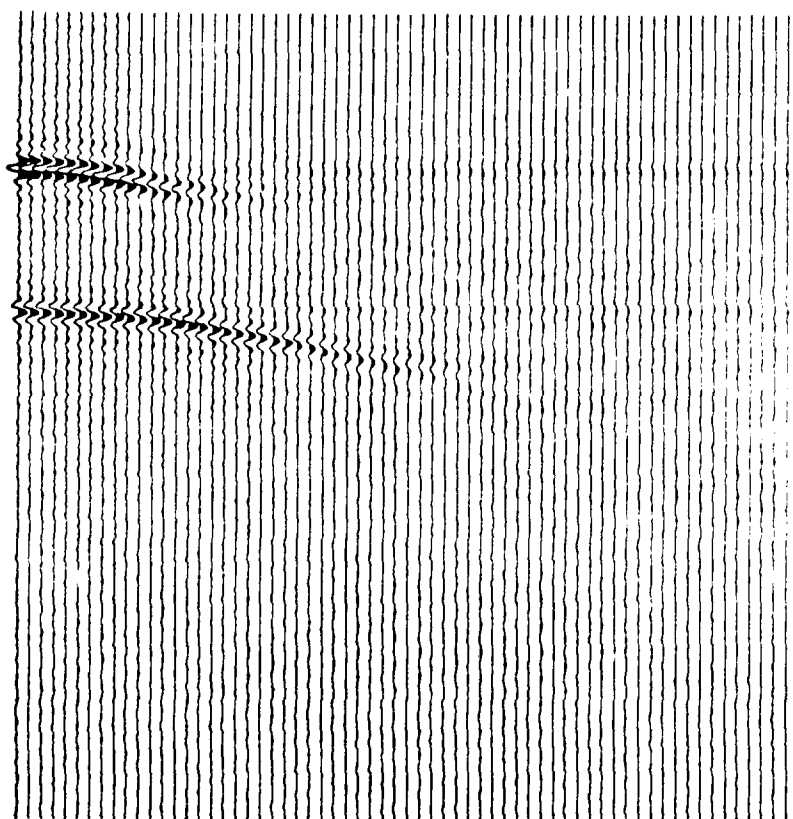


Figure 4. Shot record of a typical double interface forward model.

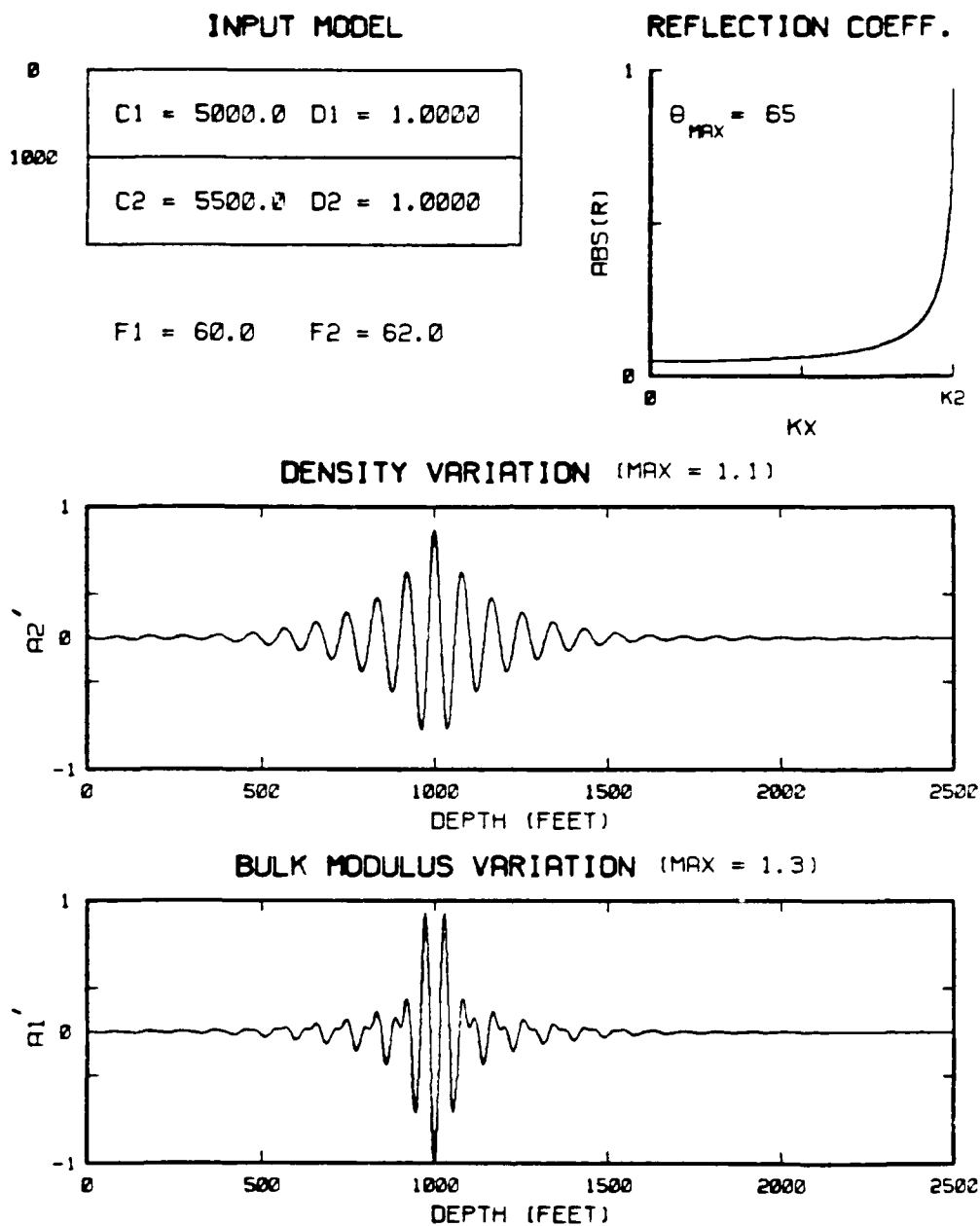


Figure 5. Fixed frequency, increasing velocity, constant density, single interface reconstruction for all pre-critical data.

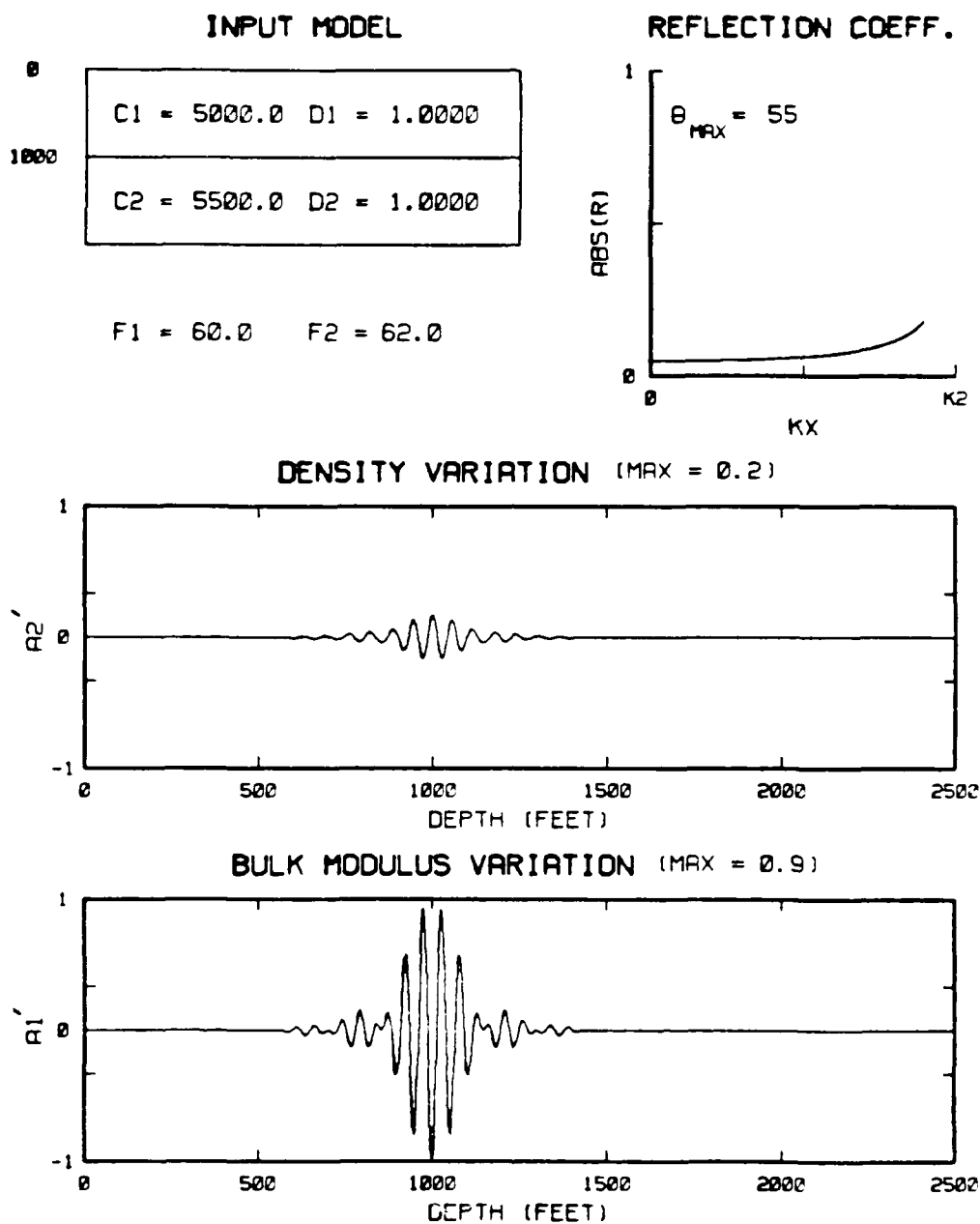


Figure 6. Fixed frequency, increasing velocity, constant density, single interface reconstruction for filtered data.

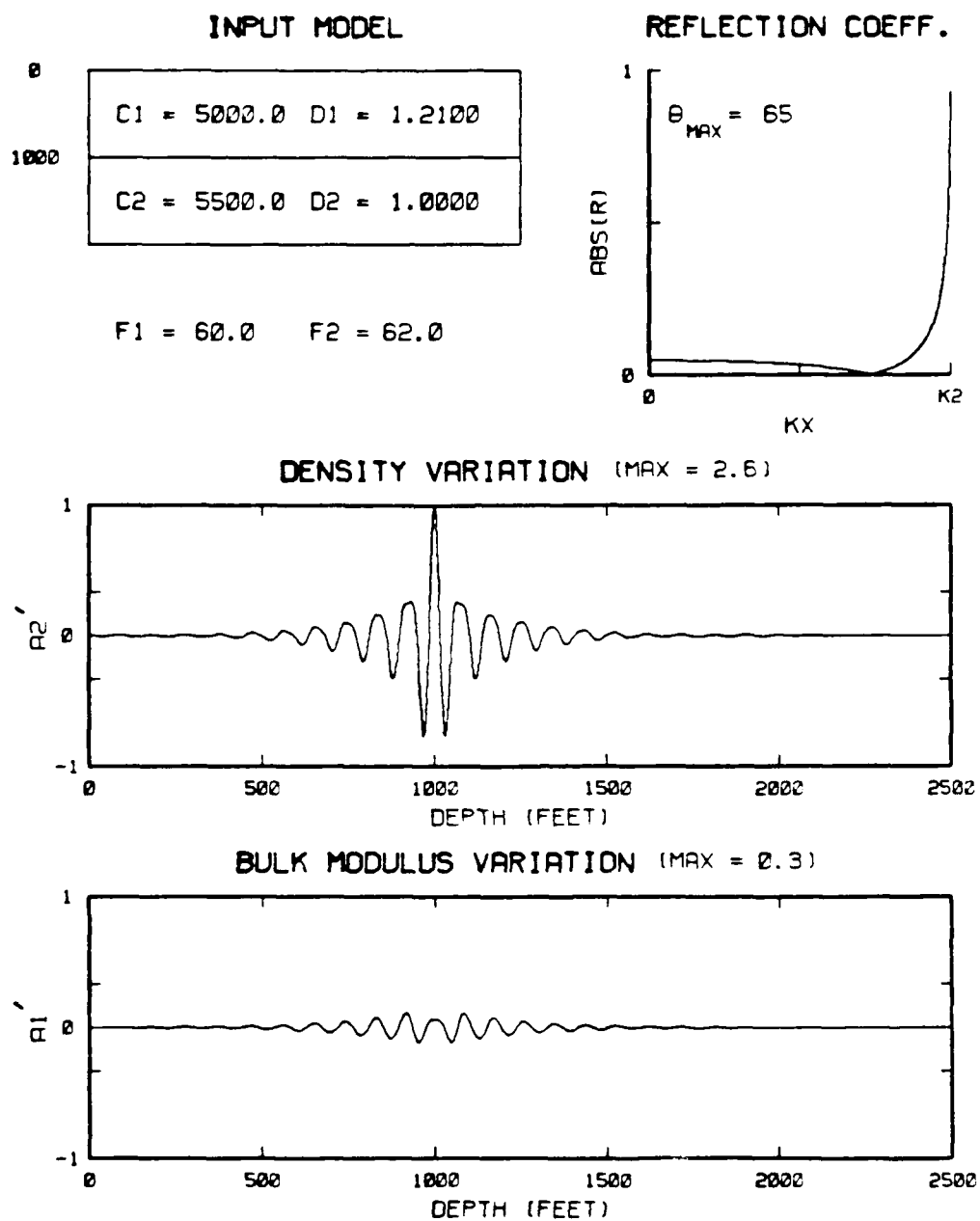


Figure 7. Fixed frequency, increasing velocity, constant bulk modulus, single interface reconstruction for all pre-critical data.

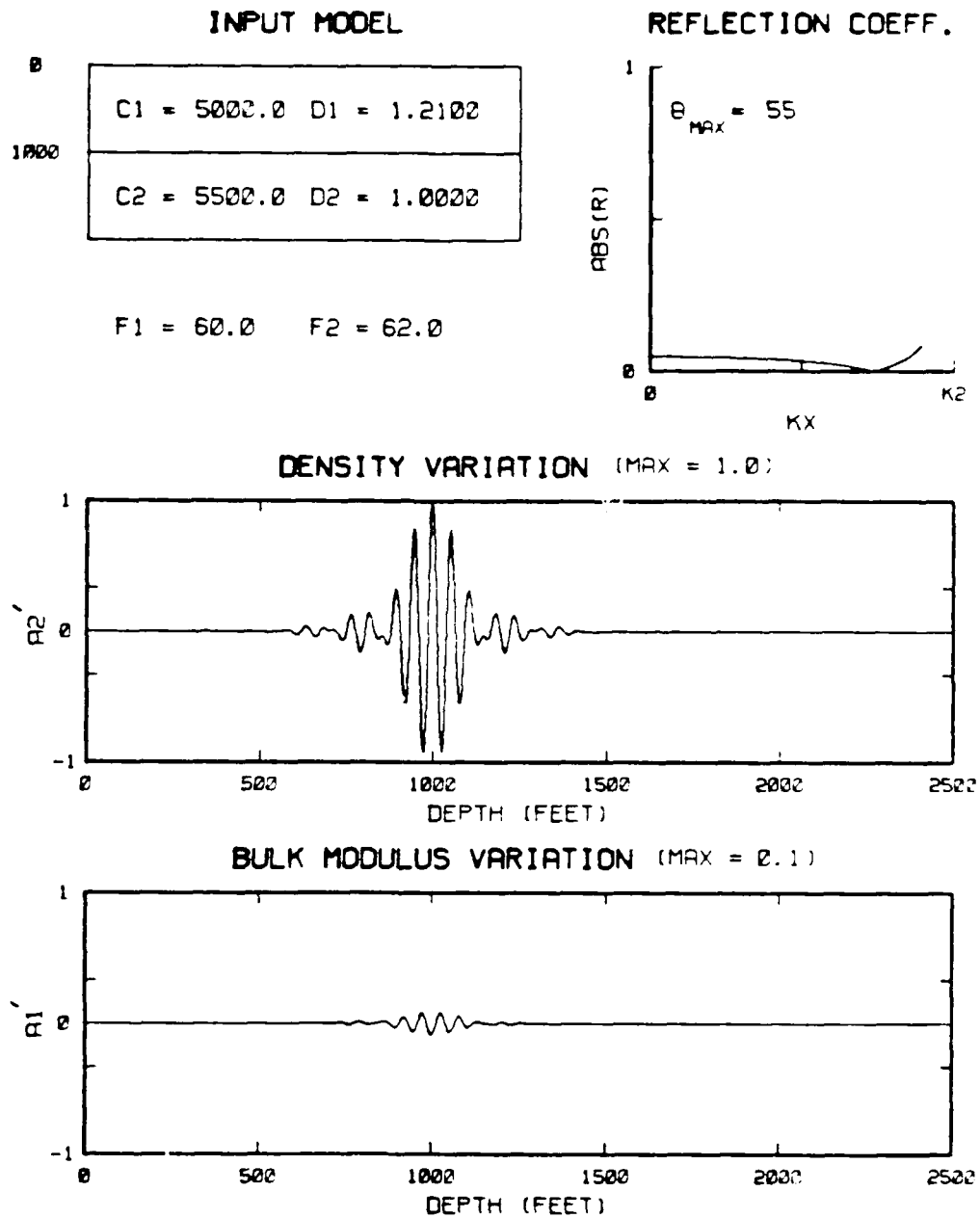


Figure 8. Fixed frequency, increasing velocity, constant bulk modulus, single interface reconstruction for filtered data.

AD-A156 394

ANALYSIS OF TWO-PARAMETER CONSTANT BACKGROUND BORN
INVERSION FOR ACOUSTIC. (U) COLORADO SCHOOL OF MINES
GOLDEN CENTER FOR WAVE PHENOMENA P B VIOLETTE

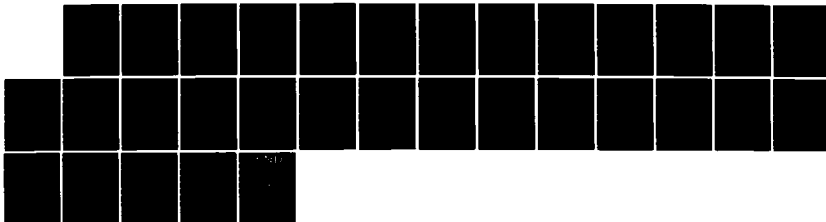
2/2

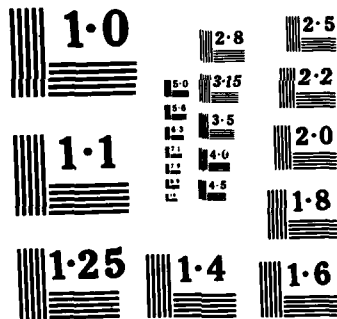
UNCLASSIFIED

15 MAY 85 CWP-029 N00014-84-K-0049

F/G 17/10

NL





NATIONAL BUREAU OF STANDARDS
MICROCOPY RESOLUTION TEST CHART

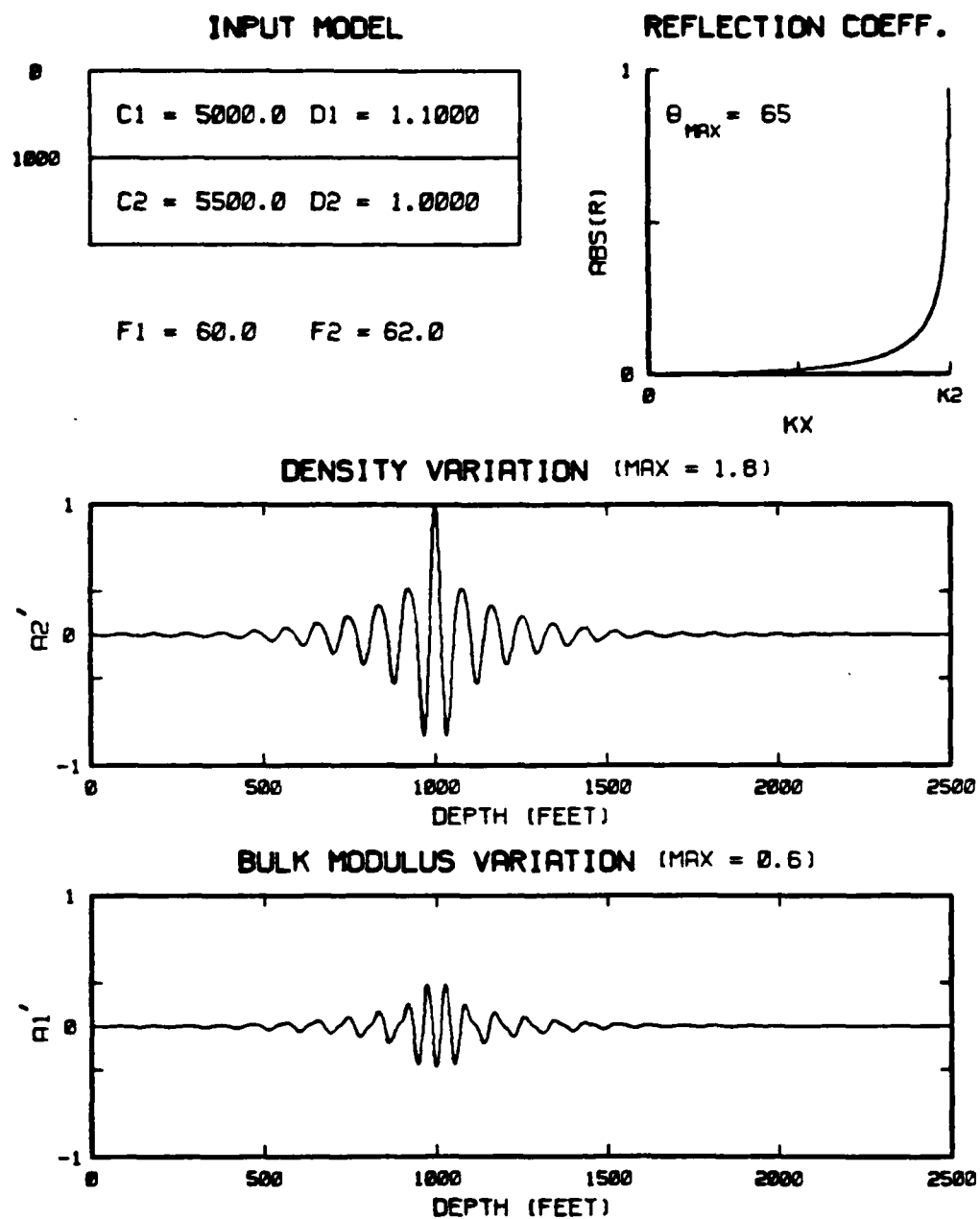


Figure 9. Fixed frequency, increasing velocity, constant impedance, single interface reconstruction for all pre-critical data.

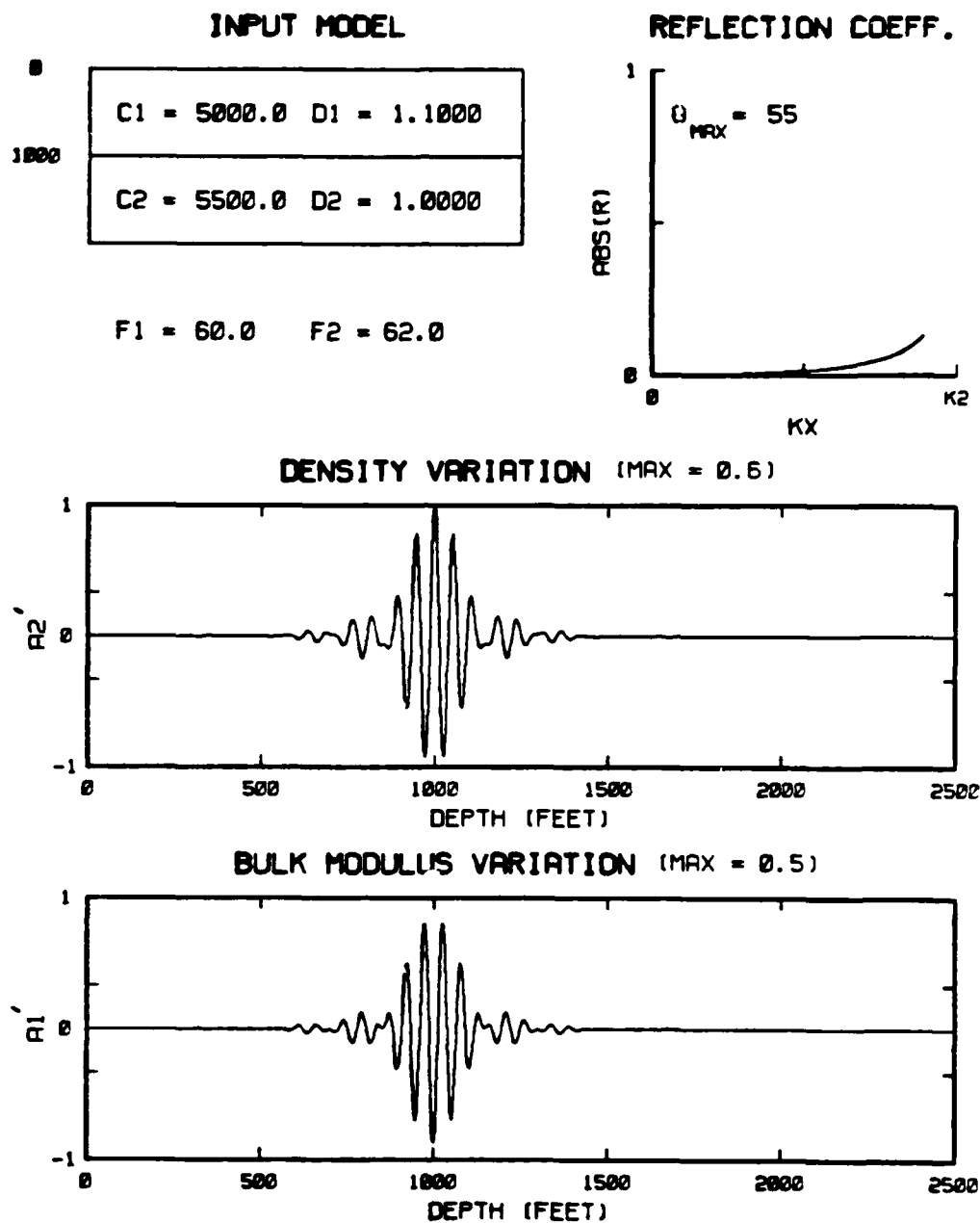


Figure 10. Fixed frequency, increasing velocity, constant impedance, single interface reconstruction for filtered data.

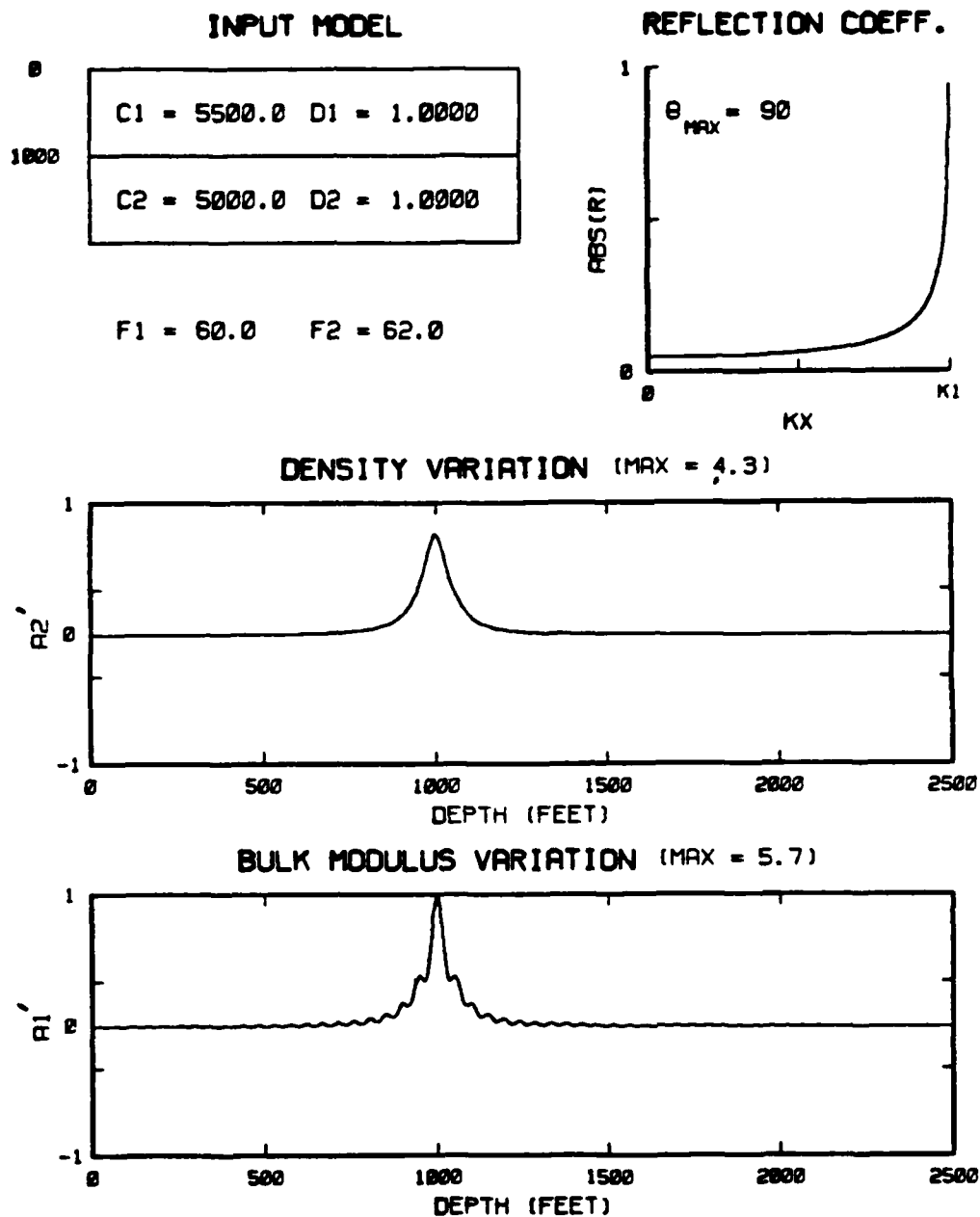


Figure 11. Fixed frequency, decreasing velocity, constant density, single interface reconstruction for broadband data.

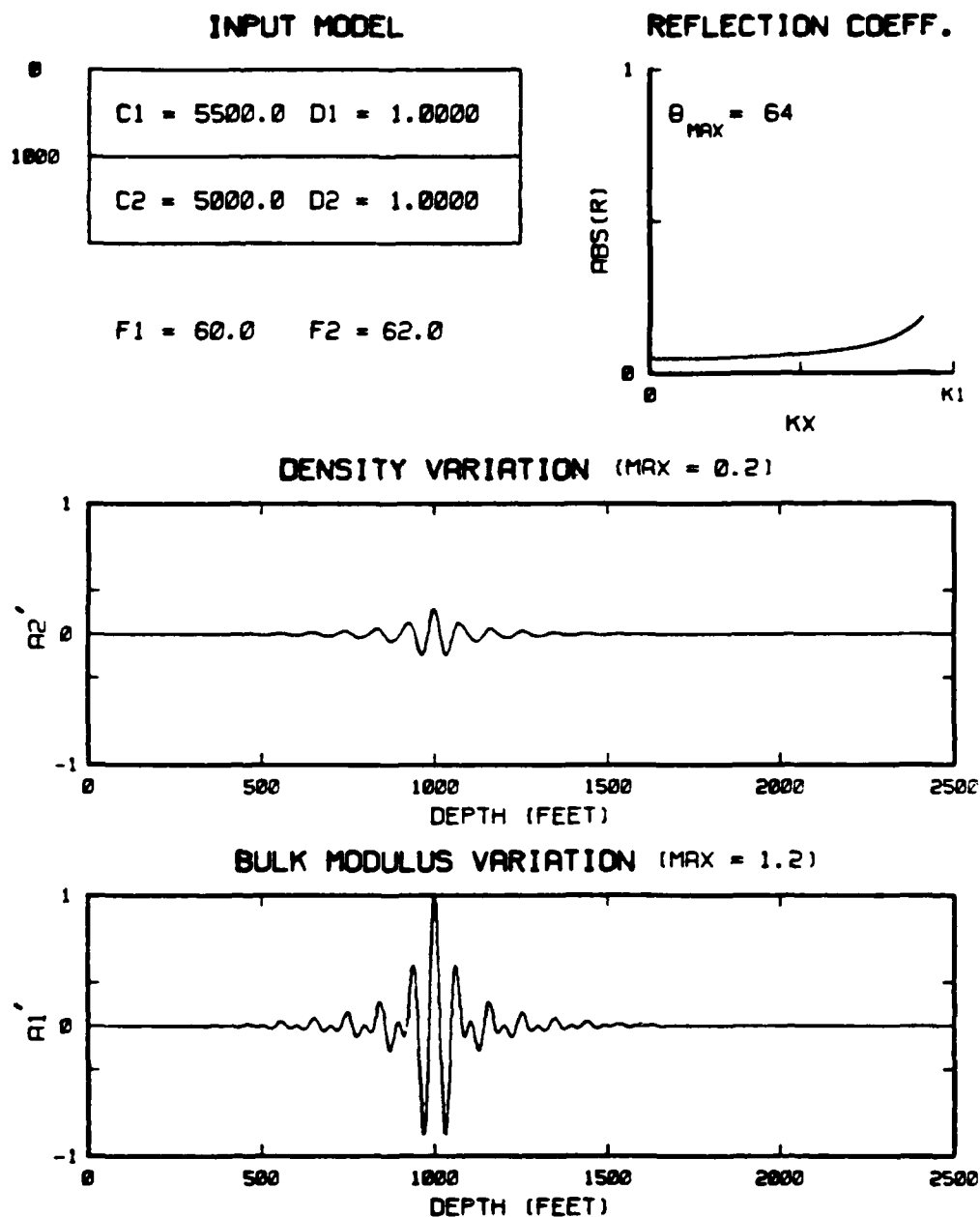


Figure 12. Fixed frequency, decreasing velocity, constant density, single interface reconstruction for filtered data.

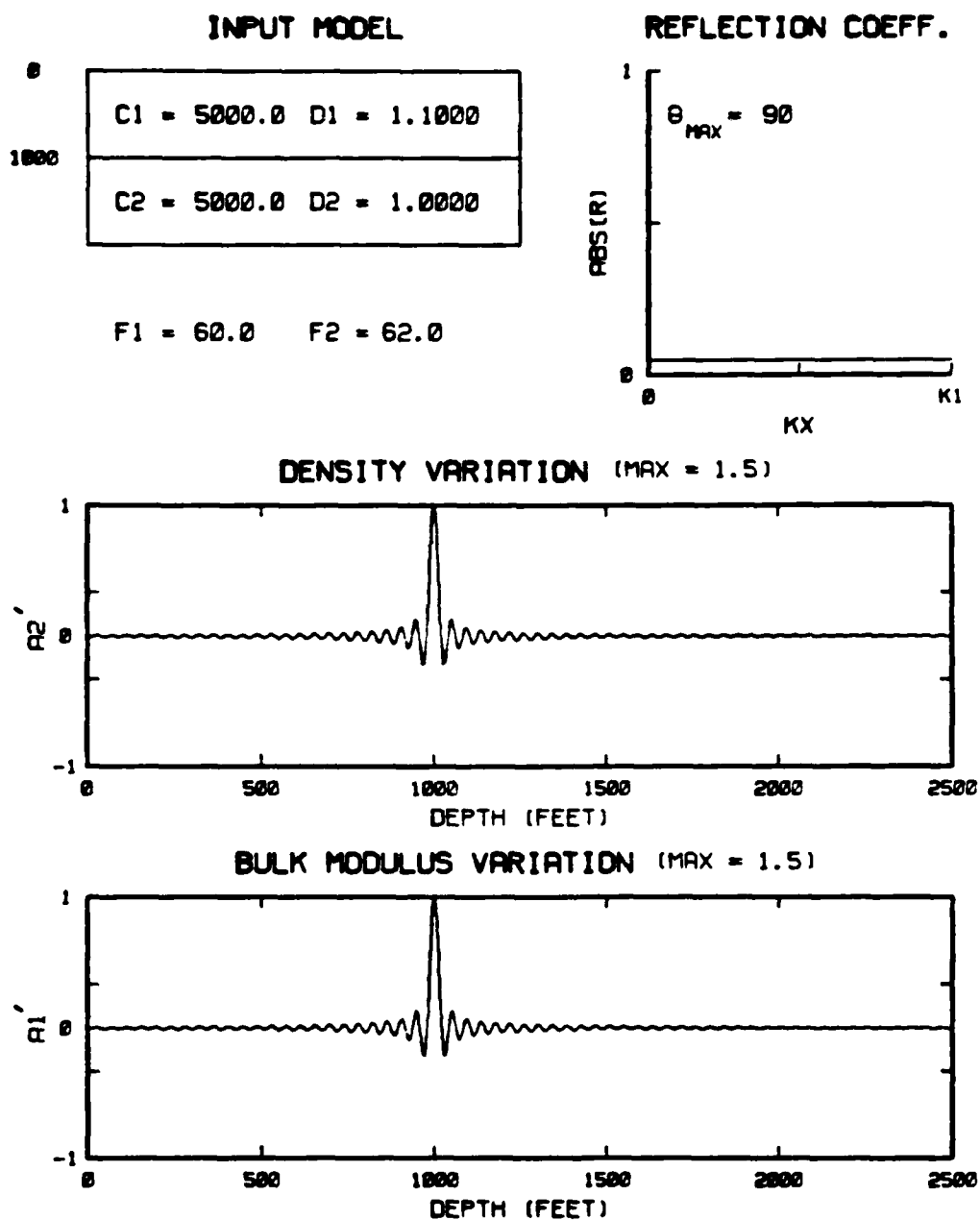


Figure 13. Fixed frequency, constant velocity, single interface reconstruction for broadband data.

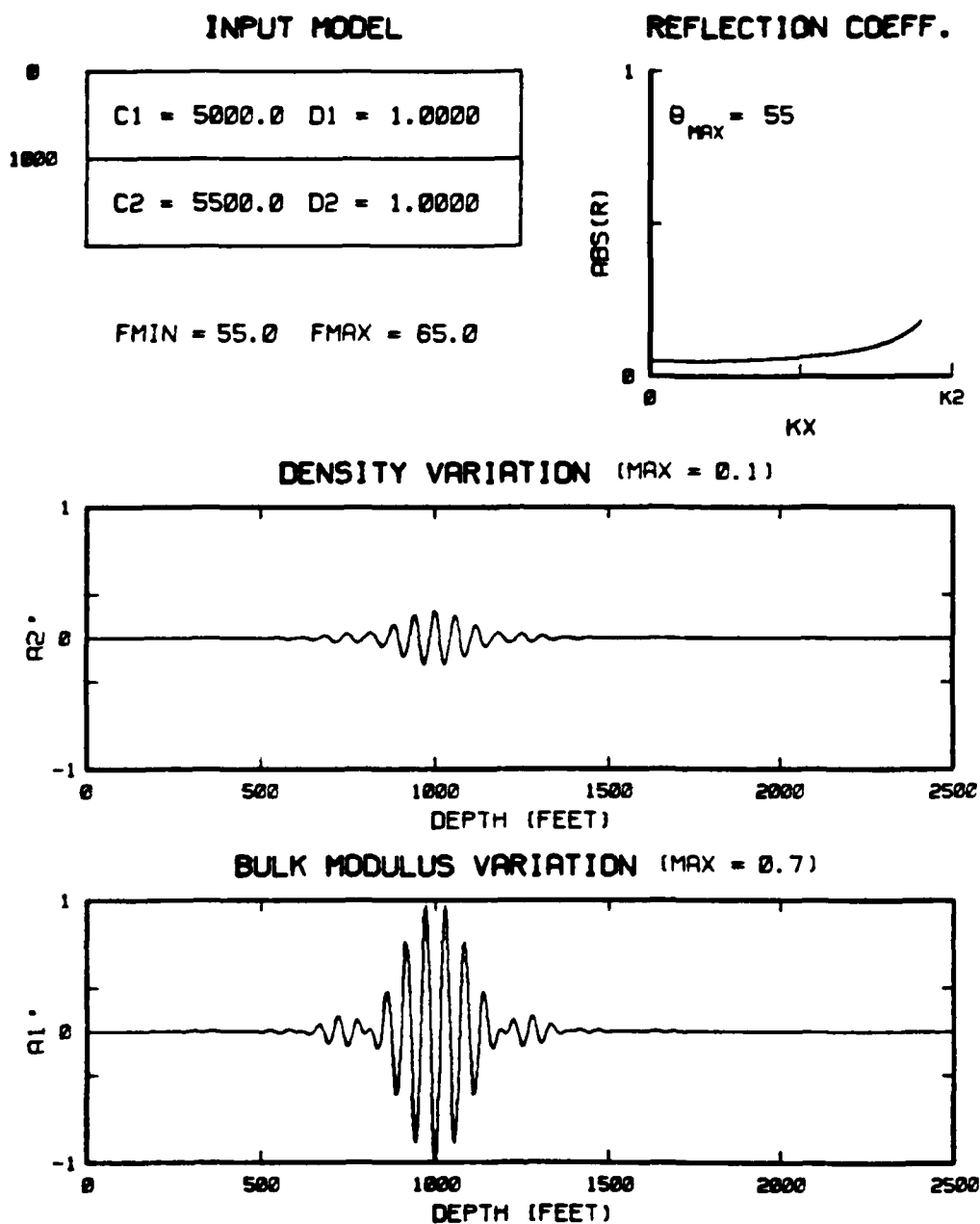


Figure 14. Least-squares, constant density, single interface reconstruction for the input model of Figure 6.

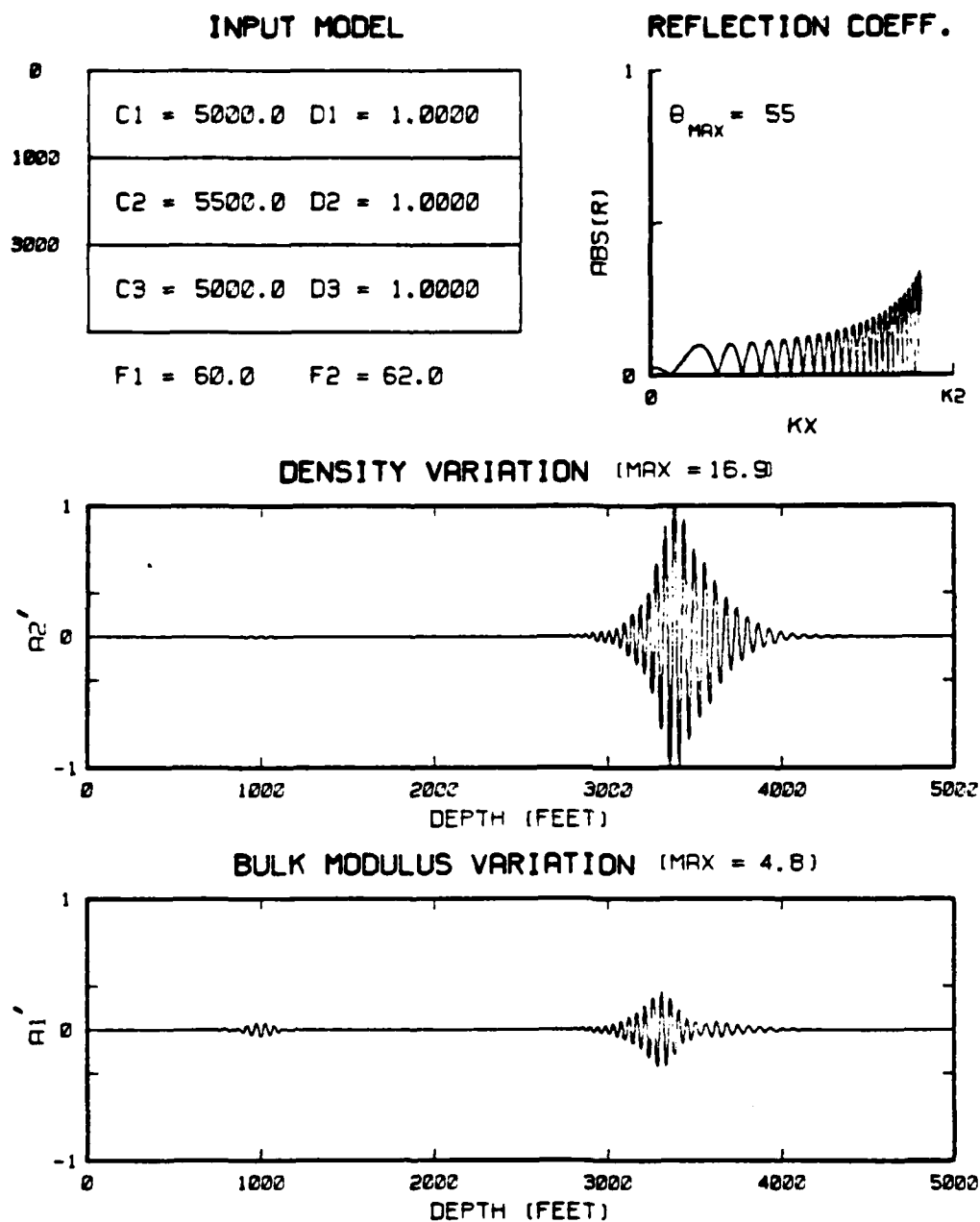


Figure 15. Fixed frequency, constant density, double interface reconstruction for 10% velocity changes.

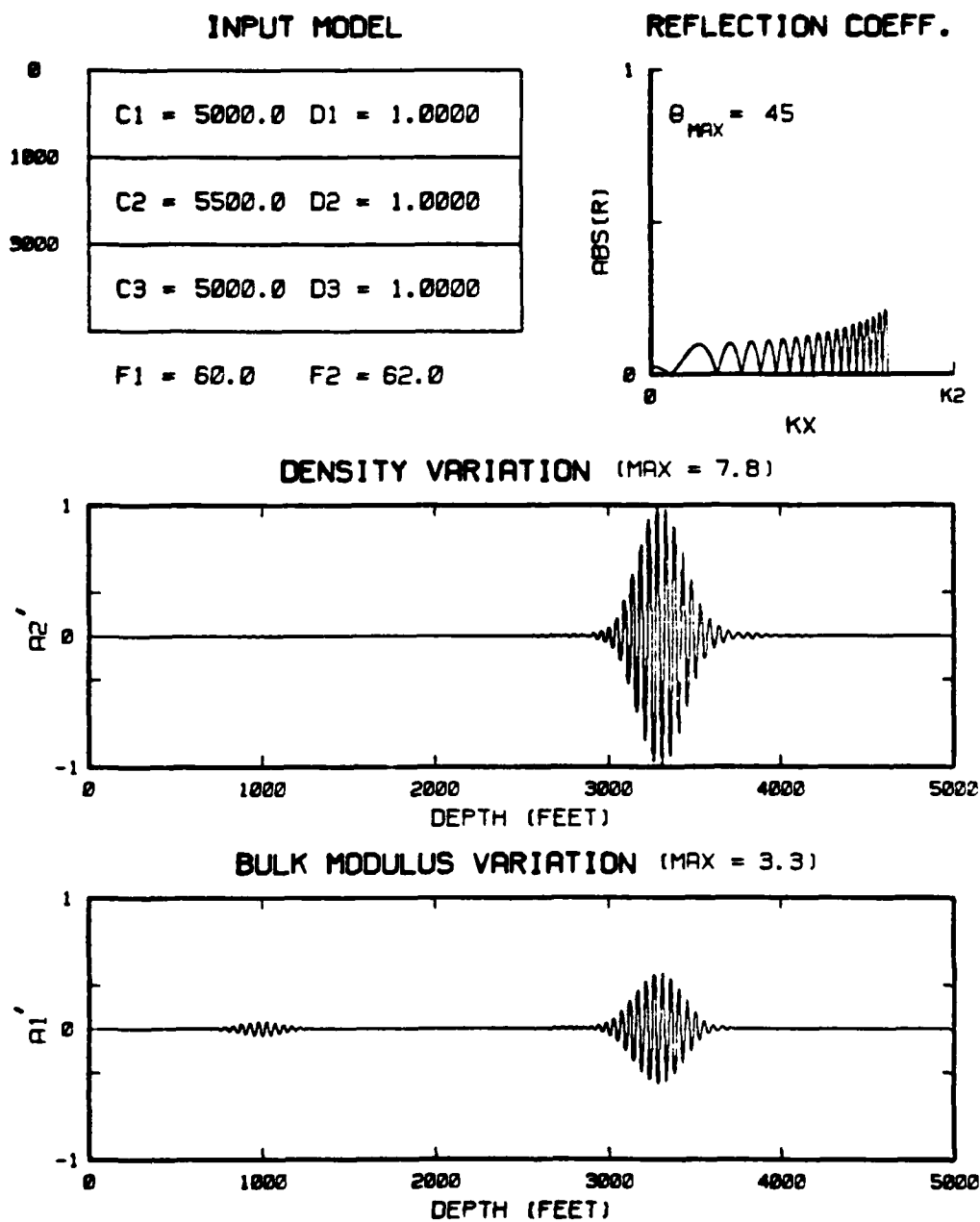


Figure 16. More highly filtered reconstruction of Figure 15.

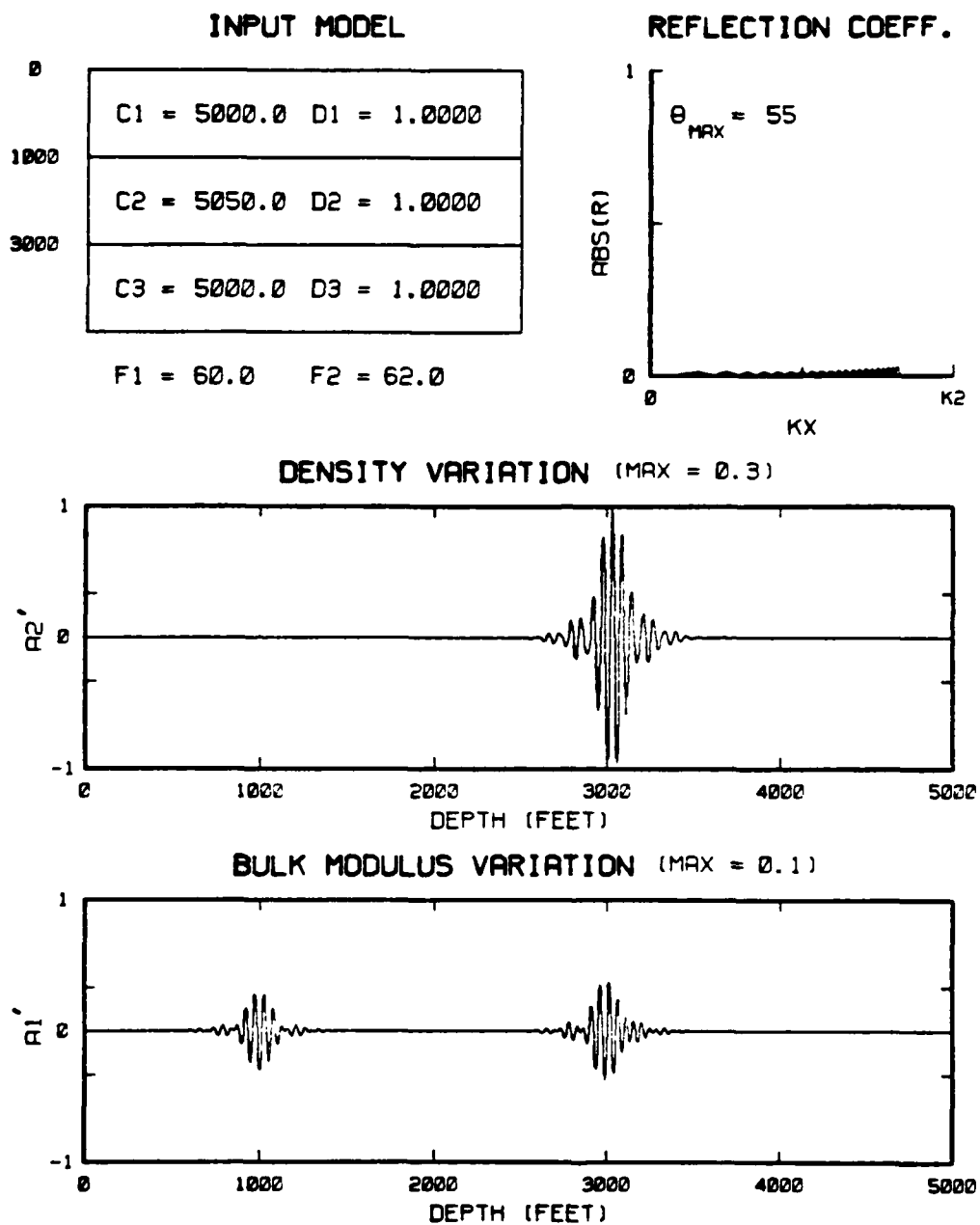


Figure 17. Fixed frequency, constant density, double interface reconstruction for 1% velocity changes.

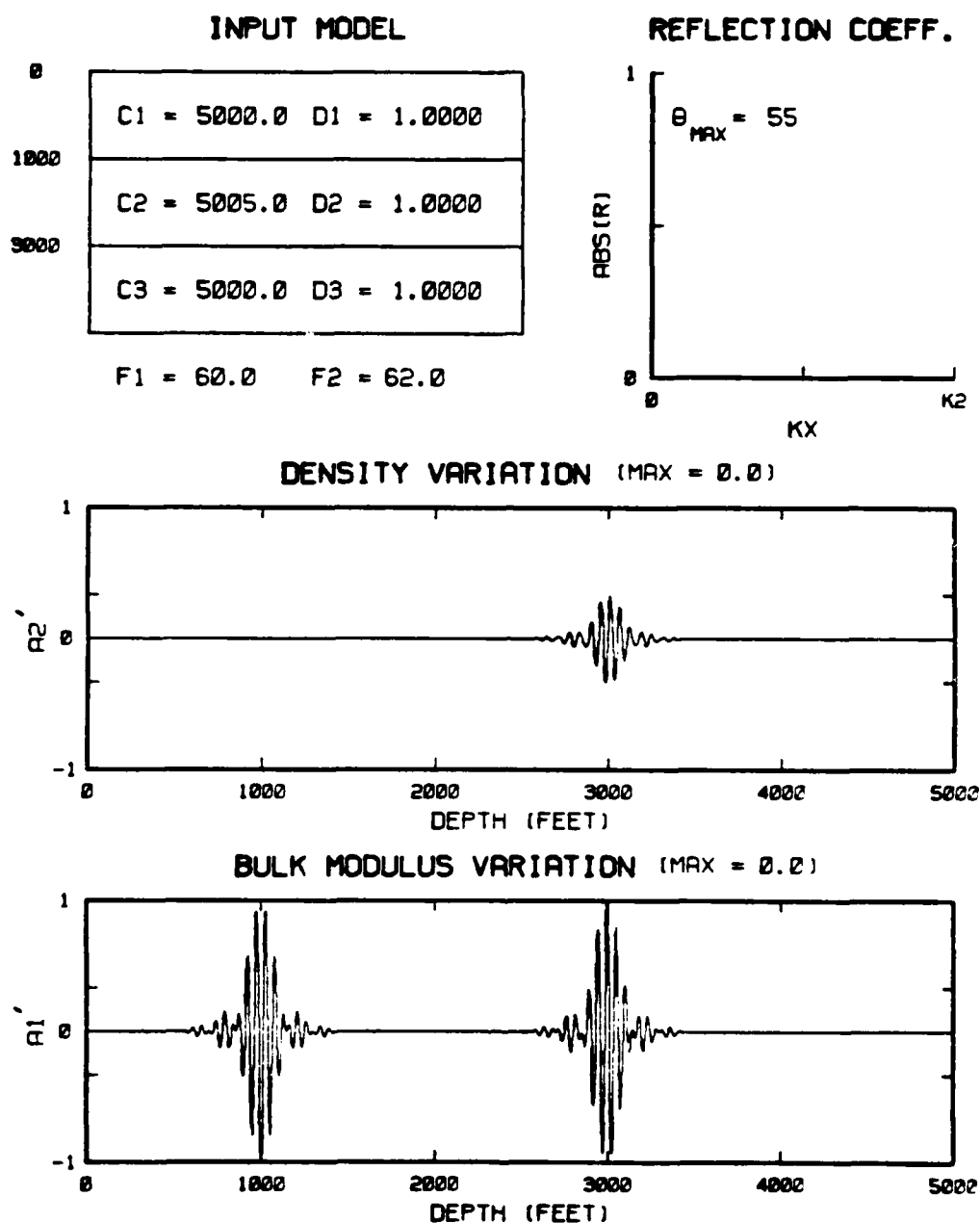


Figure 18. Fixed frequency, constant density, double interface reconstruction for 0.1% velocity changes.

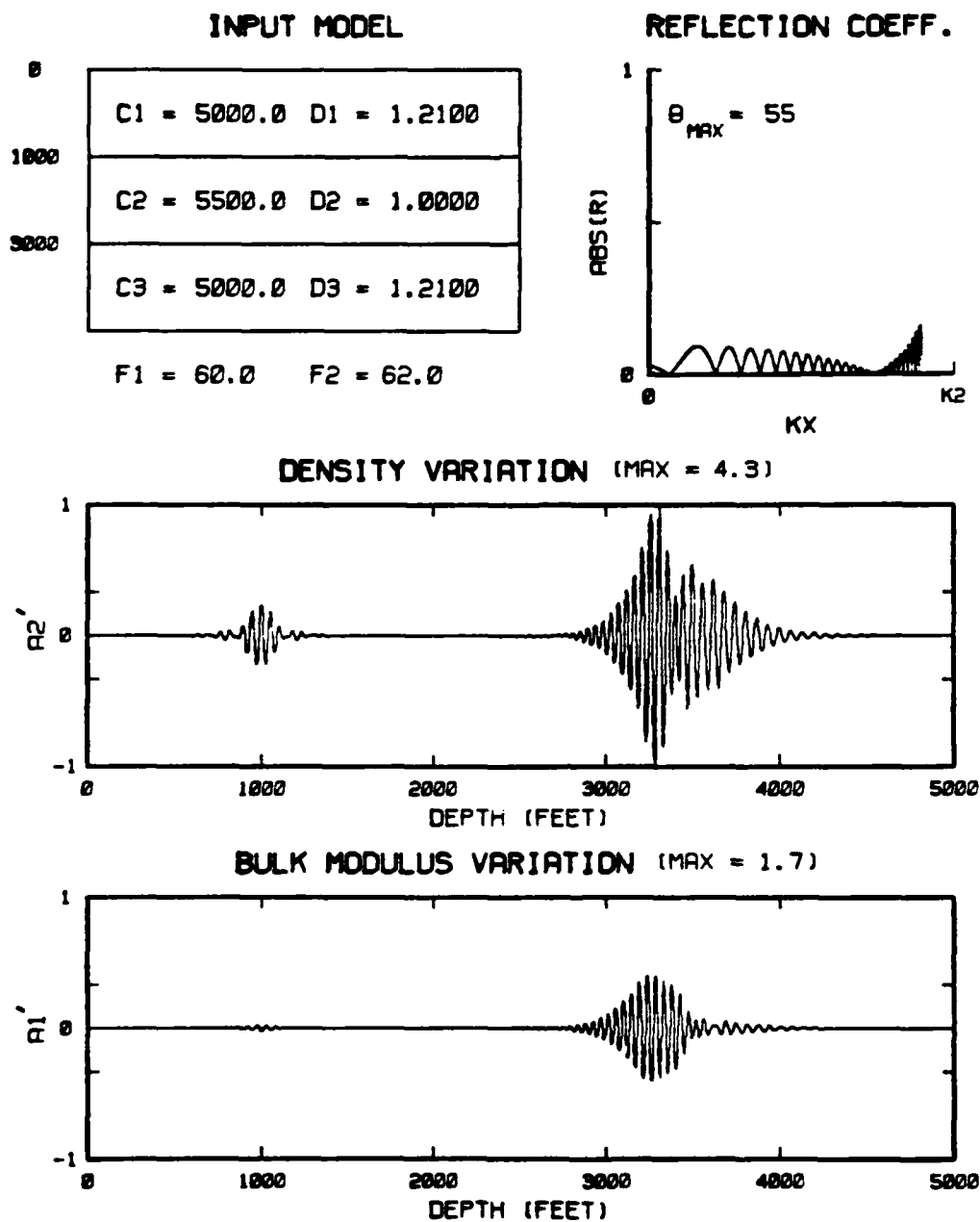


Figure 19. Fixed frequency, constant bulk modulus, double interface reconstruction for 10% velocity changes.

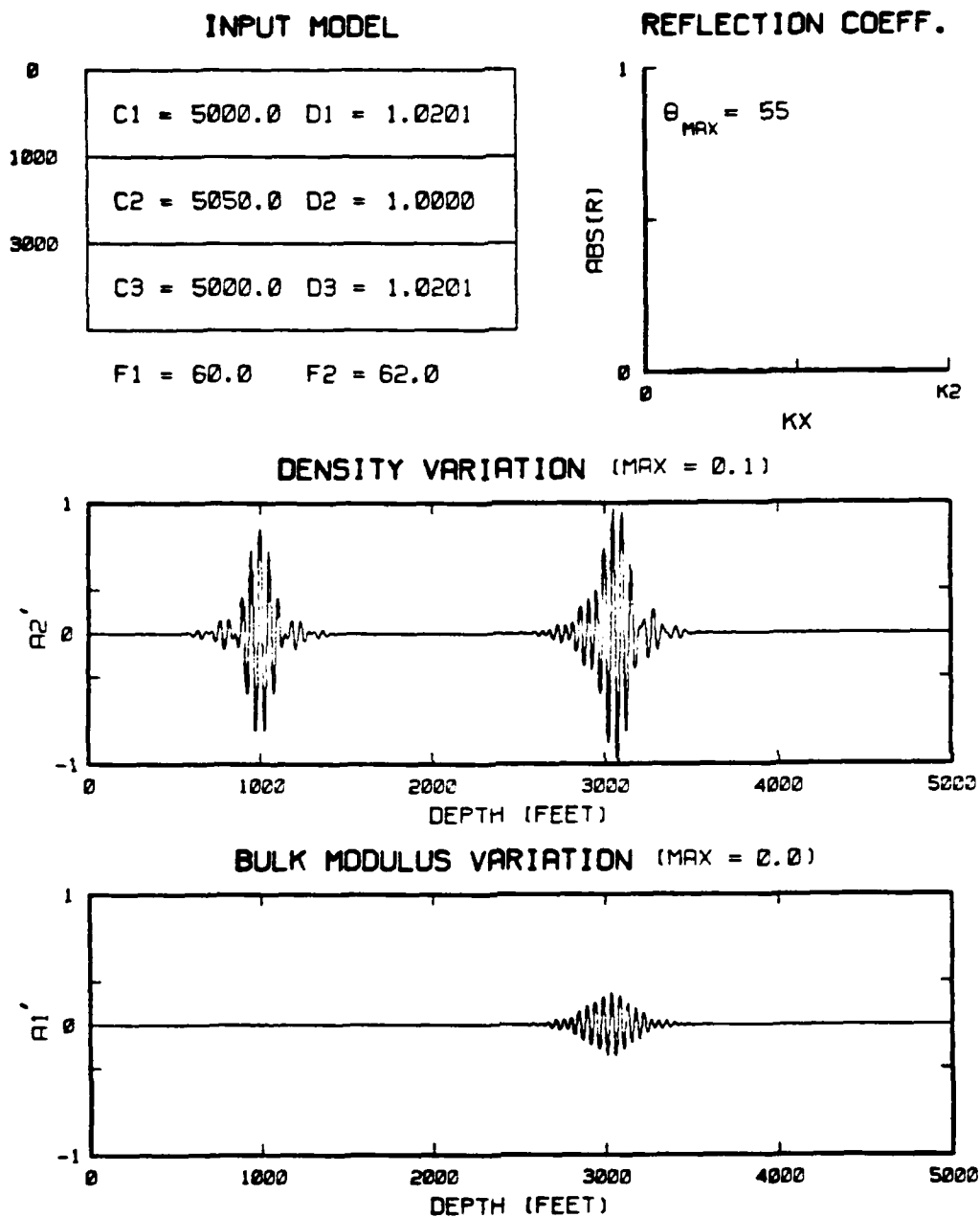


Figure 20. Fixed frequency, constant bulk modulus, double interface reconstruction for 1% velocity changes.

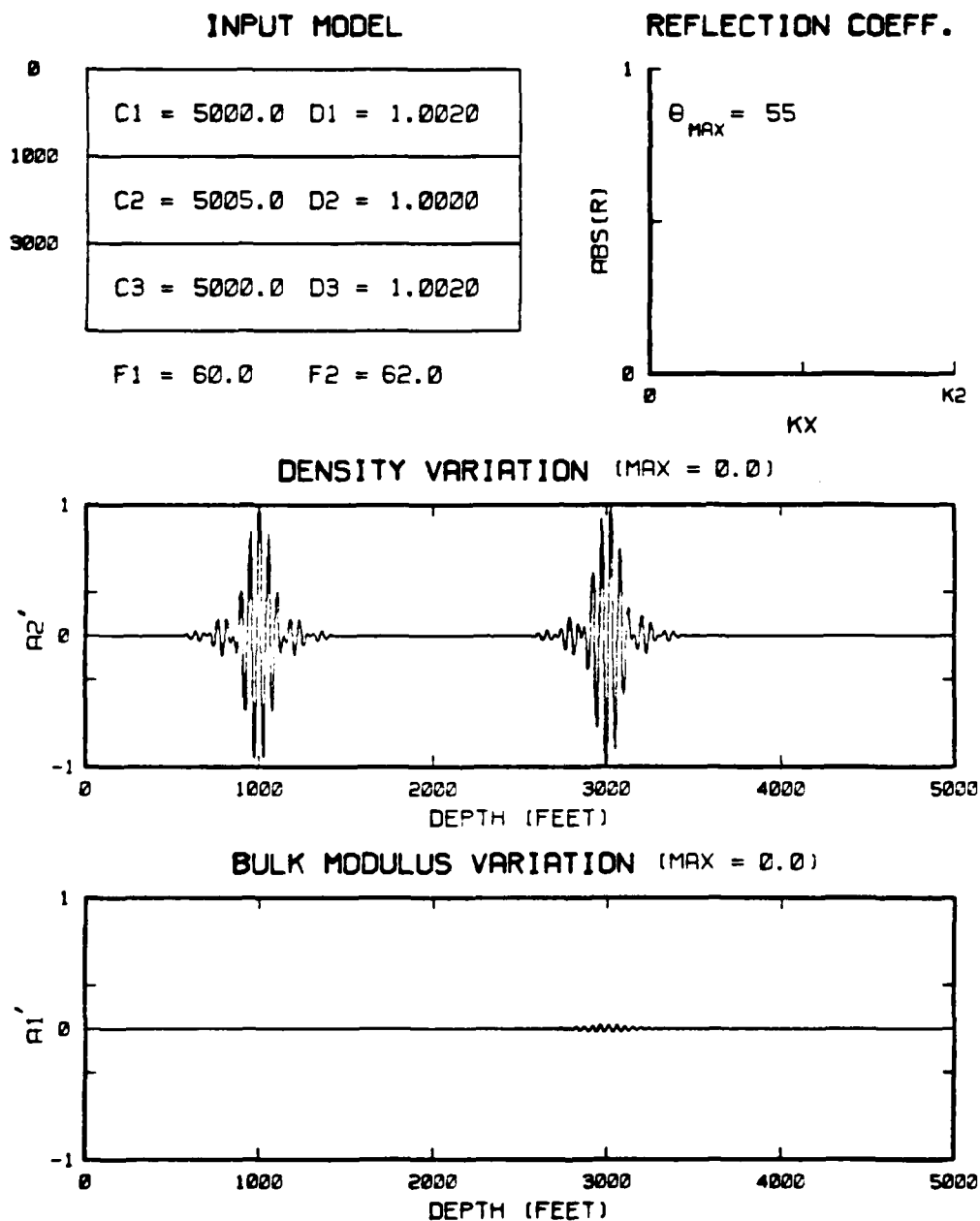


Figure 21. Fixed frequency, constant bulk modulus, double interface reconstruction for 0.1% velocity changes.

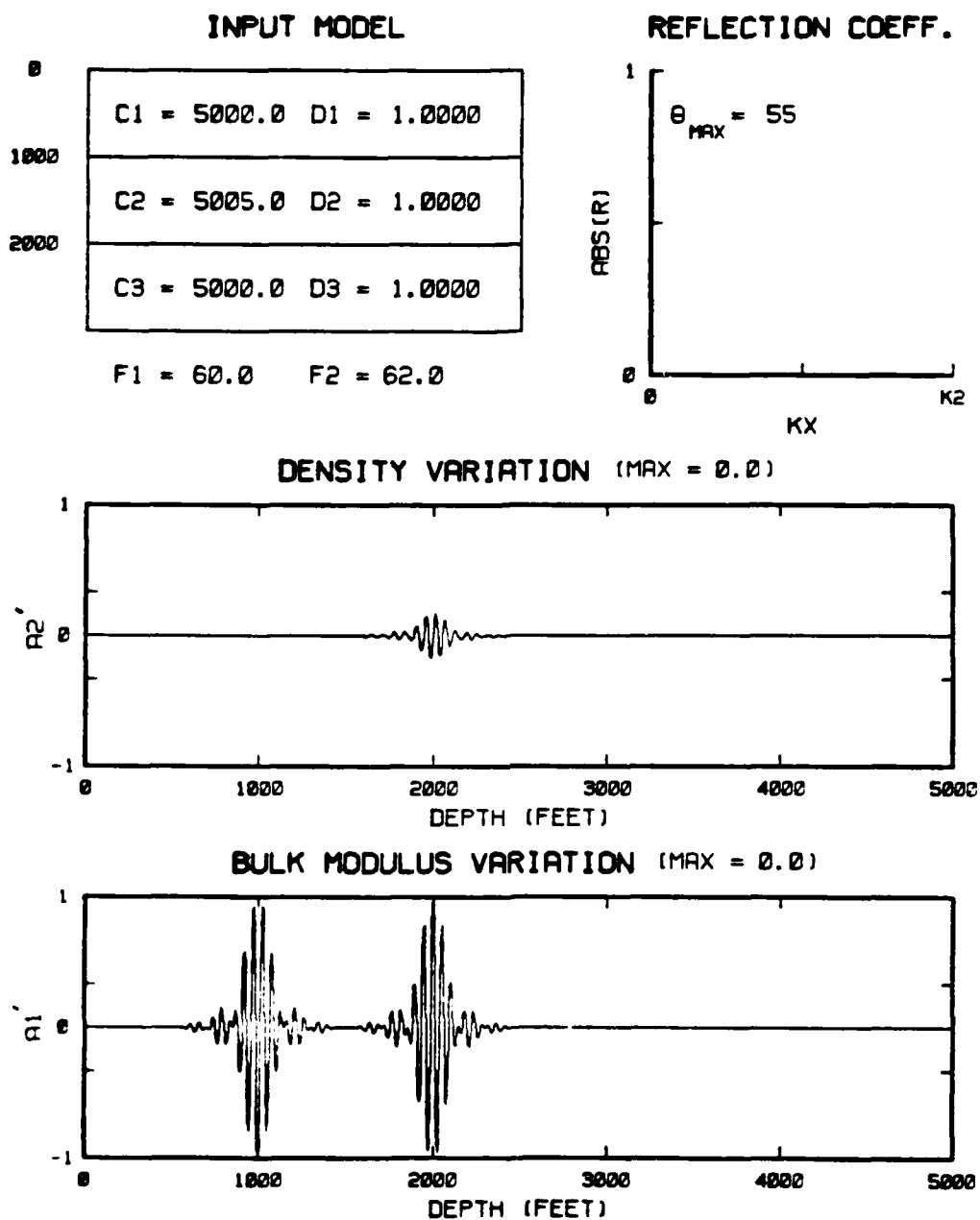


Figure 22. Reconstruction of the model of Figure 18 but for a shallower second reflector.

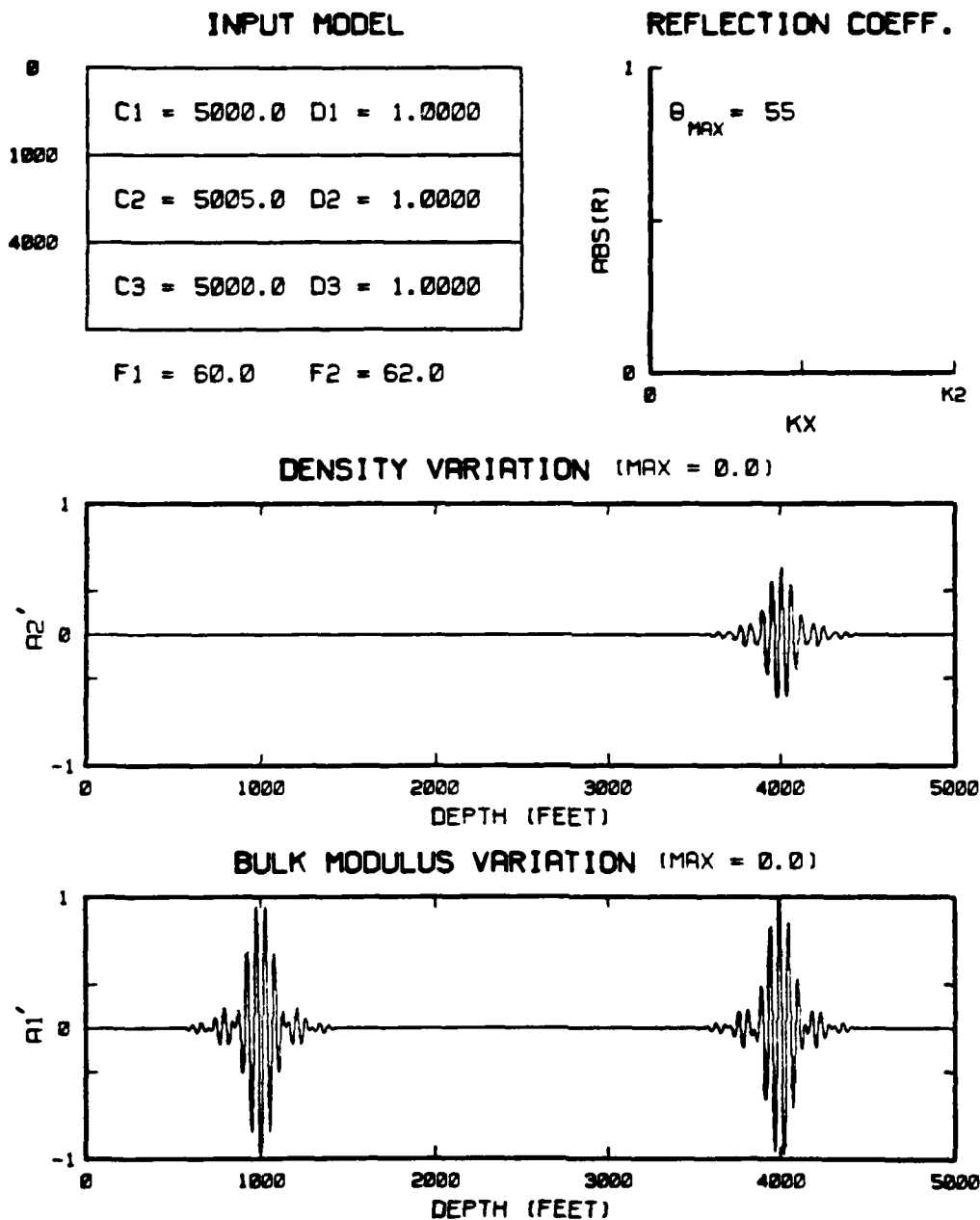


Figure 23. Reconstruction of the model of Figure 18 but for a deeper second reflector.

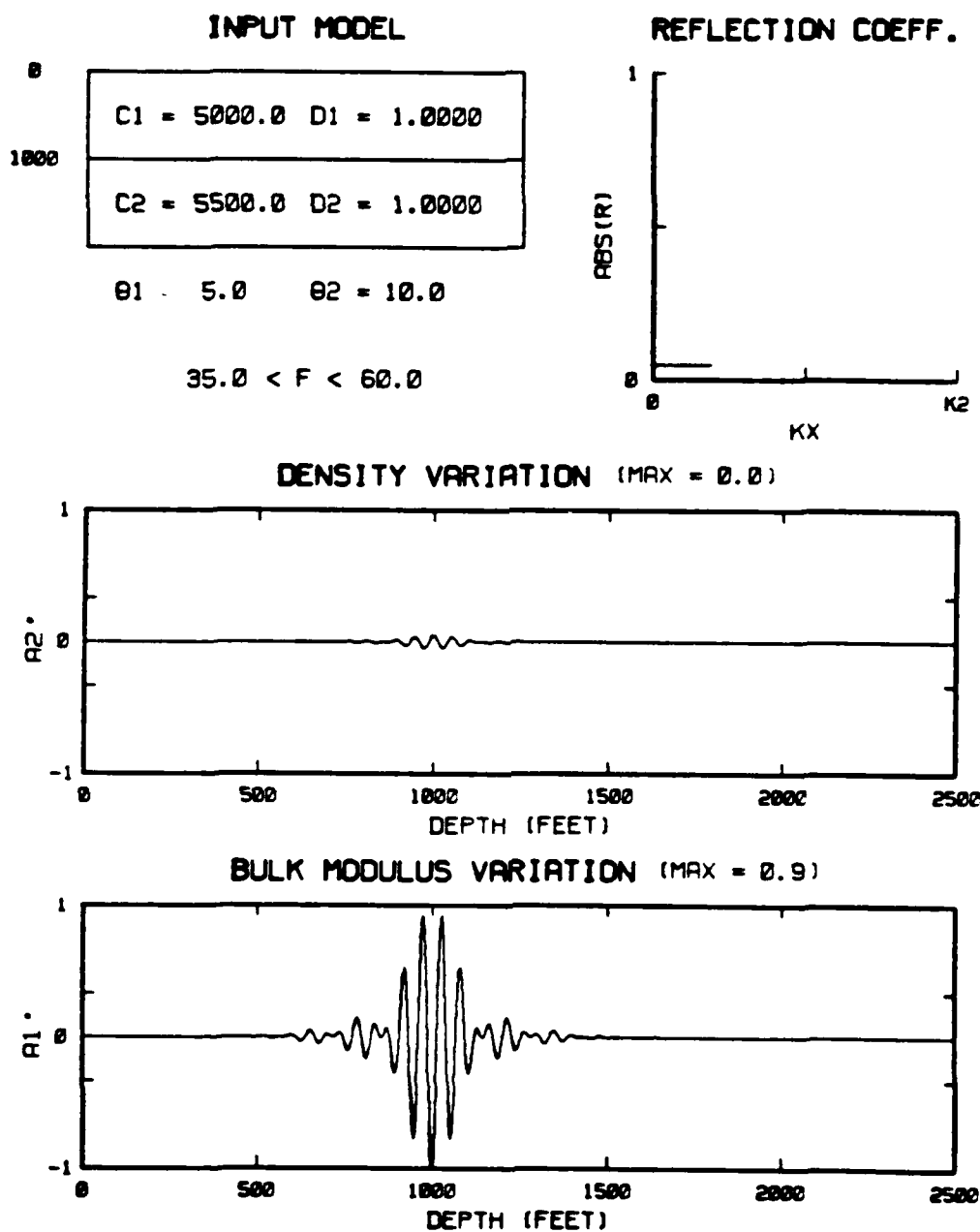


Figure 24. Fixed angle reconstruction of the model of Figure 6.

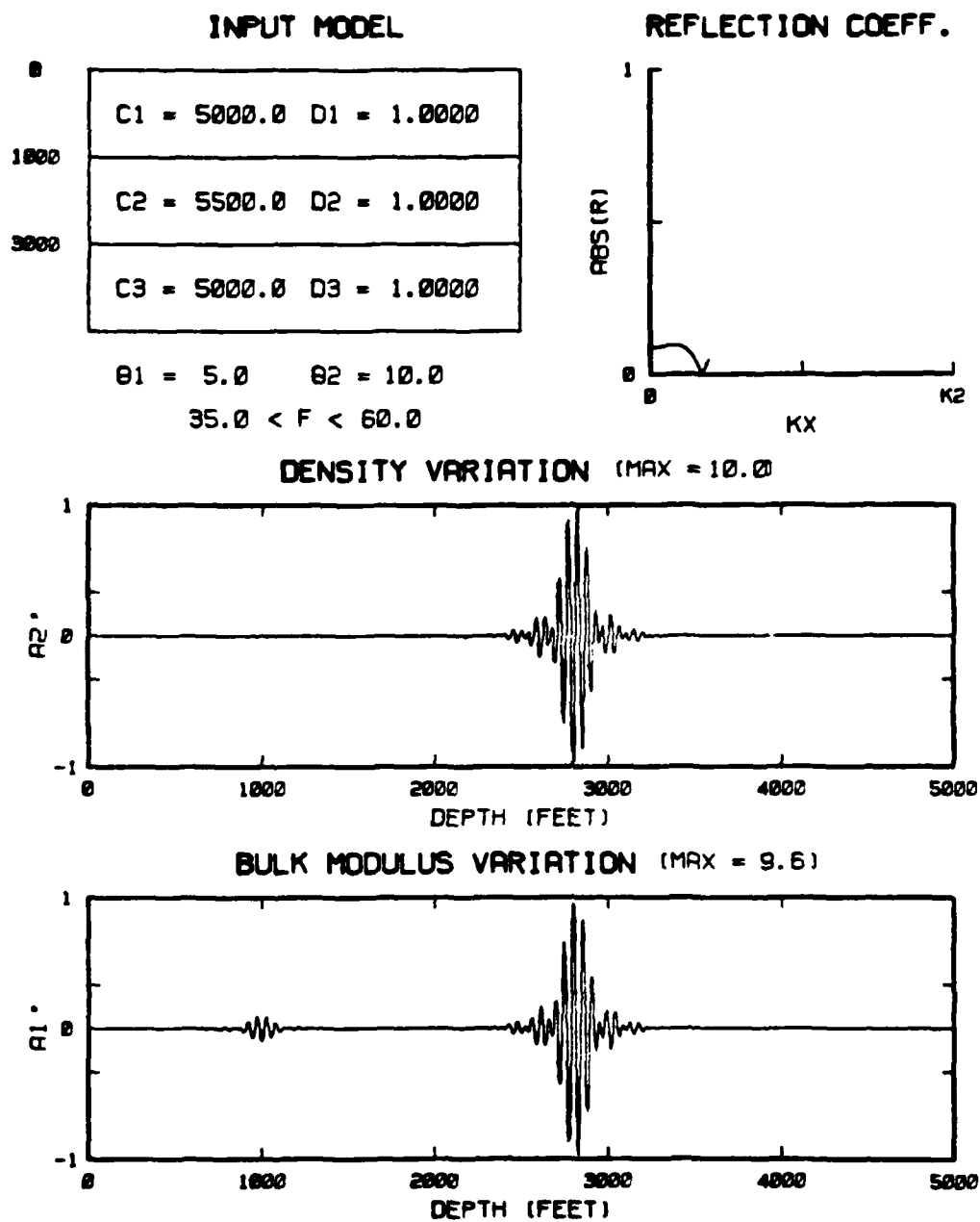


Figure 25. Fixed angle reconstruction of the model of Figure 15.

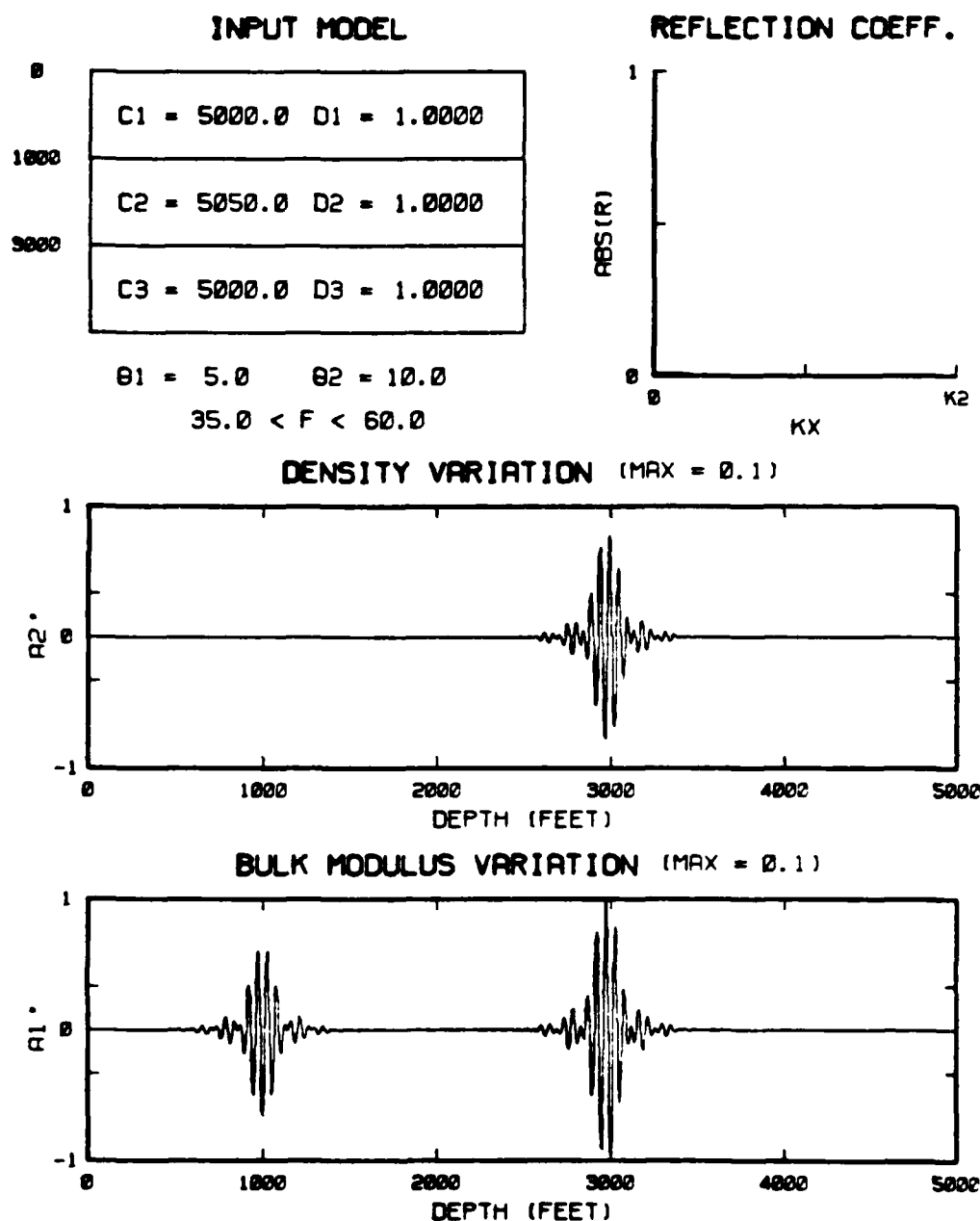


Figure 26. Fixed angle reconstruction of the model of Figure 17.

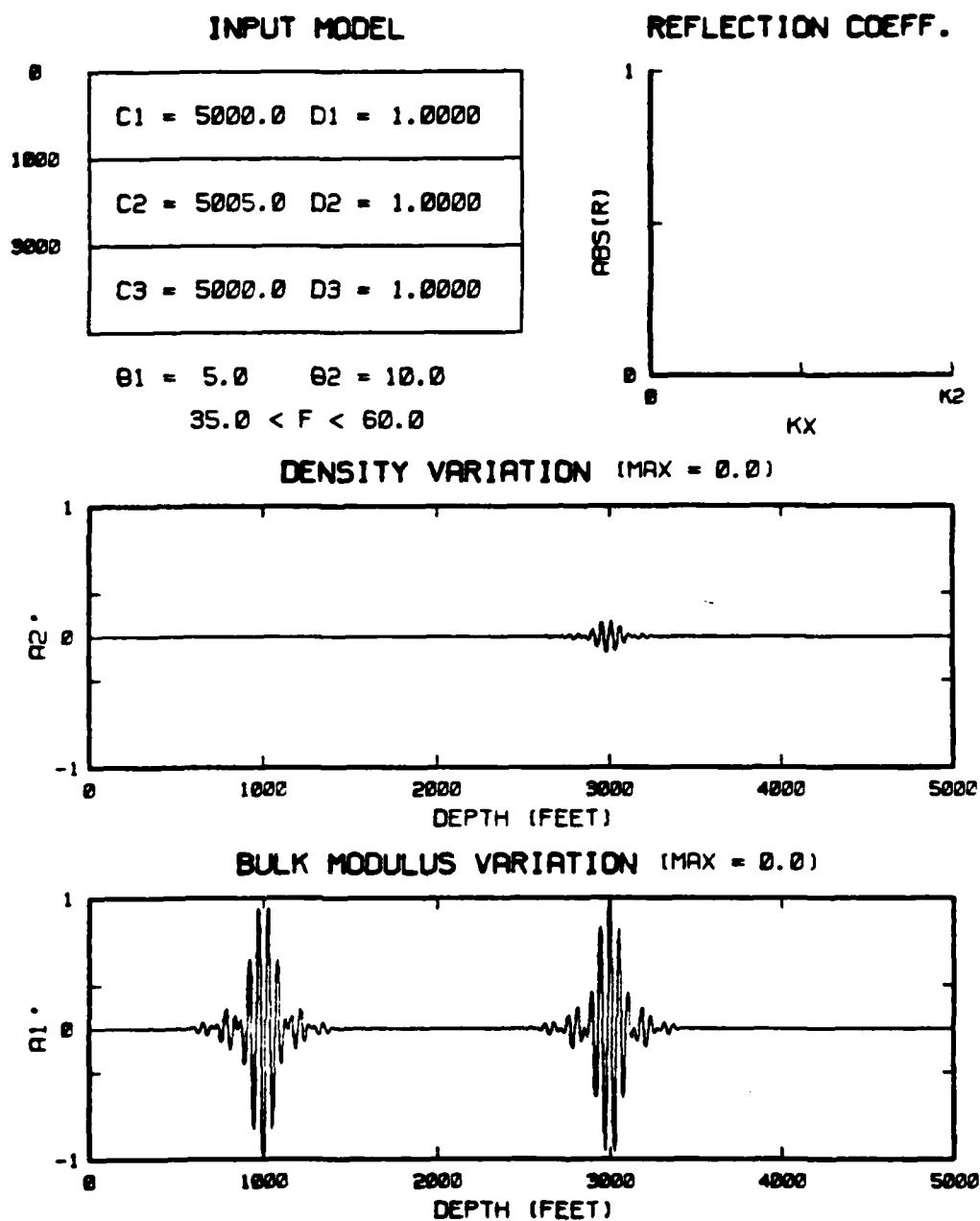


Figure 27. Fixed angle reconstruction of the model of Figure 18.

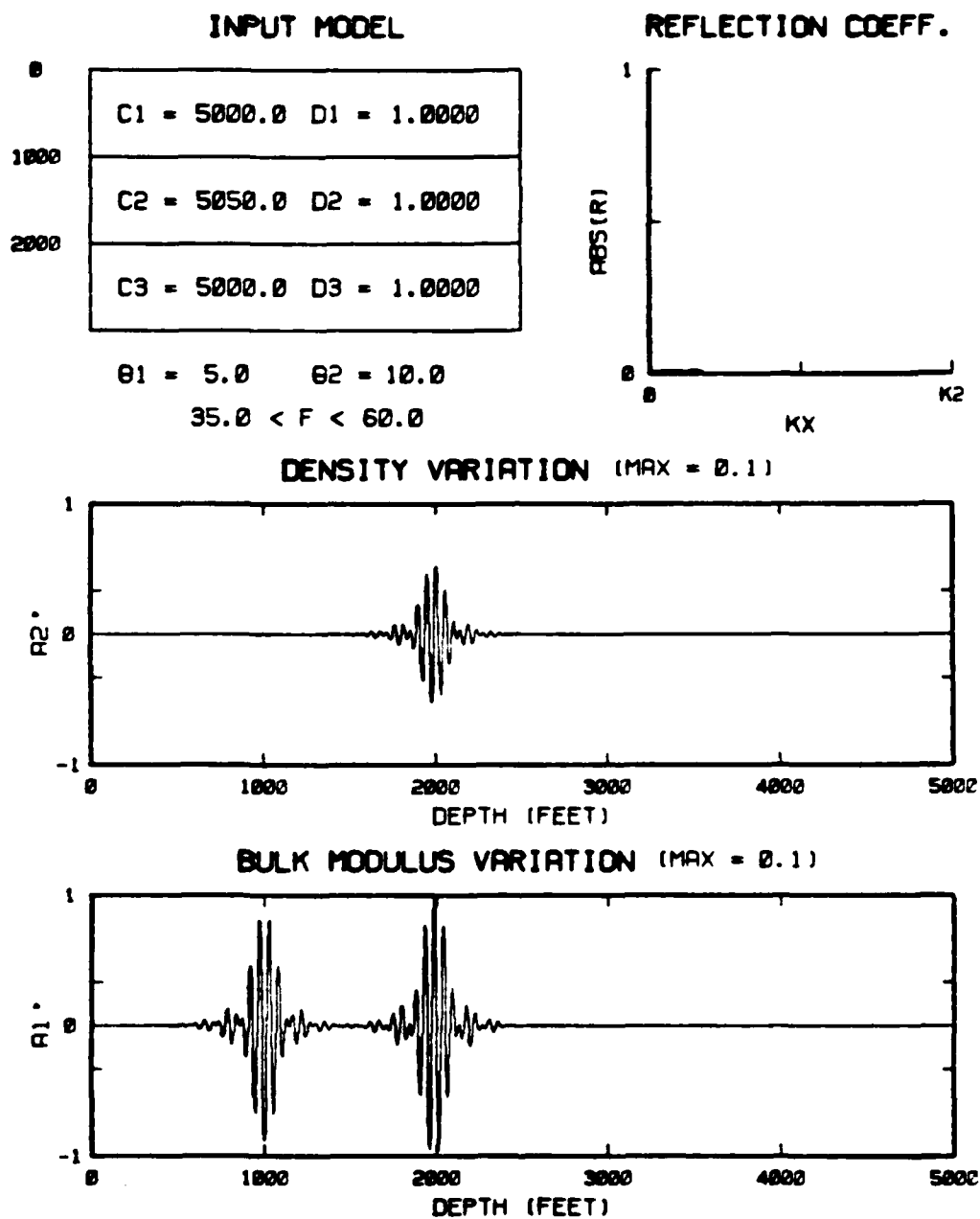


Figure 28. Reconstruction of the model of Figure 26 but for a shallower second reflector.

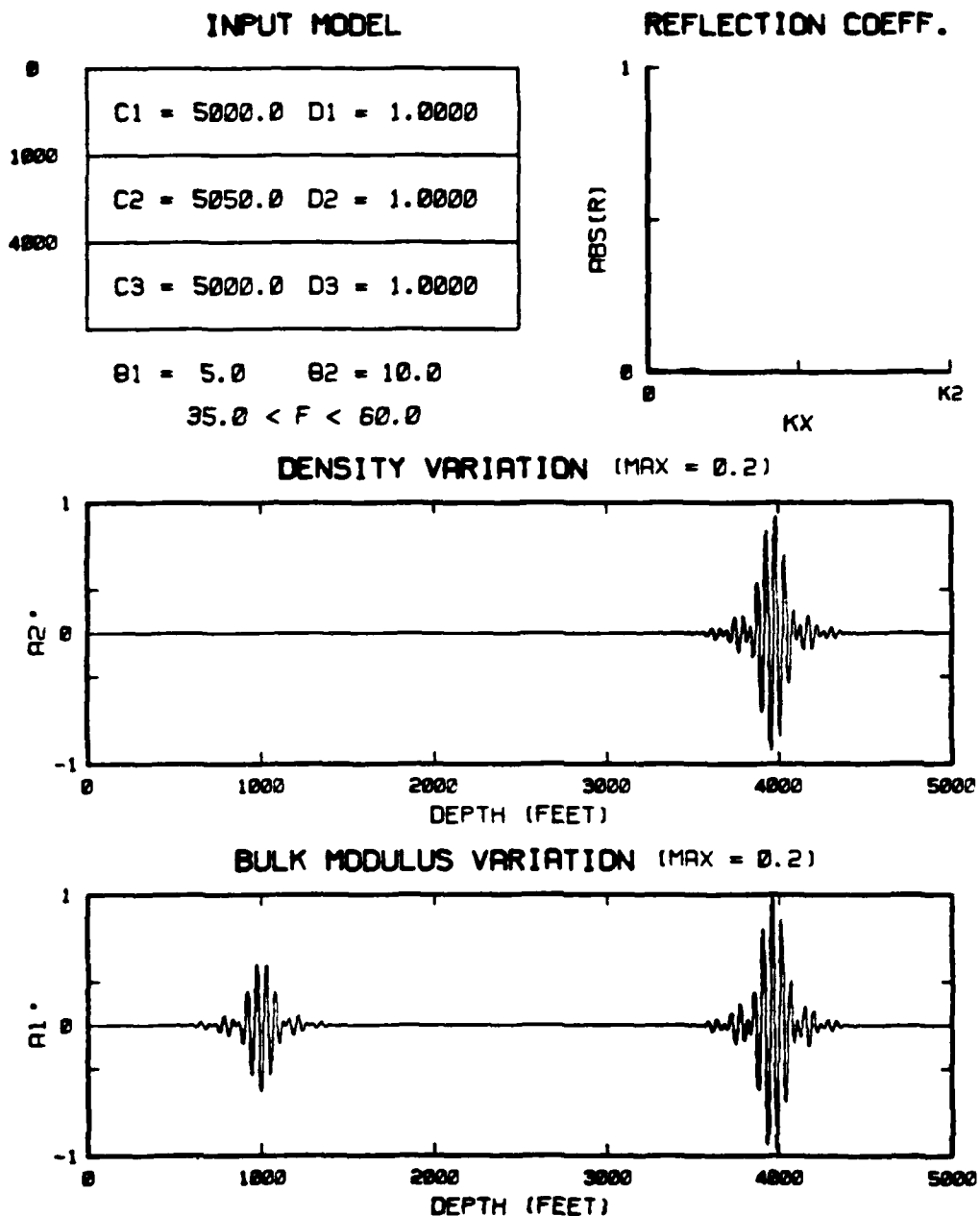


Figure 29. Reconstruction of the model of Figure 26 but for a deeper second reflector.

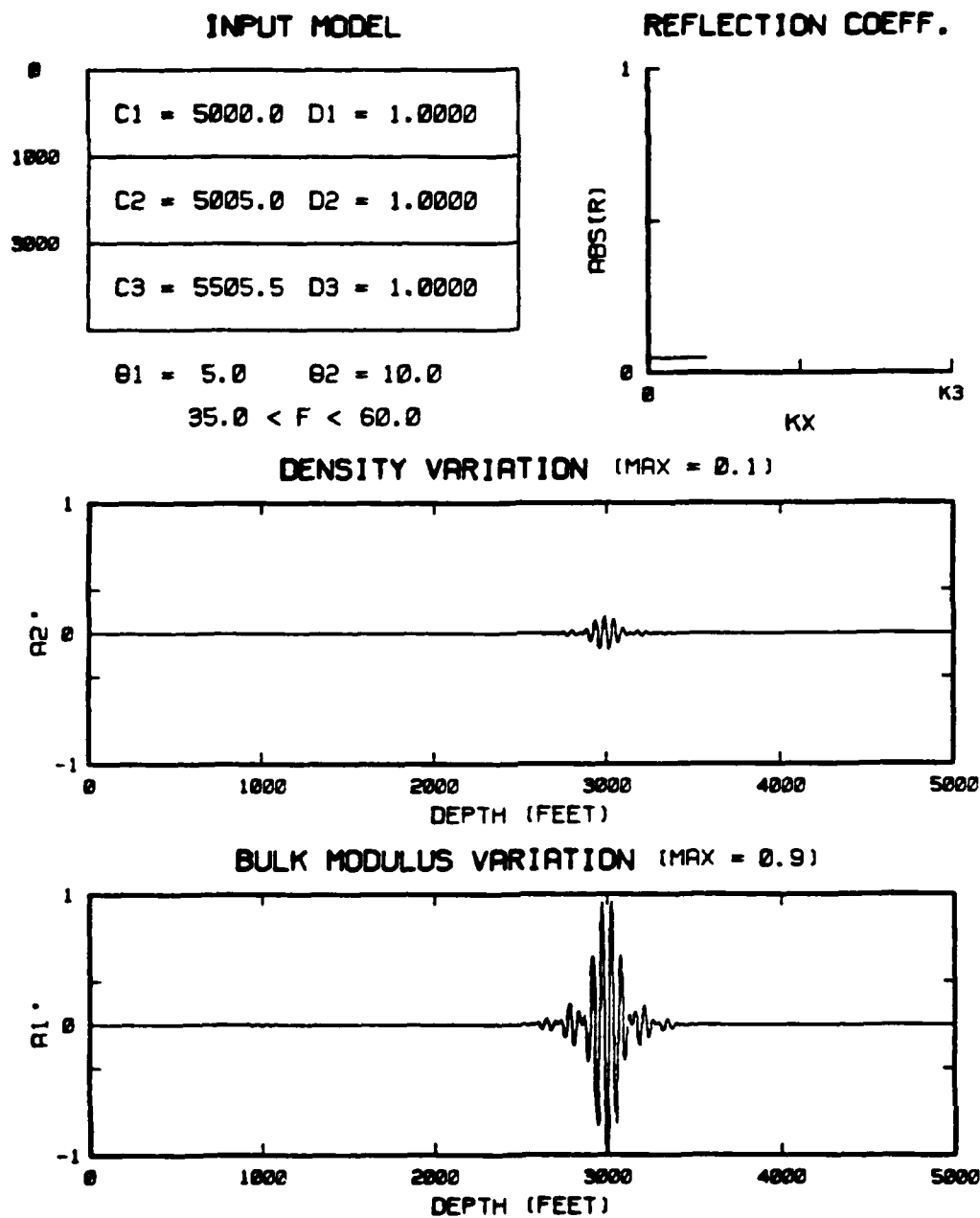


Figure 30. Fixed angle, constant density, double interface, reconstruction for 0.1% and 10% velocity changes.

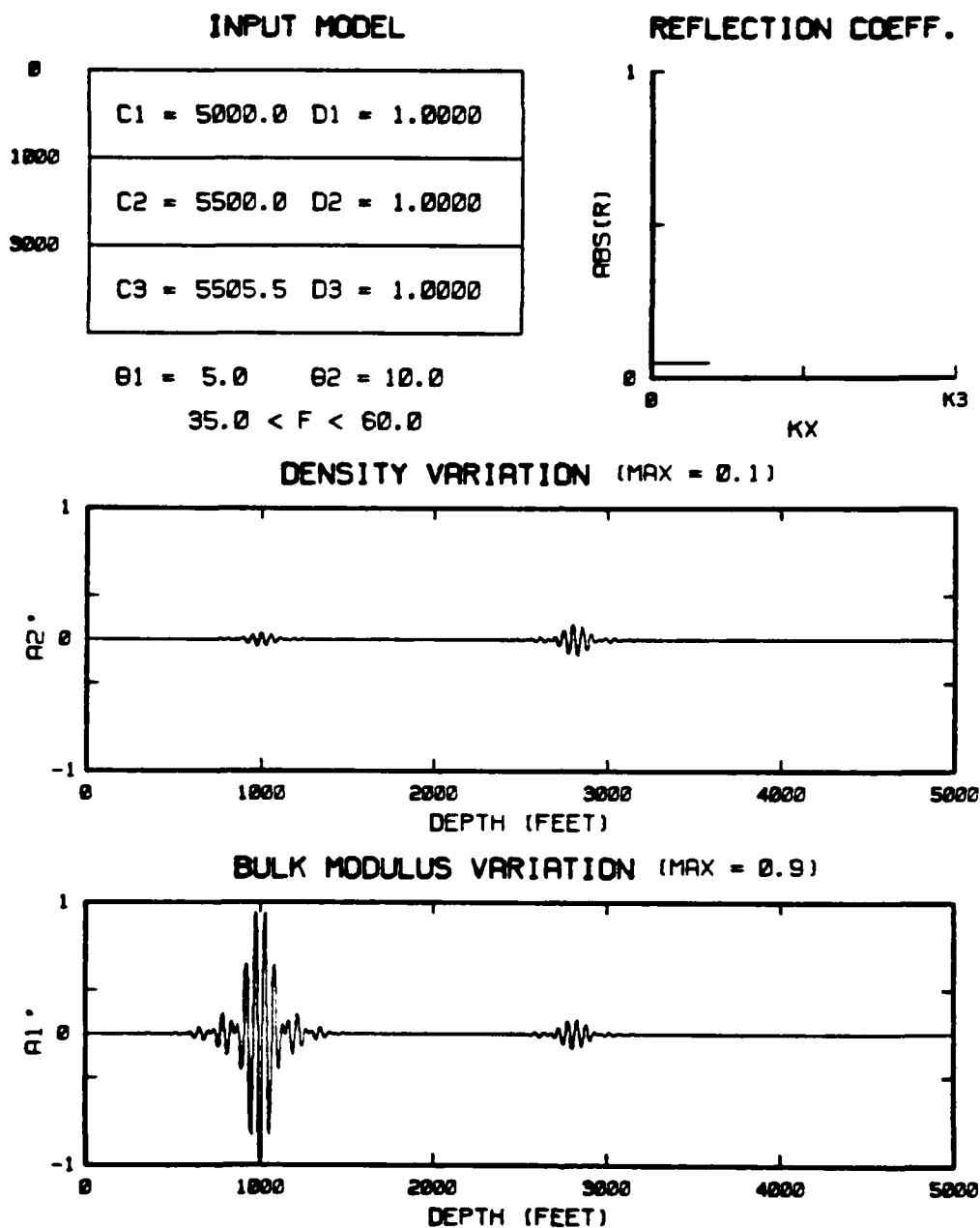


Figure 31. Reconstruction of the model of Figure 30 but with the order of the velocity changes reversed.

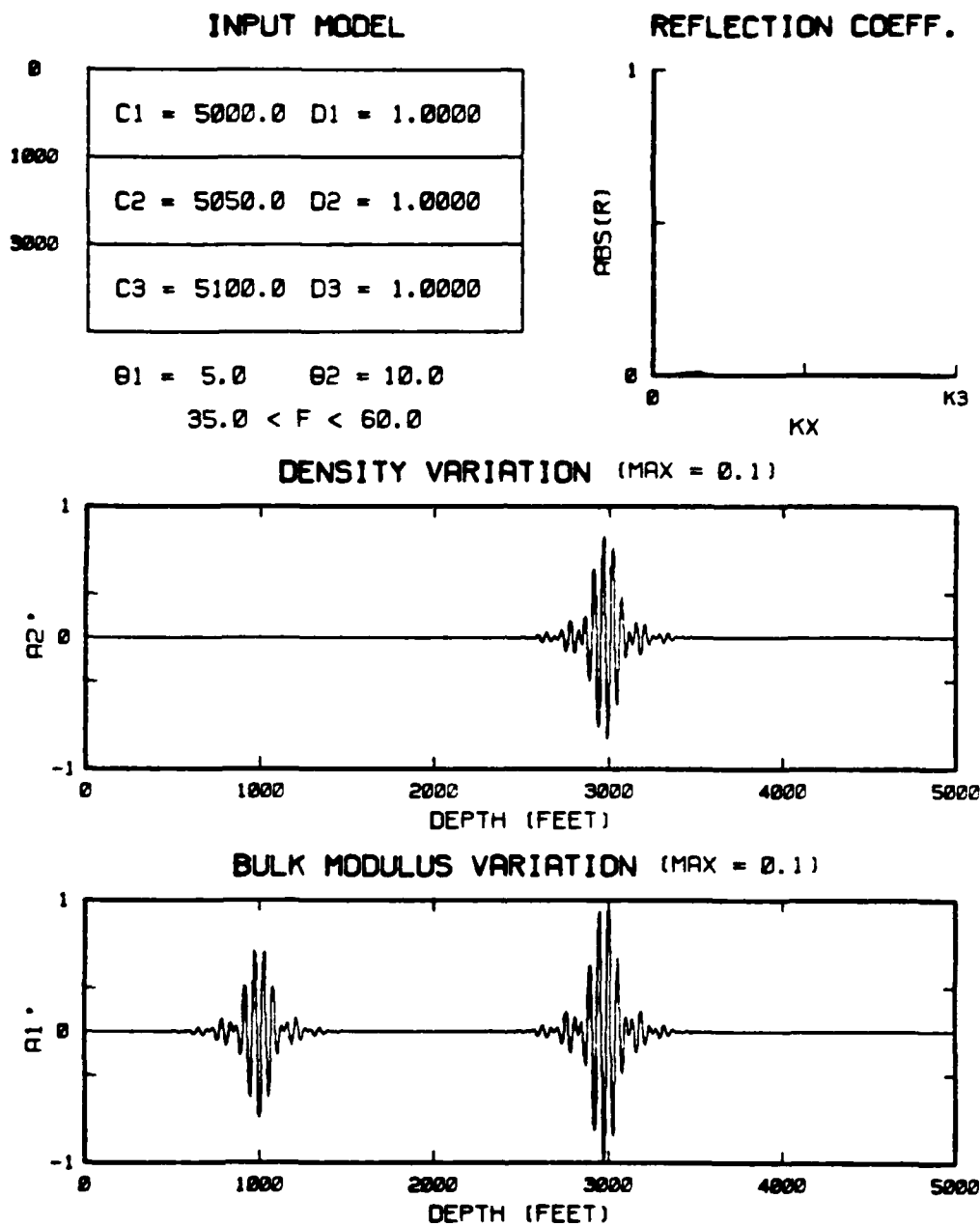


Figure 32. Fixed angle, constant density, double interface reconstruction with 1% velocity changes.

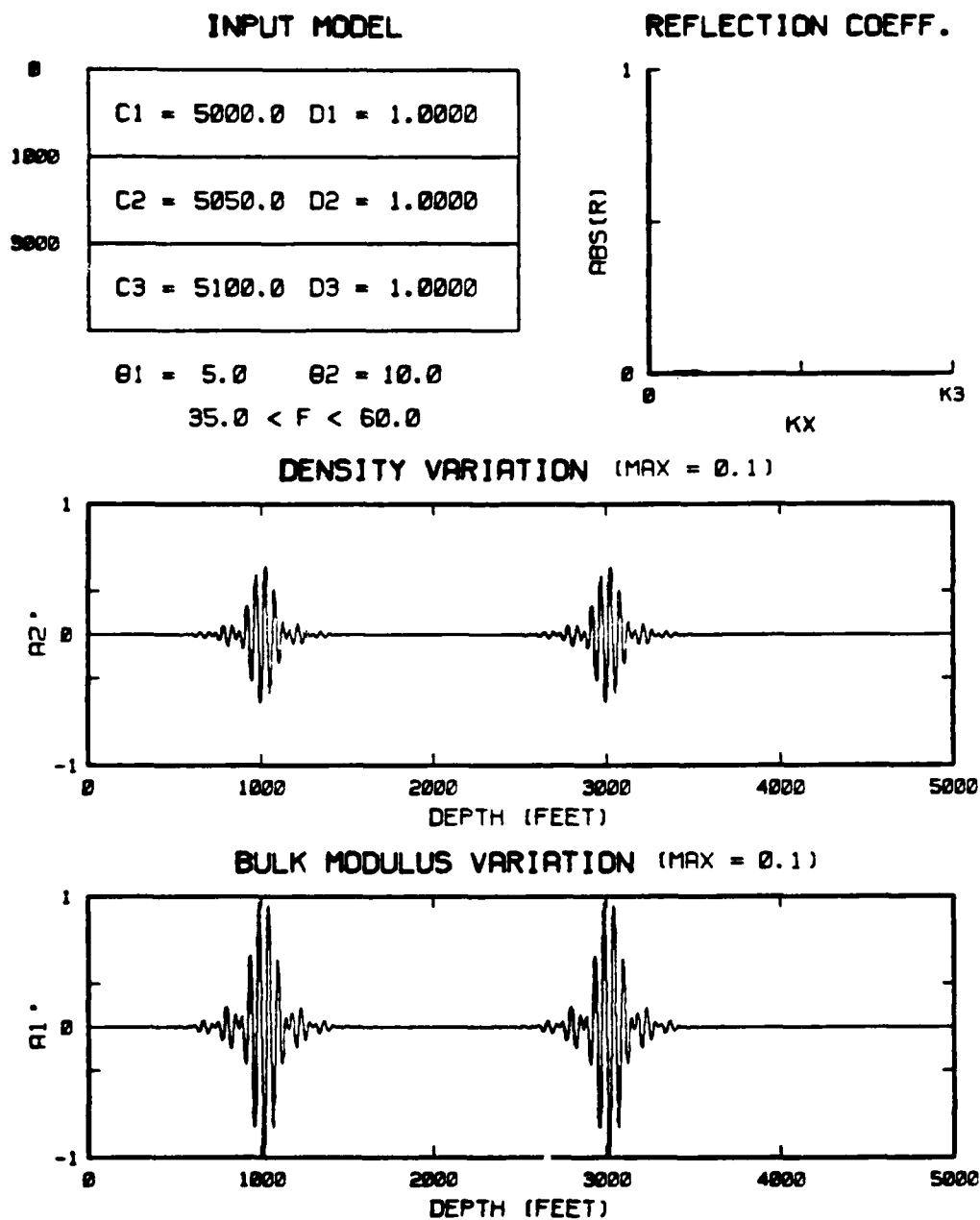


Figure 33. Reconstruction of Figure 32 with the reference velocity equal to the layer velocity.

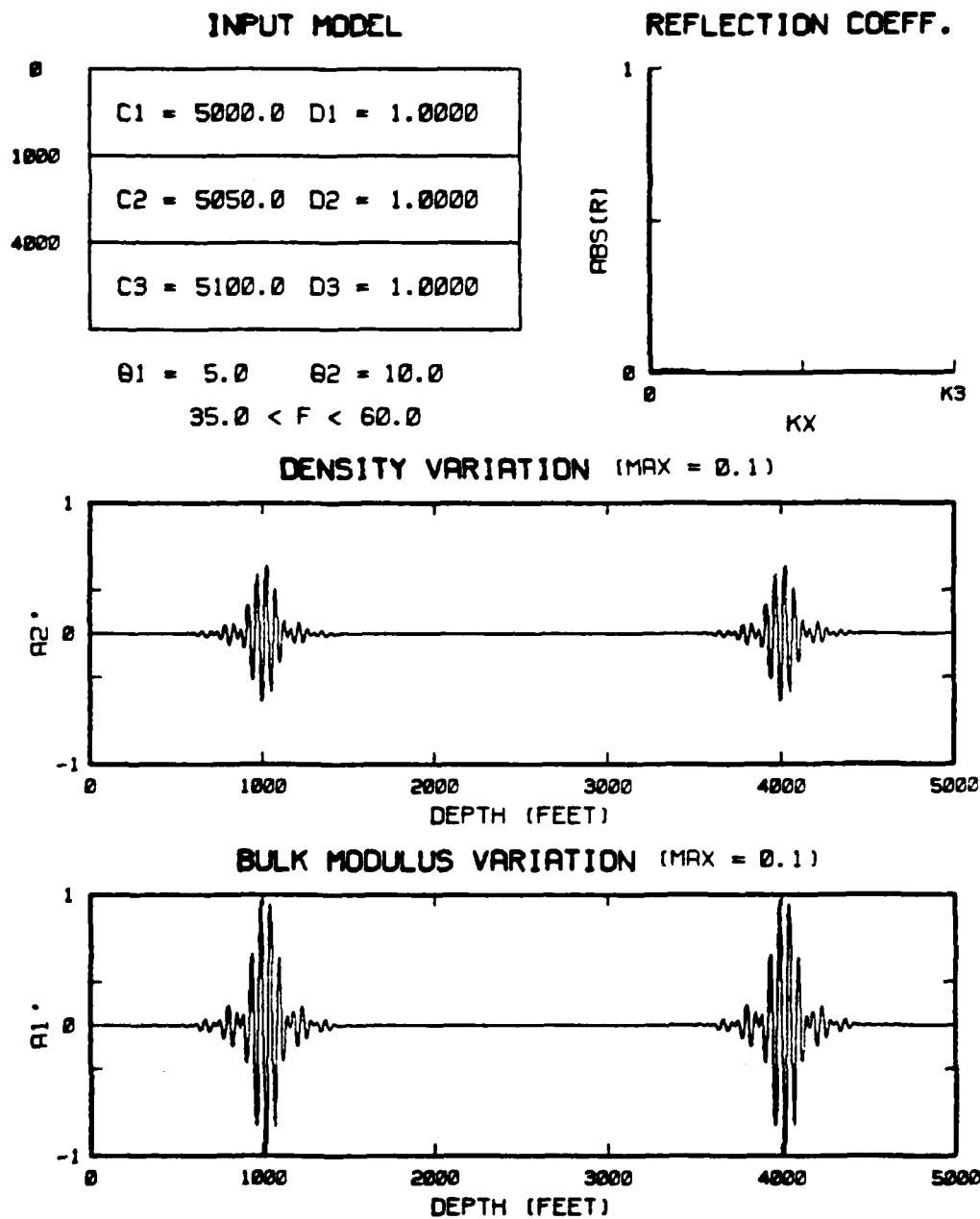


Figure 34. Reconstruction of Figure 33 but for a deeper second reflector.

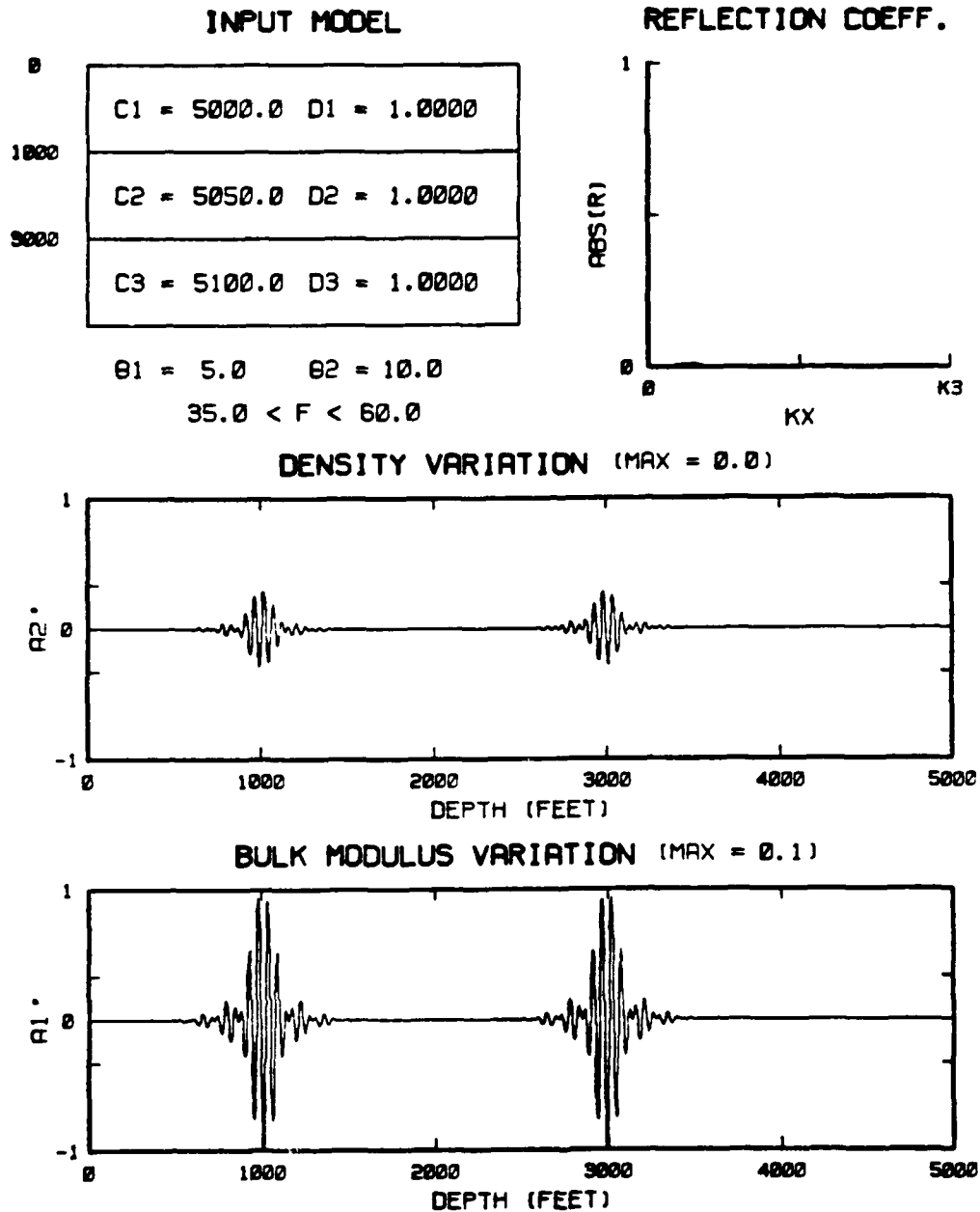


Figure 35. Reconstruction of Figure 32 with the reference velocity equal to 3025 ft/sec.

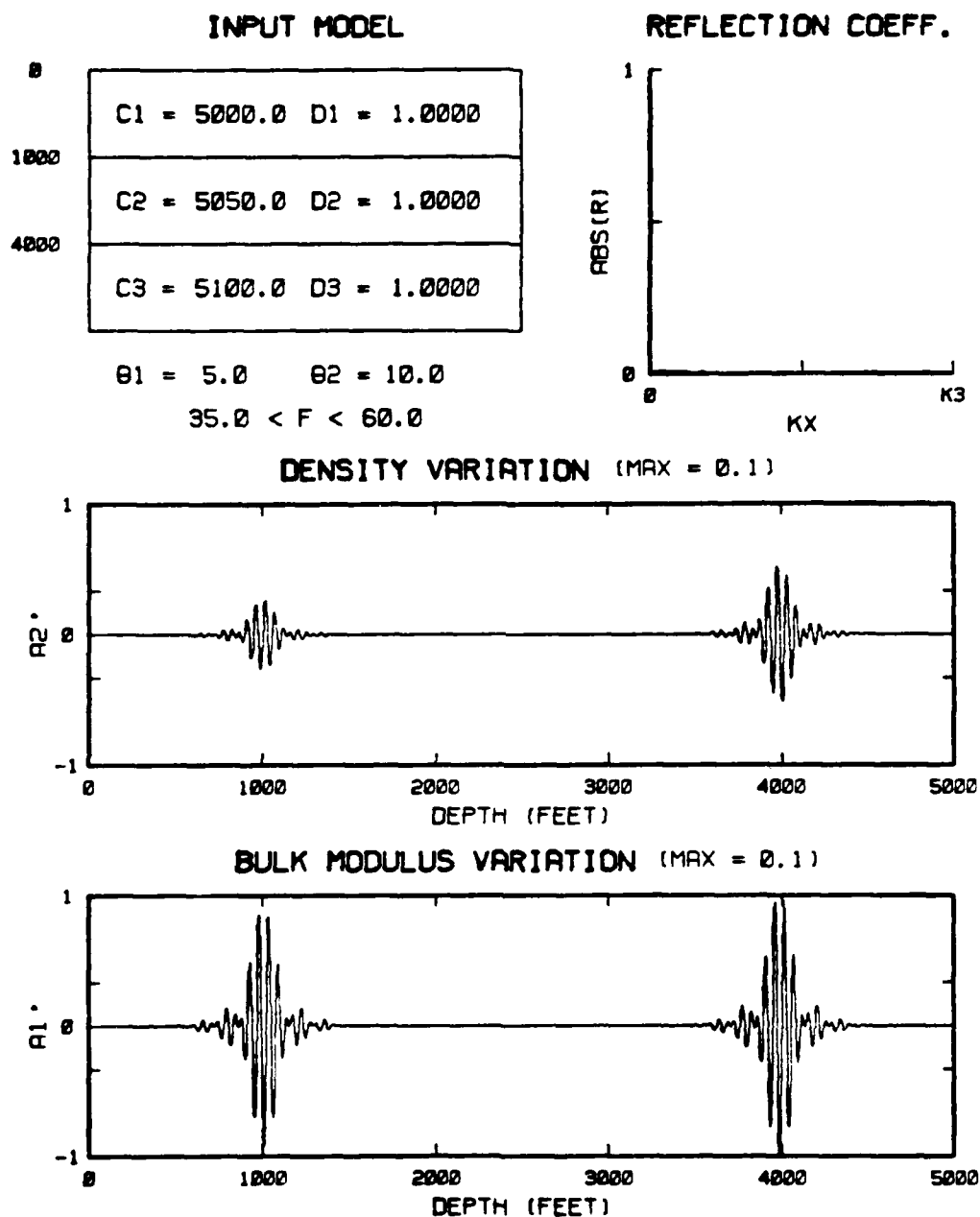


Figure 36. Reconstruction of Figure 35 but for a deeper second reflector.

REPORT DOCUMENTATION PAGE		READ INSTRUCTIONS BEFORE COMPLETING FORM
1. REPORT NUMBER CWP-029	2. GOVT ACCESSION NO. AD-156394	3. REPORT'S CATALOG NUMBER
4. TITLE (and Subtitle) ANALYSIS OF TWO-PARAMETER CONSTANT BACKGROUND BORN INVERSION FOR ACOUSTIC SYNTHETIC DATA		5. TYPE OF REPORT & PERIOD COVERED Technical
7. AUTHOR(s) PAUL B. VIOLETTE		6. PERFORMING ORG. REPORT NUMBER
9. PERFORMING ORGANIZATION NAME AND ADDRESS Center for Wave Phenomena Department of Mathematics Colorado School of Mines, Golden, CO 80401		8. CONTRACT OR GRANT NUMBER(s) N00014-84-K-0049
11. CONTROLLING OFFICE NAME AND ADDRESS Office of Naval Research Arlington, VA 22217		10. PROGRAM ELEMENT, PROJECT, TASK AREA & WORK UNIT NUMBERS NR SRO-159/84APR20 (411)
14. MONITORING AGENCY NAME & ADDRESS (if different from Controlling Office)		12. REPORT DATE May 15, 1985
		13. NUMBER OF PAGES 123
		15. SECURITY CLASS. (of this report)
		15a. DECLASSIFICATION/DOWNGRADING SCHEDULE
16. DISTRIBUTION STATEMENT (of this Report) This document has been approved for public release and sale; its distribution is unlimited.		
17. DISTRIBUTION STATEMENT (of the abstract entered in Block 20, if different from Report)		
18. SUPPLEMENTARY NOTES		
19. KEY WORDS (Continue on reverse side if necessary and identify by block number) Seismic Inversion, Born, Two-Parameter, Constant Background, Stratified Acoustic Medium.		
20. ABSTRACT (Continue on reverse side if necessary and identify by block number) See reverse side		

ABSTRACT

In this thesis, we examine the usefulness of the two-parameter Born inversion method of Clayton and Stolt (1981) under idealized conditions. We implement a constant background procedure to reconstruct line source synthetic data which simulate a stratified acoustic medium. Specifically, this investigation is an extension of the single interface work of Weglein, ² Violette and Kebo (1985) for double interface models. Since we use offset data to recover one-dimensional bulk modulus and density variations, this procedure is termed a 1.5 dimensional inversion. Implicit in these reconstructed acoustic profiles are errors related to the approximate inversion. Phase shifts inherent in the modeled wave field cause these inversion errors not only to propagate, but also to increase with depth. Since the model data are exact, we are able to examine the analytic expressions of these inversion artifacts. From this analysis, we develop an implementation which minimizes inversion errors. This is achieved by both preconditioning the offset data, and judiciously choosing a reference velocity in accordance with inversion goals. Both of these procedures however provide limited improvement, and we conclude that this constant background, frequency domain, method should be enhanced by more sophisticated algorithms. Specifically, we suggest the implementation of either a variable background procedure, or the refinement algorithm of Hagin and Cohen (1984). *Keywords*

END

FILMED

8-85

DTIC